UNIVERSITÉ DU LUXEMBOURG

PhD- FSTM-2022-015
The Faculty of Sciences, Technology and Medicine

DISSERTATION

Defence held on 19/01/2022 in Luxembourg

to obtain the degree of

DOCTEUR DE L'UNIVERSITÉ DU LUXEMBOURG

EN PHYSIQUE

by

Sharif SHAHINI
Born on 4 June 1984 in Torbat-e Jam (Iran)

LARGE GRAPHENE OXIDE FLAKES: SELF-ASSEMBLY AND ELECTRO-OPTICAL SWITCHING IN LIQUID CRYSTAL PHASE

Dissertation defence committee

Dr Giusy Scalia, dissertation supervisor
Research scientist, Université du Luxembourg

Dr Frank Gießelmann
Professor, University of Stuttgart

Dr Miroslav Haluska
Senior Research Scientist, Swiss Federal Institute of Technology (ETH) Zürich

Dr Emmanuelle Lacaze, Vice Chairman
Research director, Institut des Nano Sciences de Paris CNRS – Sorbonne Université

Dr Ludger WIRTZ, Chairman
Professor, Université du Luxembourg

Abstract

Graphene oxide (GO) flakes in aqueous suspension self-organize into liquid crystal (LC) phases. They have been studied for various applications because of their unique properties, but mostly in their bi-phasic suspensions since high concentrations was needed for their pure liquid crystal. The stability of a suspension of GO flakes over time is essential for their application. A crucial change in GO biphasic suspension is the isotropic - liquid crystal phase separation. Here I study the isotropic-nematic phase transition for large GO flakes with an average size of ~38 μm for 570 days to examine their stability. I found that large GO flakes make pure LC phases at a very low concentration of 0.7 mg/mL (0.035 vol%), completely stable over time. I observed that the equilibrium concentration for making a LC phase increases over time, and it is not constant until it reaches a critical concentration for the pure nematic phase. As typical LCs, GO LCs exhibits birefringence property and, interestingly, low-field-induced birefringence. Thus, graphene-based lyotropic LCs are an attractive class of materials for electro-optic devices. To control the electro-optic properties of these high-performance functional materials at a macroscopic scale, it is necessary to understand their self-assembly individually. I study this here by determining the large GO flakes arrangement and spatial order in the nematic phase via synchrotron small-angle X-ray scattering and direct visualization of the flakes with fluorescence confocal laser scanning microscopy. The high fluorescence of large GO flakes makes it possible to individually study the assembly of flakes in real-time when suspended in aqueous dispersions. I successfully performed an enhanced electro-optical switching of large GO flakes in their low concentration nematic phase by using a low electric field, unlike what has been reported so far. I study the optical behavior of GO LCs using polarizing optical microscopy in static and dynamic conditions to follow the flake reassembly under the application of the electric field.

Keywords: graphene oxide, liquid crystal, electro-optical switching, assembly, orientational order

Table of Contents

List of Figures

Introduction

Monolayer carbon-based nanomaterials like graphene have distinct and superior properties - making them regarded as “super-materials” – already have significant impacts on different aspects of science and technology [1]–[3]. Wet chemical exfoliation of graphite is an easy and high yield method for producing graphene flake suspensions, having GO as an intermediate step [4]–[6]. Graphene flakes in water show macroscopic properties due to their self-assembly, making graphene attractive for applications not only in the solid phase, but also in the liquid phase [7]–[9].

In aqueous suspension, GO flakes form colloidal LC phases at very low flake concentrations, in agreement with Onsager’s theory, due to volume exclusion or reduced configurational entropy effects [10]–[14]. Similar to typical LCs, GO LCs exhibit tunable light transmission between crossed polarizers due to birefringence [13]. The anisotropic shape and the chemical structure are the reasons for the formation of lyotropic LC phases with GO flakes in water. The shape can be associated with disk-like building blocks since a high rotational symmetry axis can be found normal to the flake plane and the diameter of the flakes is an order of magnitude larger than the flake thickness.

Typically, the flakes have a diameter (D) in the micrometer range and thickness (T) of about 1 nm. This gives an aspect ratio D/T of a value higher than 1000, which is a very high compared to the known lyotropic LCs, resulting in very low threshold for the LC phase formation [7], [15]. According to the Onsager’s theory, the high aspect ratio of GO flakes should result in GO LC phase formation at low concentration due to the overlap of their high excluded volumes.

The theory predicts that the transition from isotropic to nematic phase occurs sharply above a threshold volume fraction of disks, proportional to the inverse of the aspect ratio [10]. This type of phase transition, driven by an increase in the concentration of the dispersed particles in water, is characteristic of lyotropic liquid crystal systems. Another important aspect is that the GO flakes have very vast differences in size and the GO samples are characterized by polydispersity, which is not considered in the Onsager's theory. The consequences on the phase behavior are that between the isotropic and full nematic phase, there is a wide range of bi-phase region in which the isotropic and nematic phases coexist [11], [12]. However, the concentration threshold for the formation of LC phases is still relativity low compared to standard surfactant-based lyotropics [16].

It is important to point out that not all GO aqueous suspensions form liquid crystal phases. The formation of such phases is dependent not only on the aspect ratio and shape of the building blocks but also on various factors such as the surface potential, responsible for the repulsive forces between flakes [7], [17]. The GO LC phases are stable due to GO flake's high aspect ratio, and good dispersibility in water; because of dense oxygen functional groups (e.g., hydroxyl, carboxyl, and epoxy group) on GO flakes basal plane and edge [18]. The functional groups covalently bonded to the graphene carbon atoms make the flakes hydrophilic, thus compatible with water as a host medium for GO LC, unlike graphene. The GO surface charge produces a repulsive electrostatic potential between the flakes instead of the attractive van der Waals potential responsible for aggregation in graphene water suspension, which generates instability [15].

An external stimulus can align GO flakes with uniform orientations within a large domain size. Applying an external electric field from high-frequency alternating current (AC) is the most effective technique to control the alignment of GO flakes in aqueous dispersion. Because of the electro-optical switching of GO flakes, a large Kerr coefficient is obtained for low GO

concentrations [19]. However, the electro-optical switching of GO flakes in the nematic phase is still a challenge because the high concentration of small GO flakes in nematic dispersions causes inter-flakes interaction to increase, hindering field-induced ordering [20]–[22].

Electro-optical switching of a GO dispersion needs unique conditions in terms of inter-flakes interaction and assembly. Remarkably, large GO flakes form a stable LC phase at very low concentrations [23]. In addition, large GO flakes have larger polarizability and stronger response to an electric field, hence lower voltage is required to control their alignment [20], [24]. The ability to switch in the nematic phase is crucial for electro-optical applications of GO due to the needed long-term stability of GO dispersion. Because the isotropic - liquid crystal phase separation happens in GO dispersions with a concentration below the critical concentration for having a pure nematic phase.

In this dissertation, I focus on a graphene oxide with a remarkably large average flakes size resulting in an extremely low concentration value for obtaining a stable full nematic LC phase. This means that GO LC phases could appear and be stable over time at very low concentrations. A deep insight into interactions of GO colloids, to understand the origin of the self-assembly, is necessary for in situ fabrication of complex GO architectures and control of GO microstructure in innovative GO LC-based applications [8], [9], [25], [26]. I investigated the assembly of GO flakes in confined spaces and their reorientation under electric field, to understand the underlying mechanism responsible for their self-assembly phenomenon.

In addition, I carefully examine the electro-optical switching of large GO flakes in the nematic phase. The shape and chemical structure of the flakes suggest that graphene-based LCs have optically negative anisotropy. I examine it by determining the flake arrangement in the nematic phase using small-angle X-ray scattering (SAXS) measurement and polarizing optical microscopy (POM) since a common orientation of the flakes generates the birefringence. GO

flakes in aqueous dispersions or solid-state instantly exhibit broad-band photoluminescence in the visible range wavelengths, not like graphene having a zero-band gap [27]. I could directly observe the assembly of GO flakes in their original dispersions in real-time and individually with confocal laser scanning microscopy (CLSM). This is crucial since it has been reported that the freeze-dried GO assemblies do not preserve the original GO alignment in their aqueous dispersion before drying, as the freezing of water reconstructs the GO assembly. Elimination of the water between the GO particles, by either sublimation or evaporation, greatly alters the interparticle interactions and the GO alignment structure [28], [29]. My findings and understanding could help to deepen and clarify the GO flake self-assembly and their behaviors under an electric field to prepare them for real-world applications.

Chapter 1: Background

Research into graphene and graphene oxide (GO) signifies a developing field of interdisciplinary science that includes different disciplines such as physics, materials science, chemistry, nanotechnology, and device fabrication. The discovery of graphene has led to in-depth research on new two-dimensional (2D) materials and devices during the last two decades. Graphene is broadly used in various real-life commercial applications because of its exceptional properties, like high thermal and electrical conductivity, high carrier mobility, the highest strength and etc. [9], [30]. Graphene oxide is synthesized through oxidation of graphite having a high concentration of oxygenated functional groups on its basal plane and it is a significant chemical precursor of graphene [31]. GO flakes as uniform single layers and being dissimilar from pristine graphene, form stable dispersions in water and various organic solvents even at high concentrations. However, GO preserves the original anisotropy of graphene flakes and its lateral size can reach more than 100 μm. The combination of good dispersibility and huge anisotropy of GO can result in the formation of liquid crystals (LC) in different solvents, like water [30], [32].

1.1 Graphene Oxide

1.1.1 Synthesis

The GO history started more than 150 years ago. In 1859, Brodie reported for first time using pristine graphite for the synthesis of graphite oxide. He invented a method consisting in oxidation and exfoliation of natural crystalline graphite and resulted a considerable amount of

single layer GO [33]. However, the synthesis of GO received a full attention just in the last two decades, mainly driven from the original impact by Ruoff et al [34]–[36]. We can basically divide the methods for synthesis of GO into two principle categories: using simple carbon molecules to produce pristine graphene, “bottom-up” methods, or using a carbon source like graphite to extract layers of graphene derivatives, “top-down” methods [37], [38]. Bottom-up methods like epitaxial growth on silicon carbide wafers or chemical vapor deposition are slow and inefficient for mass production of GO [39]. Thus, the top-down methods are more common for producing graphene derivatives like GO [40], [41].

Numerous famous top-down methods have been reported for the synthesis of GO and among them, the ones that the most widely used are modified Hummers methods, especially for the mass production of GO [42]–[46]. Figure 1-1 shows schematic of a method based on using strong chemical oxidants for the synthesis of GO flakes suspension from bulk graphite, including related optical images or sample appearances for each step. As presented, the synthesis of GO is involved of three successive steps, (i) acid intercalation, (ii) oxidation, and (iii) hydrolysis and exfoliation. The three steps indicate development of the two middle products and the final GO product [9], [47].

Synthesized GO flakes can have size range from 40 nm to more than 100 μm, dependent on their precursor graphite source and the used oxidation process. Different factors, for instance long oxidation time, high oxidation temperature and a high density of oxidizing agent, usually results in GO flakes having a smaller lateral size, regardless of the original source of graphite [16], [19], [20]. Generally, factors like crystallinity and size of the graphite source, level of oxidation, and extent of exfoliation (ultrasonication/mechanical shaking), are closely related to each other [45], [48], [49]. Therefore, the change of one of these factors can have a dramatic effect on the size of GO flakes, which influence the behavior of GO LC [9].

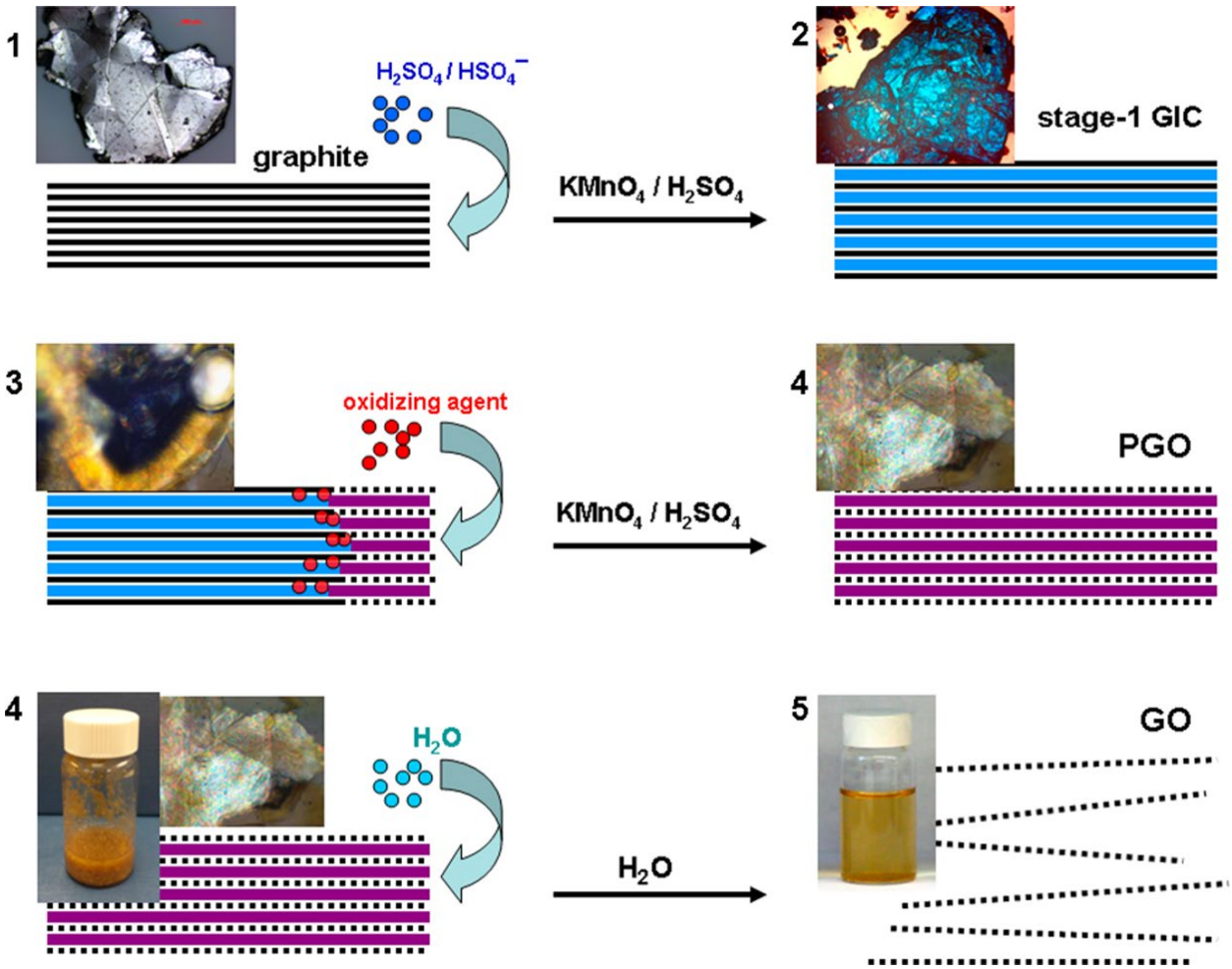

Figure 1-1. Schematic of a method based on using strong chemical oxidants for the synthesis of GO flakes from bulk graphite. Solid black lines represent single layers of graphene and dotted black line represent single layers of GO, where wide blue line and purple line respectively show an intercalated acid layer and combination of acid with the reduced form of oxidizing agent. GIC is graphite intercalation compound and PGO is pristine graphite oxide. Reproduced from reference [47] with permission from ACS.

1.1.2 Structure of GO

The chemical structure of GO is alike to its parent graphite oxide, when we compare their carbon regions having oxygenated functional groups. An atomically thin and continuous two-dimensional network of carbon atoms containing functional groups on the carbon basal plane

and the edges is the most generally recognized structure of GO flakes. Based on the established model of graphite oxide in 1998, Figure 1-2, three kinds of oxygen functional groups can exist in the graphite structure. They are epoxy (on the carbon plane), hydroxyl and carboxyl groups (above and below the carbon plane). According to this structural model, because of the oxygen layers being negatively charged, epoxide groups are chemically inactive in the planar carbon lattice [50], [51].

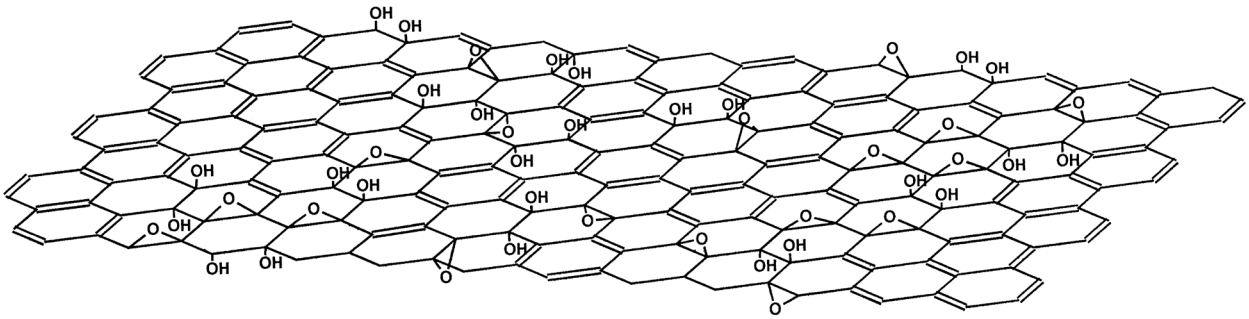

Figure 1-2. Structural model for GO. Reproduced from reference [50] with permission from Elsevier.

Using high-resolution transmission electron microscopy (HR-TEM), the structural model of graphite oxide was validated with some adjustments for single layer of GO, Figure 1-3. It was observed that GO has much larger graphitic and oxidized areas than predicted by the GO model. Besides, holes were also detected in the GO flakes. The holes are created when CO and CO_2 are released through the strong oxidation reaction. In addition, no specific order among the primary and dominant (hydroxyls and epoxies) and edge (carbonyl) functionalities was observed as the oxidized areas make a continuous network all over the carbon lattice [52], [53]. As an important proportion of the basal plane is still included carbon domains, these areas on GO flakes are considered to be comparatively hydrophobic, whereas the very acidic edge areas are considered to be hydrophilic, consequently, GO have an amphiphilic structure [54]–[56].

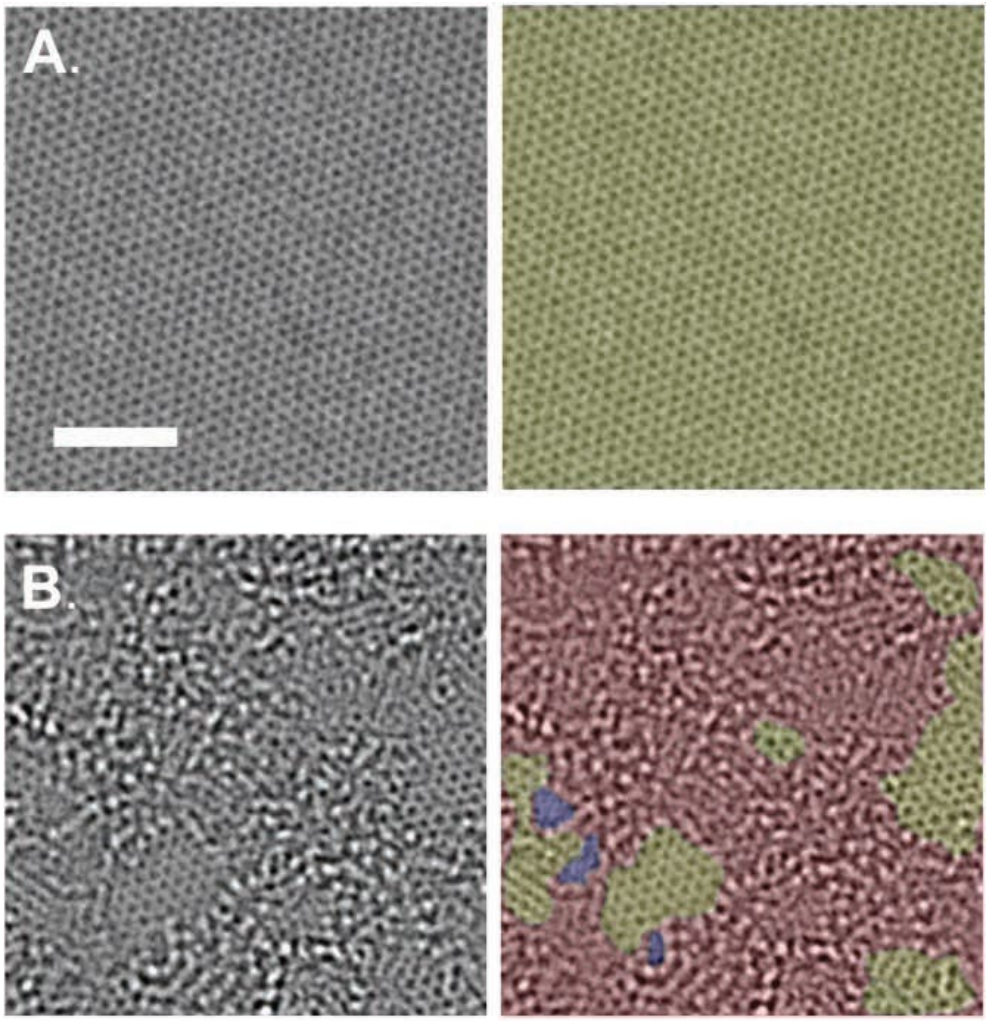

Figure 1-3. TEM images of (a) a perfect crystal lattice of suspended single sheet of graphene. On the right, yellow color shows graphitic area. (B) showing suspended single layer GO flake having the crystal lattice with defects. On the right, graphitic areas are shown in yellow, holes in blue, and red color indicates disordered regions i.e., oxygen functionalities. Size of scale bar is 2 nanometers. Reproduced from reference [52] with permission from John Wiley and Sons.

1.1.3 Dispersibility of GO in aqueous/organic solvents

In the natural form of graphite, the graphene layers are attached to each other by very noticeable π-π stacking interactions. The high thermodynamic stability of graphite is a direct result of this noncovalent interlayer sticking. Therefore, these interactions are always involved against the wet chemistry of graphene. For instance, the equilibrium of solvent-dispersed graphene flakes

or a targeted exfoliation of graphite is in a competition with reaggregation at all times. Consequently, it is not possible to completely disperse a graphite crystal into single graphene flakes in a solvent. But, using an assistance like a surfactant makes it possible to obtain partially dispersed graphene flakes. On the other hand, the wet chemical dispersion of graphene is efficiently possible thorough the graphene transformation into a derivative, for example GO as a single atom carbon layer with oxygen containing functional groups covering both surfaces [32], [41], [57].

The GO flakes dispersibility in a solvent is greatly determined through the surface functionalities of GO and the nature of the solvent. In water and polar organic solvents, GO can form a stable dispersion because of having large amount of oxygen functional groups. However, in nonpolar solvents GO normally display a low dispersibility [57]–[59]. For the stability of the GO suspensions, the pH is also an important factor. In aqueous solution, GO flakes can homogenously be dispersed in normal pH conditions, because of the repulsive interaction between GO flakes. On the other hand, since the ionization of GO is poor in the low pH conditions, acidic pH conditions result in a noticeable aggregation of GO flakes, because of insufficient electrostatic repulsion between GO flakes [60], [61]. If the GO aqueous suspensions pH is increased to basic regions, the aggregation of GO flakes also happens since the high concentration of alkali leads to the partial reduction of GO [9], [62].

1.2 Liquid crystallinity in nanomaterials

The LC phase is a real thermodynamically steady state of matter and follows the conventionally well-defined solid, liquid, and gas states. All these dissimilar states of matters are defined via the dissimilar degrees of molecular or atomic assembling. For example, a gas has a totally disordered structure, where a liquid has a short-range order and a crystalline solid is defined

through its long-range 3D atomic assembly. In general, LC phase is a middle state between the normal solid and liquid states in terms of assembling and related properties, hence it is frequently so-called a mesophase, meaning intermediate shape. A substance having the LC phase mixes the physical properties of a solid and a liquid phase together. The study of LC materials has increasingly grown during the last century since Reinitzer revealed the optical birefringence of cholesterol in 1888 [63], and now we regularly face LC materials in our daily life and for many advanced application. Various functional materials and devices are based on LCs. For example, small molecular LCs are essential for the technology of modern display, i.e., LCDs from large scales televisions to mobile devices. Furthermore, LCs are also used in photonics, optical lens, telecommunications, chemical and biological sensors, drug delivery, and etc. [9], [64]–[66].

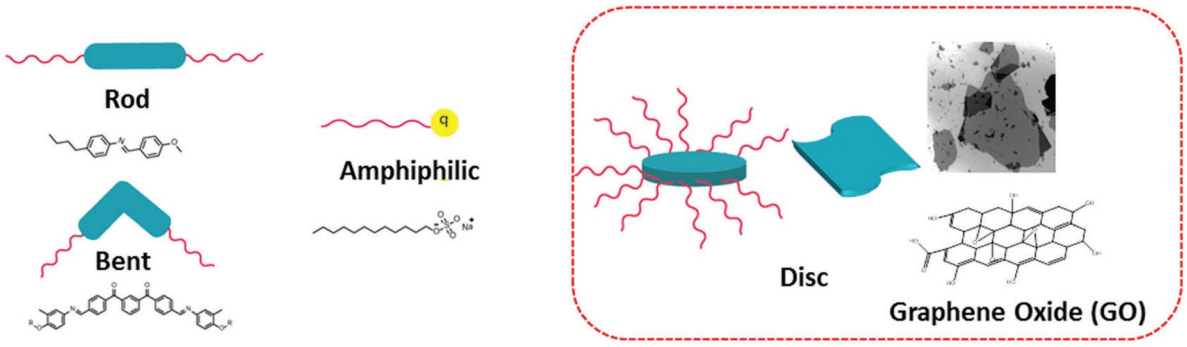

Figure 1-4. Different mesogens, LC materials, with dissimilar molecular shapes making LC phases. GO is a discotic shape mesogen. Reproduced from reference [9] with permission from Royal Society of Chemistry.

LCs can be classified by different methods like the evolution condition of LC phase transition. The LC phase can happen either via a variation of temperature in the original form i.e., thermotropic LC phases or through a variation of concentration in the suspension state i.e., lyotropic LC phases. According to the anisotropic shapes of the LC materials, the basic units of the LC phase are usually so-called mesogens and they can be categorized into discotic (disk-

like), calamitic (rod-like), and banana (bent) LCs [9], [67]–[69]. A schematic image for the general LC categories is given in Figure 1-4. The geometry and orientation of the mesogens and the aspect ratio of their anisotropic shape control the LC phase structures. When mesogens are uniaxially aligned without showing a positional order, LC phases are called nematic. Smectic is when mesogens have 1D positional ordering by layered structures. Cholesteric, as well named chiral nematic, has a helical order of mesogens by the chiral axis [9]. Discotic mesogens may show nematic and/or columnar phases. Figure 1-5 shows a schematic for the normal LC classifications.

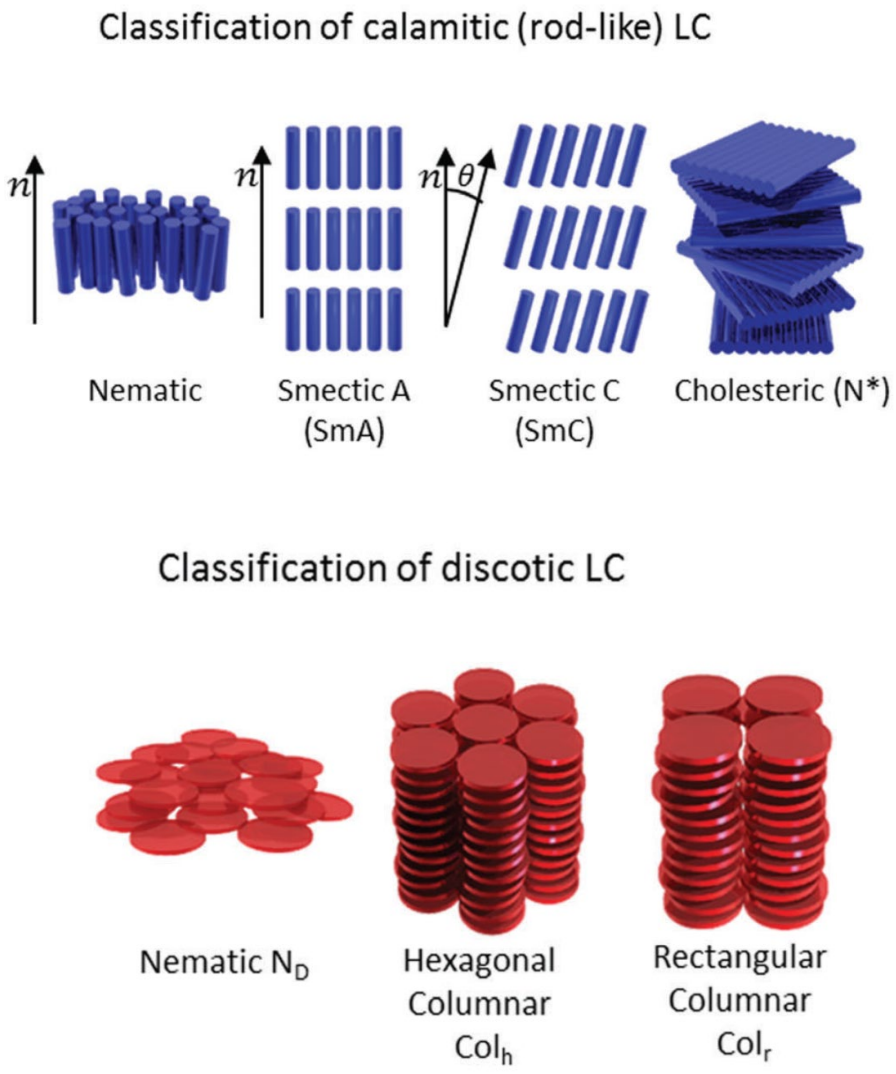

Figure 1-5. Different Classification of LCs, based on the orientation and order of mesogens. Reproduced from reference [9] with permission from Royal Society of Chemistry.

1.3 Liquid crystallinity of GO

From the old natural happening clays and oxides, 2D colloids have been developed to the recently discovered GO flakes. Numerous nanomaterials and 2D colloids can form lyotropic LCs as they have large enough anisotropy and stable dispersion concentration. Regardless of their dissimilar chemical composition and related properties, their LC formation mechanism looks identical in the theoretical frame of 2D colloidal LCs. It is becoming more significant to understand their spontaneous behaviors. For GO suspensions, besides the normal nematic phases, the variety in surface composition (electrostatic or steric repulsion), tunable size and distribution, aspect ratio and shapes of flakes result in the discovery of different mesophases, including lamellar, columnar, biaxial and chiral mesophases. The organizational assembly of GO LCs are very valuable for the production of materials with well-organized structure and so enhanced performances [9], [30], [70].

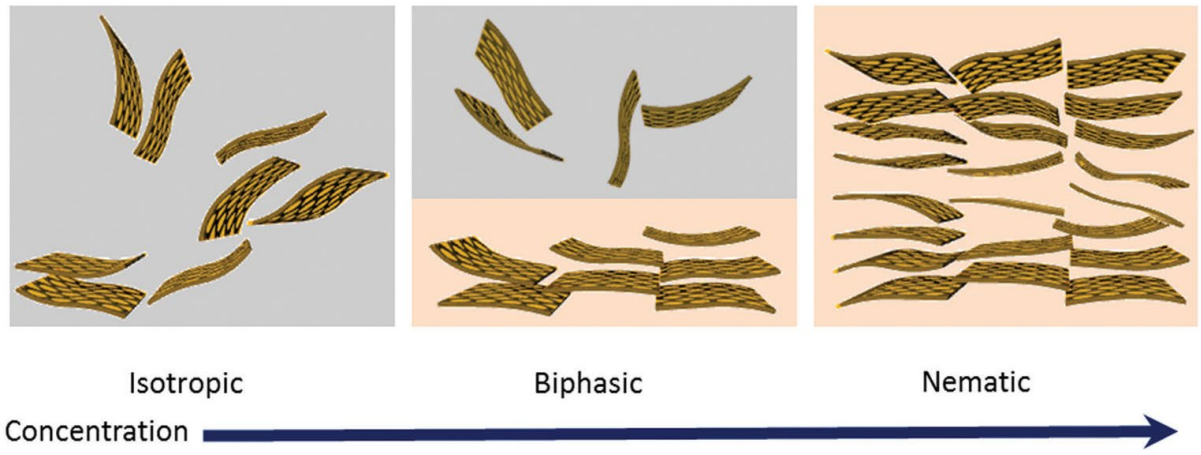

Figure 1-6. Schematic showing the isotropic to nematic phase transition of a GO dispersion with increasing concentration. Reproduced from reference [9] with permission from Royal Society of Chemistry.

GO flakes are the principal elements (mesogens) in GO LCs while many parameters, like their mass/volume fraction, shape anisotropy and polydispersity, in addition to pH value and ionic strength can have a great impact on their LC phase behavior. Anisotropic particles like GO flakes having large aspect ratio, form an isotropic phase in a very dilute dispersion. By increasing concentration of particle, slowly a biphasic state appears, when there is a coexistence of the isotropic and nematic phase that eventually develop into a full LC phase, Figure 1-6. In the same way, GO flakes in water and some polar solvents can form colloidal isotropic and nematic LC phases.

The mechanism for formation of GO LC can be described via the excluded-volume effect theory, expressed in 1949 by Onsager [71]. In basic terms, we can understand the excluded volume of a particle as the volume being inaccessible for other particles because of the existence of the particle. The particle with anisotropy excludes the geometrical center of a second particle from accessing a specific volume. In Figure 1-7, red dash lines show the excluded volume of 1D and 2D anisotropic colloid particles. In the perpendicular arrangement as compared with the minimal volume in parallel alignment, the excluded volume of anisotropic colloids turn out to be maximal. In colloidal systems, as stated by Onsager theory, LC phase formation is fully determined by entropy and happens owing to the contest between the loss of orientational entropy and the increase in the translational entropy (excluded volume entropy).

In a colloidal system consisting of charged particles, the particles want to keep their distance from each other at a certain length. GO flakes have their highest orientational entropy in isotropic dispersions (dilute concentrations) since they are far away from each other and for their movement, they are completely unrestricted in a dilute dispersion. On the other hand, as the concentration of GO flakes increases, GO flakes are restricted and their freedom of movement decreases, results in a loss of orientational entropy. Thus, neighboring GO flakes

get closer to each other, causing neighboring GO flakes an overlap of their excluded volumes. Consequently, GO flakes arrange themselves in parallel ordering (nematic) to lower their excluded volume and to increase their translational entropy. Hence, the translation entropy of colloids can be maximized by their regular alignment and the increase in translational entropy becomes larger than the reduction in orientation entropy that results in the formation of orientated structure as LCs. This way, the GO flakes suspensions becomes thermodynamically stable as the increase in positional entropy compensates the orientational entropy loss. At the transition concentration, we can clearly distinguish the isotropic and nematic phases, hence it normally identified as the critical concentration for having nematic phase [9], [30].

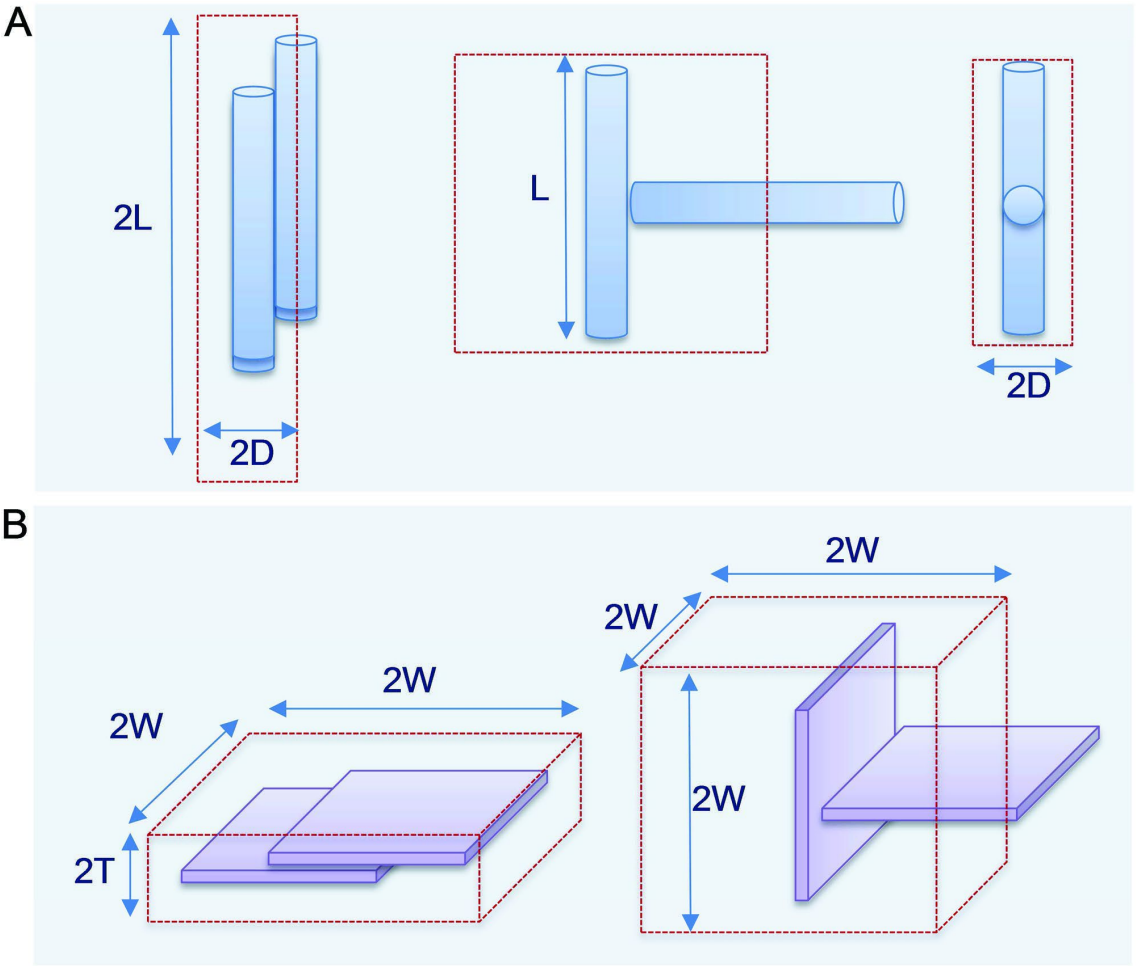

Figure 1-7. The excluded volumes of 1D (A) and 2D (B) anisotropic colloid particles. Reproduced from reference [30] with permission from John Wiley and Sons.

Onsager theory can successfully explain the isotropic to nematic phase transition in the GO suspensions. However, we should consider that in Onsager's theory the particles are presumed as ideal rigid rod and this is not totally in agreement with the complex structure of GO. GO flake is a superflexible system and its level of orientational entropy loss is not compatible with a rigid particle. In addition, in Onsager's theory the steric hindrance between GO flakes, the congestion because of the physical presence of the surrounding ligands, and their electrostatic repulsion were not considered [72], [73]. Hence, it is difficult to find an agreement between the experimental results and theoretically expected critical concentration values. Also, for the reason that the excluded volume affected not only by the electrostatic interaction between the GO surface functionalities, but also by the polydispersity of GO flakes. According to Onsager theory, the critical concentration for formation of LC phase is directly related to four times the ratio of thickness a particle and its width, $\phi_{Critical} = 4\frac{T}{D}$. Where T is the thickness and D is diameter. Therefore, for different GO flake samples, having polydispersity in their shape and lateral size, the critical concentration for the isotropic to nematic phase transition changes. Monolayer GO flakes having a large lateral size, at a concentration much lower than smaller and thicker GO flakes, form the nematic phase [74], [75]. Polydisperse disk systems are normally anticipated to exhibits only a discotic nematic phase, but a GO LC with high concentration can show a higher order by lamellar phase and helical LC assembly [9], [76].

1.4 Optical Properties and Birefringence of LCs

When light propagates in an explicit direction as a plane wave, an ellipse orthogonal to the propagation direction indicates the polarization of the light. The polarization ellipse can be divided into two linearly polarized waves along two axes perpendicular to each other with a definite phase relationship. The two linearly-polarized propagating waves have an equivalent

phase velocity c/n_{medium}, where c is the speed of light and n is the refractive index in an isotropic medium, Figure 1-8a. Instead, the optical properties of LCs as anisotropic medium are similar to uniaxial crystals, in a way that an incident light faces with unlike refractive indices when it oscillates in the plane perpendicular or parallel or to the director. Consequently, the two linearly-polarized waves pass through the LC with a dissimilar phase velocity as showed in Figure 1-8b. This phenomenon is birefringence. Birefringence is one of the most noticeable properties of LCs that differentiate them from ordinary isotropic liquids. It is the characteristic of LCs that not only makes them unique for their special application, but it is also very useful for studying their structure [77].

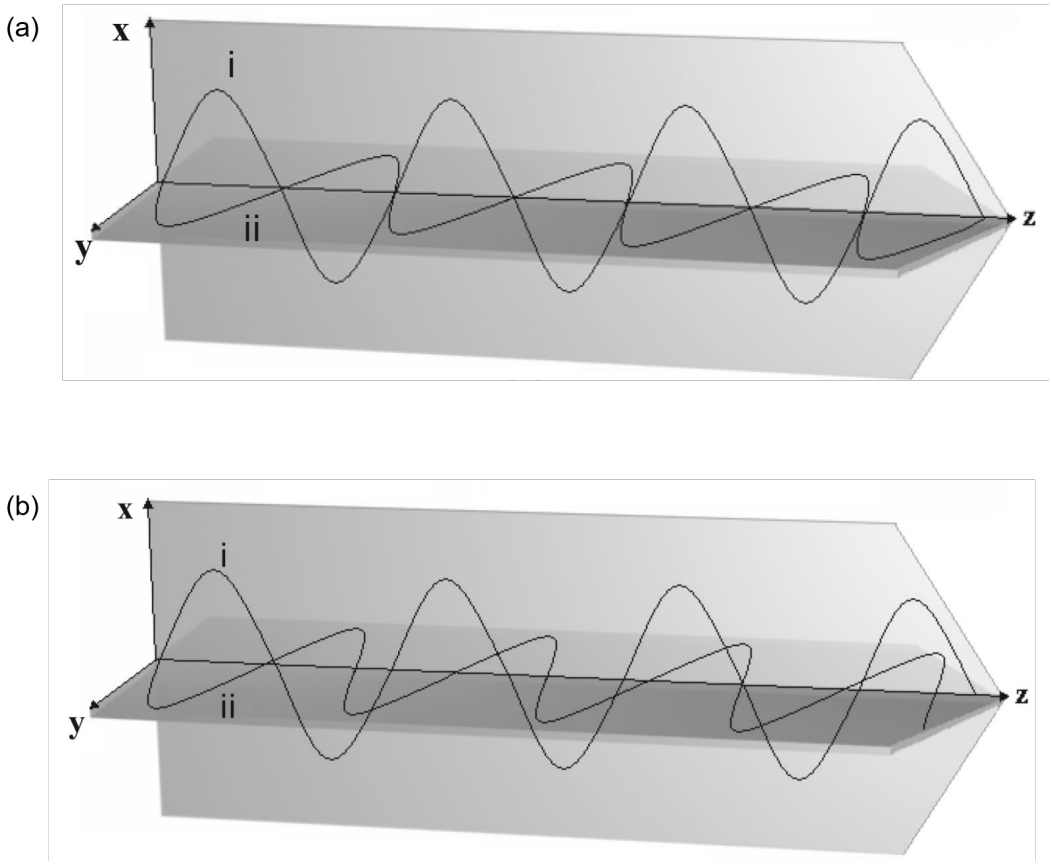

Figure 1-8. Propagation of light in (a) an isotropic medium, (b) in a LC (uniaxial medium). Reproduced from reference [77] with permission from Springer Nature.

In a simple liquid, refraction of an incident light beam agrees with Snell's law of refraction, as the refractive index of an isotropic liquid is independent of the incident light beam direction. However, for anisotropic materials like LCs, the refractive index is subjected to the light propagation direction. A light beam passing through a LC is divided into two components with perpendicular polarizations. One called the ordinary ray as travels with the same speed in every direction through the LC, and one called the extraordinary ray as travels with a speed that is dependent on the propagation direction within the LC. Therefore, the ordinary and extraordinary rays pass through the LC (as a birefringent medium) at unlike speeds, since they experience slightly dissimilar electrical environment i.e., indices of refraction, respectively n_o and n_e. This results in a phase difference δ i.e., different polarization ellipse at the end of the LCs, given by

$$\delta = \frac{2\pi}{\lambda}(n_e - n_o)d$$

where λ is the wavelength of incident beam line in vacuum and d is the distance that the beam traveled in the LC. For LC electro-optic switching cells d is equivalent to the cell gap and the beam light having different wavelengths (colors) experience different δ. The LC sample thickness, d, is an important factor, since the phase shift accumulates as long as the light propagates in the LC. Once the phase difference is equal to 2π, the wave turn back to its initial polarization state [77]–[79].

When the ordinary and extraordinary rays come out of LC films, still they vibrate at right angles with respect to each other. Nevertheless, the combination of these waves that traverse the analyzer vibrate in the same plane, Figure 1-9. Since one wave with respect to the other is retarded, constructive or destructive interference happens between the waves when they traverse the analyzer. Consequently, between crossed polarizers LCs obtain a spectrum of color when we observe them using a white light. Generally, after the polarizer, the incoming linearly

polarized light to a LC is transformed to elliptically polarized light, with a component that can traverse the crossed analyzer; hence, the LC sample looks bright. The intensity of transmitted light is given by

$$I = I_0 \sin^2 2\varphi \sin^2 \frac{\delta}{2}$$

where I_0 is the light intensity after the polarizer and φ is the angle between the analyzer and the optic axis of the LC. In the above equation, the first term mainly defines the variations in transmitted light intensity when rotating a LC sample between crossed polarizers and the second term is in charge for the attractive colors of the liquid crystal textures [78]–[80].

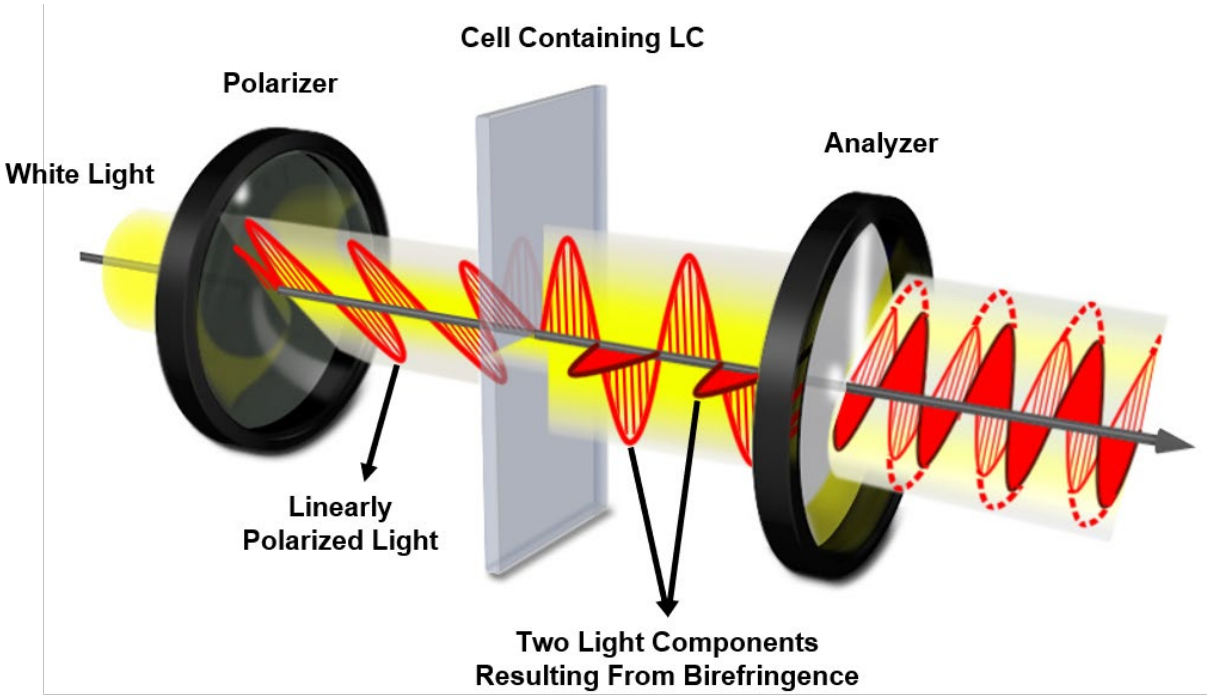

Figure 1-9. Liquid crystal between crossed polarizers

1.5 GO LCs Under External Fields

2D colloidal LCs have the basic properties of fluid but with orientational or positional orderings, similar to LCs of small molecules. Unsurprisingly, external fields including flow, space confinement, electrical and magnetic fields affect the intrinsic assembly of 2D colloids LCs. The fluid nature of 2D colloidal LCs enables modifying their order by these fields as well, to change their rheological, optical properties and performances.

In dispersions of anisotropic colloids with 1D and 2D morphology, shear induced birefringence is a typical phenomenon. Langmuir documented the primary systematic explanation of shear birefringence of 2D colloids [81]. In isotropic phase of colloids, flow can form a temporary parallel orientation of particles, and the formed birefringence declines with a short relaxation time. One of the rheology properties of 2D colloid fluid is the decreasing of viscosity when shear rate raises, together with emergence of birefringence. Like polymeric LCs with anisotropic mesogen units, colloid LCs show reduced viscosity by starting shearing, Figure 1-10a, due to shear-induced alignment of the particles, [82], [83]. In addition, it is revealed that the shearing process of GO suspensions is accompanying with a rise of the flatness of aligned particles, but not just an enhancement of their orientation order [84]. This phenomenon is contrary to other recognized platelet systems such as disc-like clay, mineral and organoclay particles [85], [86]. Remarkably, it was found that the distance between GO flakes decreases with increasing shear rate, which is because of an under shear flattening effect, Figure 1-10b [30], [84].

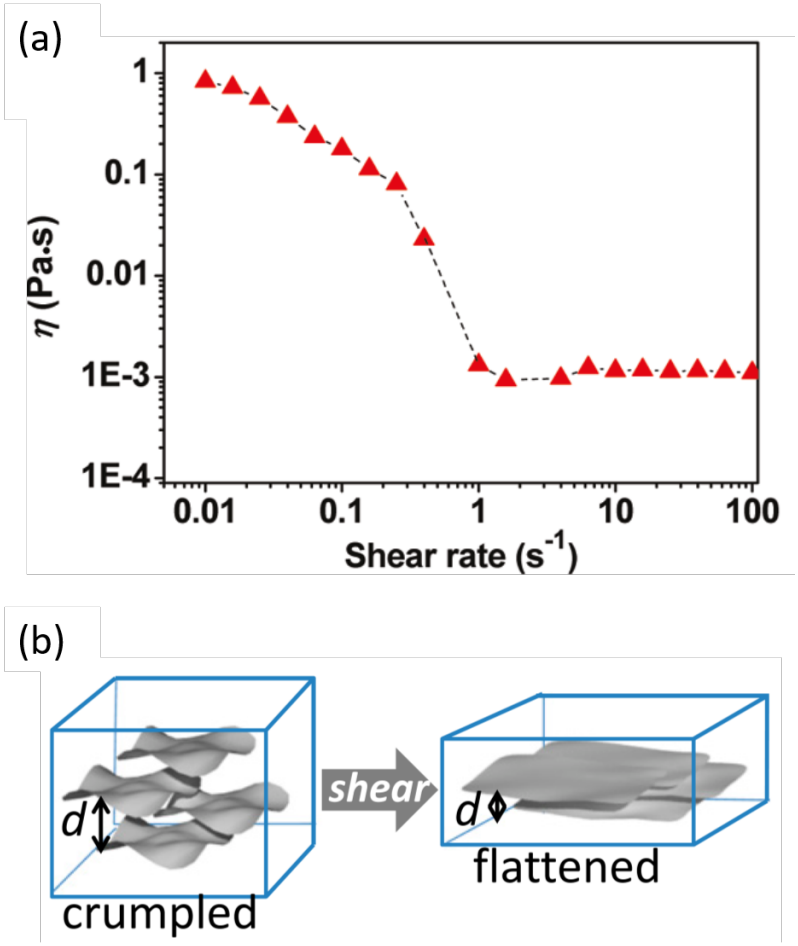

Figure 1-10. (a) Viscosity of GO aqueous dispersion as a function of shear rate. Reproduced from reference [83] with permission from John Wiley and Sons. (b) Sketch of the shear-induced flattening of the GO flakes. Reproduced from reference [84] with permission from PNAS.

The alignment of 2D colloids can also be controlled by external electric and magnetic fields. Applying electric field can create anisotropic dipole moments in particles, highest along the plane of particles and lowest in the normal direction, Figure 1-11. This results in an orientational order along their long axis under the electric field [87], [88]. Under the magnetic field, the anisotropic magnetic susceptibility tensor stimulates the alignment of colloids [89]. External magnetic and electric field are the efficient methods to adjust and control the internal assembly of 2D colloids dispersions.

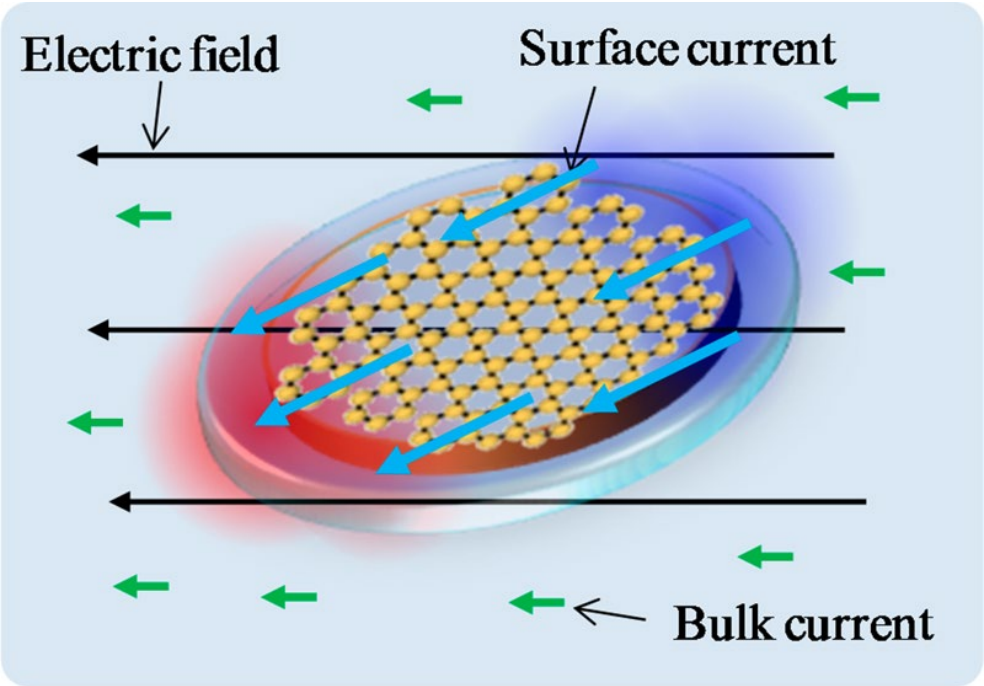

Figure 1-11. A large polarization is quickly achieved on a GO flake under the application of an electric field due to a large dissimilarity between the bulk and surface conductivities, producing dipolar charge distribution. Reproduced from reference [90] with permission from ACS.

When GO LC was discovered for first time, it was found also that an external stimulus, like applying a magnetic field, can align the LC phase, Figure 1-12. Because GO shows a magnetic susceptibility, the orientation of GO LC can be changed by external magnetic field. However, to reach a perfect alignment, several hours was needed since GO flakes have a weak intrinsic magnetism. In GO dispersion when a strong magnetic field is applied, the domains with unlike orientations would reorient gradually and form a uniform domain. The reorientation of GO flakes using magnetic field can be enhanced for their perfect alignment when GO flakes were functionalized by magnetic nanoparticles [30], [91].

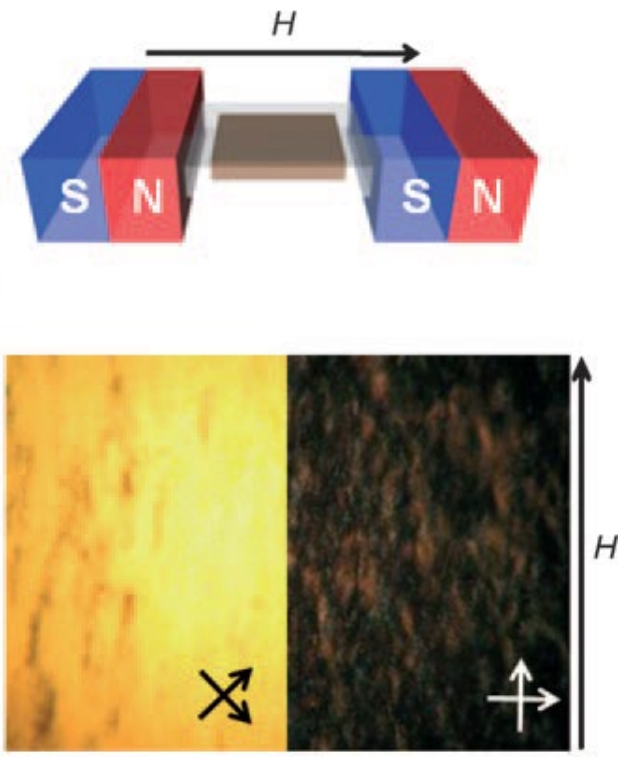

Figure 1-12. Magnetic-field-induced of GO flakes. Top: schematic for magnetic field application. Reproduced from reference [91] with permission from Angewandte Chemie International Edition.

To reorient the negatively charged GO flakes and control their alignment, it was expected that electrical field should be an efficient stimulus. When GO LC was discovered, an attempt was made to perform electric-field-induced alignment of GO flakes using a direct current (DC) field. However, because of the electrophoretic migration of charged GO flakes under a DC field or low-frequency electric field, the GO flakes reorientation was not possible, as their electrochemically reduction happens at cathodes [91]–[95]. The first electro-optical switching of GO flakes was reported in 2014, by using alternating-current (AC) field with a high-frequency (10 kHz) to stop the electrophoretic migration, Figure 1-13a [96].

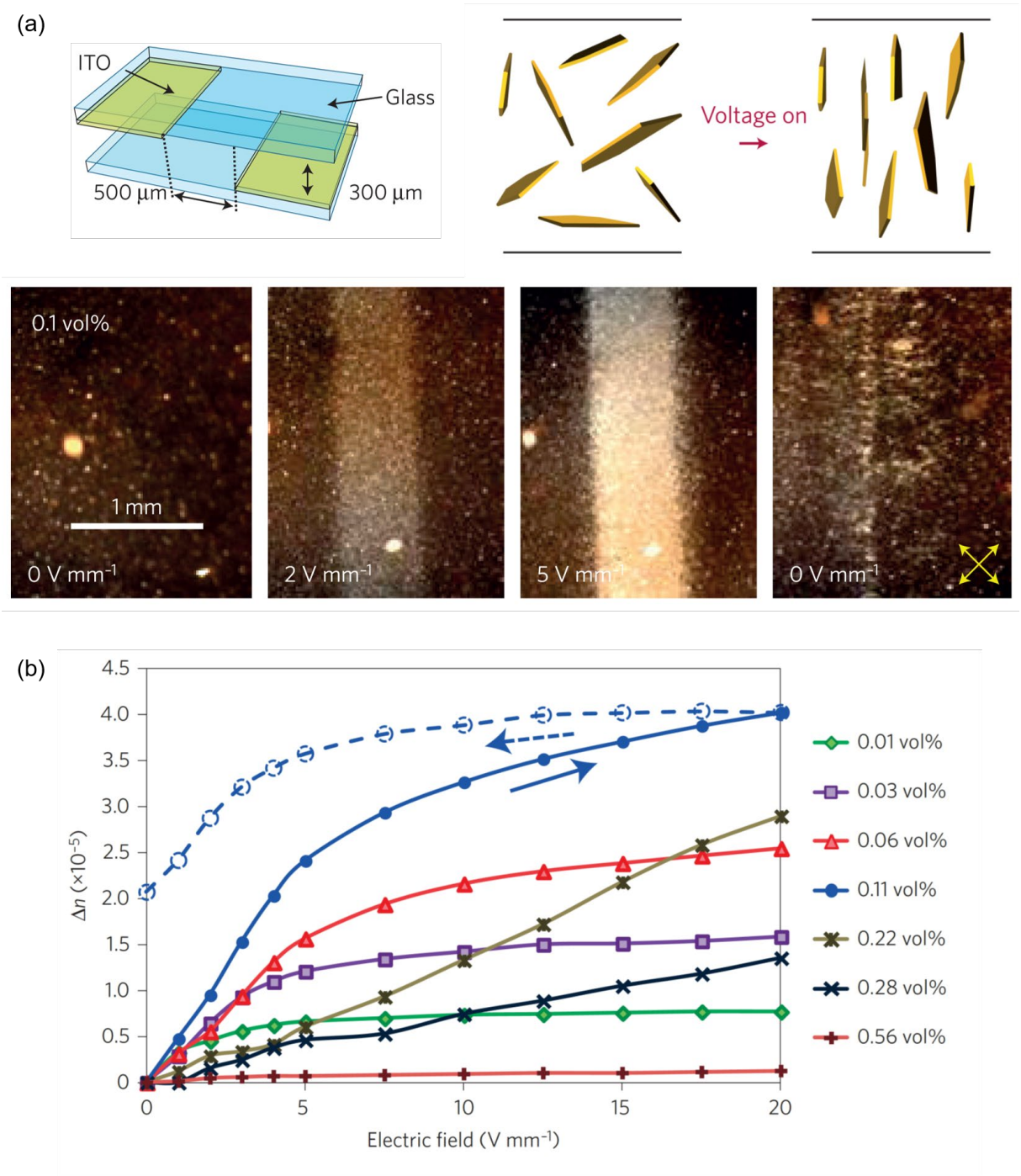

Figure 1-13. (a) Electro-optical switching of biphasic 0.1 vol% GO dispersion using 10 kHz AC field, and before and after switching; top: schematic for used cell design (left) and the field-induced orientation of GO LCs expected at very low GO concentrations (right), when the inter-flake interactions are effectively small. (b) Measured field-induced birefringence for different concentration. Reproduced from reference [96], [97] with permission from Springer Nature.

It was demonstrated that an AC electric field can effectively aligned biphasic GO LCs with a high Kerr coefficient, as a strong birefringence was detected for the dilute GO dispersion under polarized light, proving the high sensitivity of GO flakes to the electric field. The relaxation of such a field-induced alignment and the vanishing of birefringence was observed, very shortly after switching off the electric field. Moreover, the study on the effect of GO flakes concentration and their lateral size on GO electro-optical switching properties revealed that for a flake size of 5 μm, a concentration of 0.11 vol% gives the highest birefringence, Figure 1-13b. For the 5 μm GO sample, the critical concentration for having pure nematic phase was 1.1 vol% and up to 20 V/mm no change was observed in the nematic GO cell. The GO electro-optical switching was not possible for pure LC phases because LC suspensions of small size GO flakes are made of a high concentration of the flakes resulting in high inter-flake interactions and preventing their reorientation [9], [96], [97].

The optical switching of GO flakes suggesting the potential application of GO LCs as an innovative class of liquid crystal display (LCD). GO LCs have shown large Kerr coefficients due to their high polarizability anisotropy and the Onsager excluded-volume effect. The great response of GO LC phases to external stimulations is successfully investigated for applications in electro-optic devices. Tuning the direction and extent of the electric field, makes it possible to control the direction of induces alignment and assembly in GO LC for various applications [96]–[98].

Chapter 2: Large Graphene Oxide

2.1 Graphene oxide flakes

2.1.1 Graphene oxide preparation

The Graphene oxide (GO) flakes used in this dissertation was provided to LC Nano group by Dr. Stéphane Campidelli. A GO suspension with 2 mg/mL concentration, which was synthesized by a modified chemical exfoliation method with a procedure based on the Hummers' method [99].

In this method, 0.5 g of graphite, 25 mL of concentrated H_2SO_4 and 2 g of $NaNO_3$ were mixed at 0°C. While controlling the mixture stirring temperature at 0°C, 3 g of $KMnO_4$ was added slowly. At the end of this step the mixture was kept on stirring for 90 min at 0°C and then for 2h at 35°C. 50 mL of deionized water (18.2 MΩ-cm) was then gently added before keeping the solution stirring for 30 min. 2.5 mL of H_2O_2 (30%) was added and the stirring resumed for 15 min. The mixture was then mostly composed of graphite oxide. After the obtained mixture went through five continuous steps of: 1) centrifugation at 1600 rpm, 2) removal of 20 mL supernatant, 3) adding 20 mL distilled water, 4) agitation with a laboratory vortex shaker enabling exfoliation of GO. The last agitation step led to the formation of a gel-like structure composed of a superior phase with a high concentration of large GO flakes and an inferior phase with remaining unexfoliated graphite oxide which was eliminated after centrifugation [100].

2.1.2 Shape and size

To determine the size and shape of the GO flakes, I performed Scanning Electron Microscopy (SEM) measurements using a JSM-6010LA microscope. For this purpose, I prepared a GO suspension with very low concentration, 0.002 mg/mL, by diluting the 2 mg/mL mother suspension with deionized water, and then depositing the GO flakes on cleaned silicon wafers by drop casting method. Figure 2-1 shows the GO flakes on silicon wafer in different magnifications.

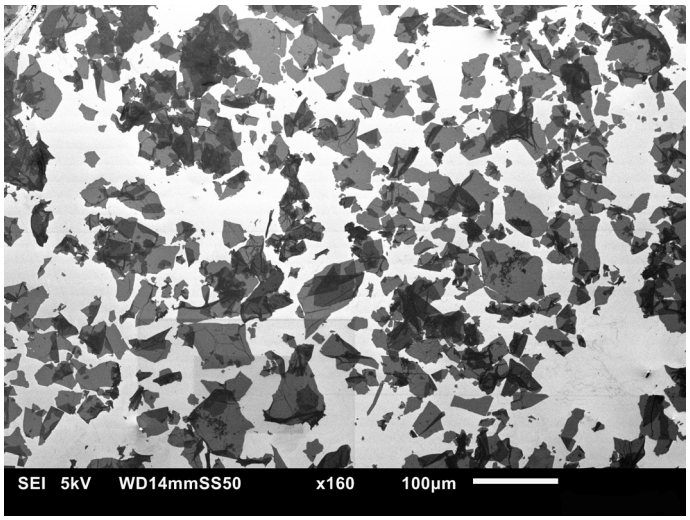

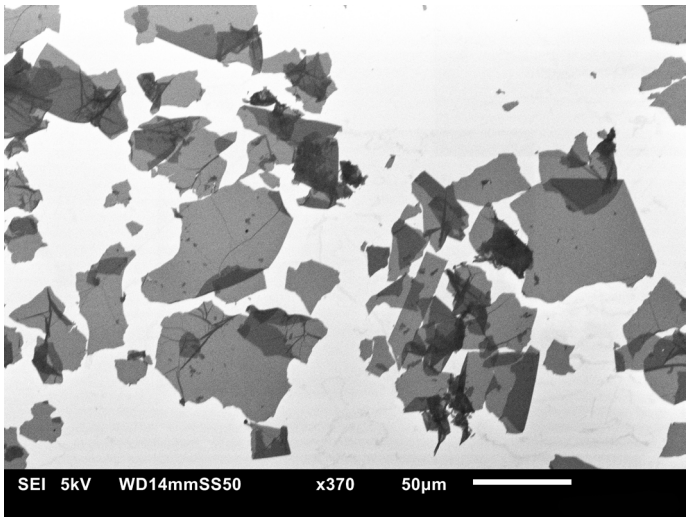

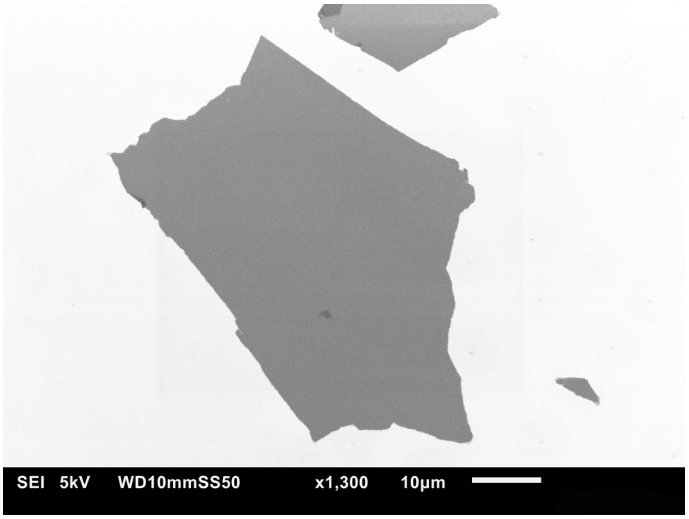

Figure 2-1. SEM images of GO flakes deposited on a silicon substrate, under different magnifications

The GO flakes are highly single layer. Generally, GO flakes are dissimilar in shape, however we can assume that they have a disk shape since they have a very high surface area in comparison with their thickness. They also vary in size, but they are generally quite large, up to more than 100 micrometers. I estimated the average size of the GO flakes by evaluating their average widths on SEM images, Figure 2-2. From my measurements, I obtained a mean diameter ~ 38 µm for the GO flakes.

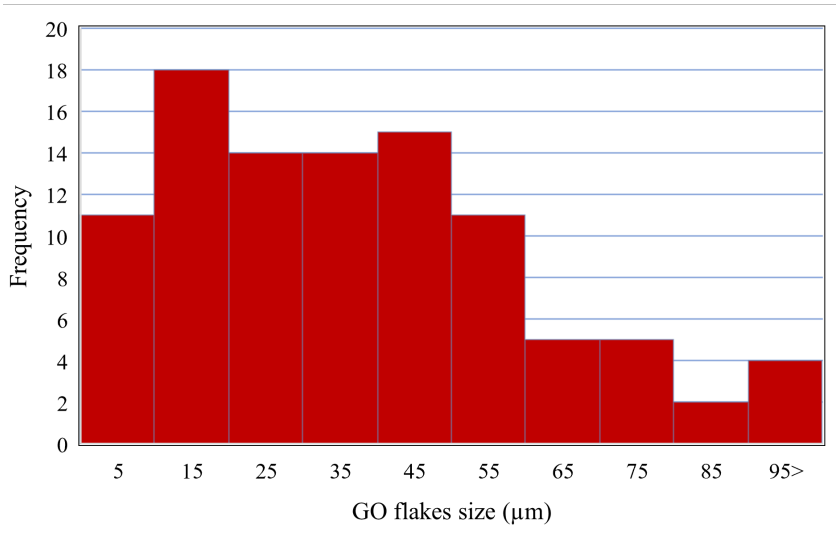

Figure 2-2. The GO flakes size distribution, evaluated from SEM images

2.1.3 Thickness

I analyzed GO flakes by Atomic Force Microscopy (AFM) in the ambient condition (in air), by a Veeco Multimode V and using silicon tips, to determine their thickness. GO flakes are single layer of carbon atom with the attached functional groups, and they are very soft materials. They normally develop a liquid meniscus layer on their surface when they are deposited on a silicon wafer which is one of the major problems of scanning in ambient air. For these reasons, I used the tapping mode for my AFM measurements, which is the best mode to work in ambient air for soft materials.

In tapping mode, the tip (cantilever) is driven in a way to have an up and down oscillation at or near its resonance frequency. The cantilever oscillations are kept steady by keeping constant the frequency and amplitude of the driving signal, until tip does not have an interaction with the GO flake surface. When the tip gets closer to the sample and the cantilever interacts with forces like Van der Waals forces, dipole-dipole interactions, electrostatic forces, and short-range repulsions, the amplitude of the cantilever's oscillation shift. The distance of the cantilever from the sample is controlled by an electronic servo, which uses the shift of amplitude as a parameter to adjusts the height by preserving a set cantilever oscillation amplitude when the cantilever scans the sample. This way by imaging of the force interaction of tip with the flake surface, an image of GO flake is created via tapping AFM [101], [102].

Figure 2-3 shows an AFM image of a large flake. The surface of flake looks smooth in areas that the flakes is not wrinkled or folded and there is no difference between middle and edge of flake. This indicates that the entire flake has a homogeneous structure. To estimate the thickness of the flake, I measured the average height profile at edge which is presented as a yellow I shape line in Figure 2-3. The middle line shows the direction of the profile, and the area between two end marker lines show the area over that the average profile was obtained.

By fitting a step line to the measured height profile, I obtained ~1.3-1.6 nm for GO flakes thickness which agrees with what is reported for monolayers of GO flakes [103]–[106]. It is higher than ~0.8 nm graphene thickness, and it is expected that GO has a thickness higher that graphene because of functional groups of GO [107], [108].

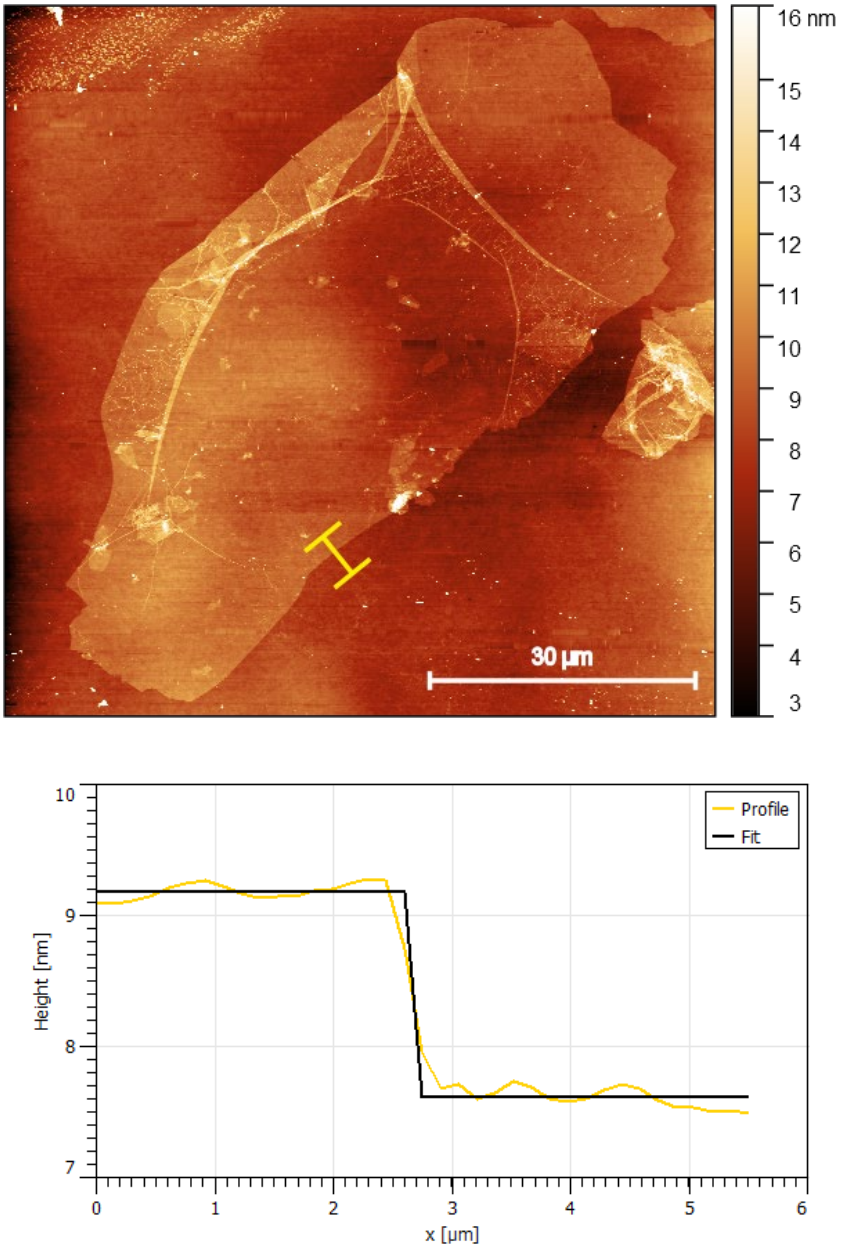

Figure 2-3. AFM image of a single layer GO flake on a silicon wafer and the height profile measurement at edge of the GO flake.

For a more precise measurements, I also performed a height profile measurement on two flakes on top of each other to avoid the effect of different Van der Waals force interaction between tip with GO flakes and silicon wafer, Figure 2-4. This way, I measured the thickness of GO flakes ~ 0.8-0.9 nm, which is very close to the reported values for graphene thickness [30], [109]. From my measurements, dry GO single layer has a thickness similar to graphene and its functional groups does not have a remarkable effect on its thickness.

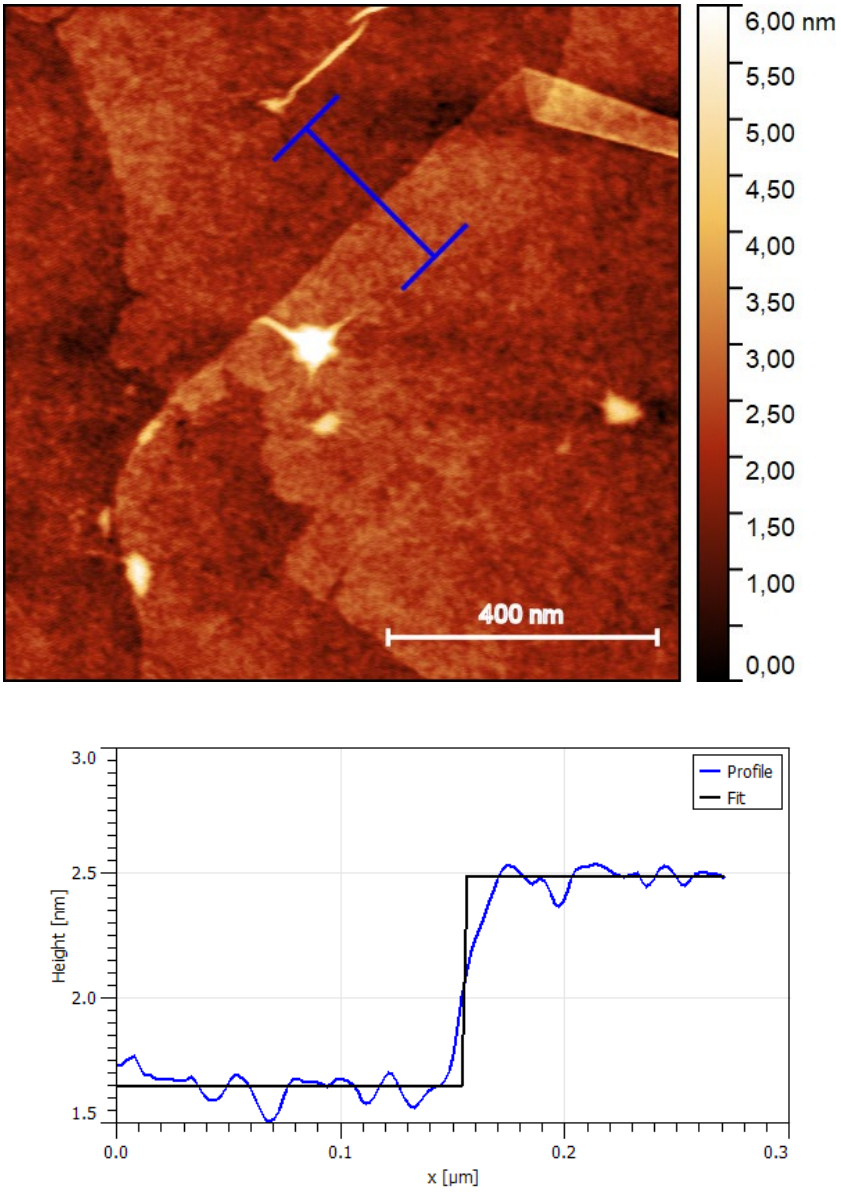

Figure 2-4. AFM image of two single layer GO flakes on top of each other and the height profile measurement at edge of the top GO flake.

2.2 Graphene Oxide Liquid Crystal

2.2.1 GO aqueous suspension

GO because of its dense oxygen functional groups is hydrophilic and it can easily disperse in water. For my studies, I used a 2 mg/mL GO flakes suspension as mother suspension, Figure 2-5a. The GO has dense C−O, C=O and O=C−OH oxygen functional groups, with estimated C:O ratio of ca. 1.25:1, for a similarly prepared GO [100]. Between crossed polarizers, GO aqueous suspension displays high brightness, due to birefringence, because of GO flakes order. GO flakes due to their shape and anisotropic ratio form discotic lyotropic nematic LC phase, Figure 2-5b.

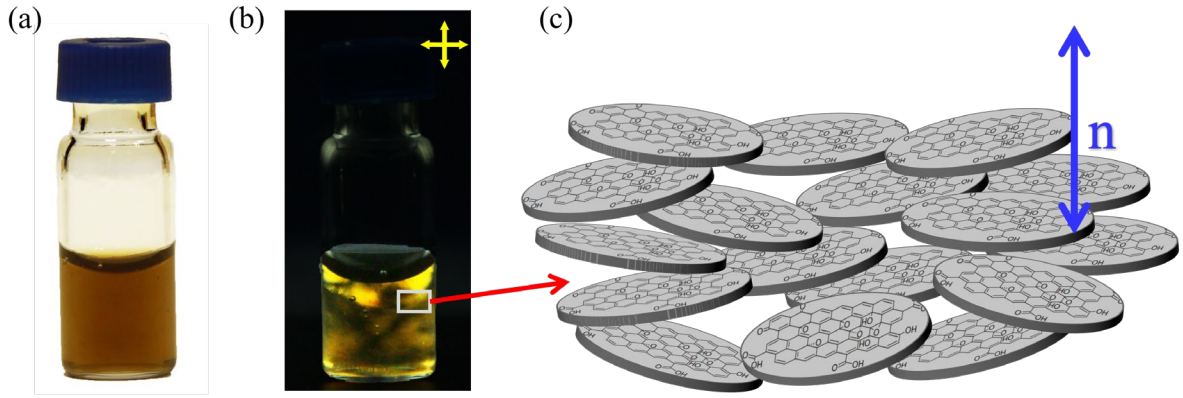

Figure 2-5. (a) 2 mg/mL GO aqueous suspension. (b) between crossed polarizers. (c) A schematic of GO flakes order in their aqueous suspension and their optical axis.

The high level of light transmission for GO suspensions is because of the large size of GO flakes and their small thickness. I prepared lower concentrations of GO suspension, by diluting the mother suspension with deionized water (18.2 MΩ-cm), Figure 2-6. Even very low concentration of GO suspension, 0.2 mg/mL, show birefringence between crossed polarizers

indicating already the appearance of ordering in GO flakes due to LC phase formation. The low birefringence is because of the very low GO concentration and the fact that they are biphasic i.e., a co-existence of isotropic and nematic phases. Due to the polydispersity of the GO flakes it is expected that a have quite wide bi-phase region and a pure nematic phase would appear as the concentration increases at a value depending on the suspension characteristics [11]. Being in biphasic region, the GO suspension is expected to phase separate into the nematic and isotropic phases with time.

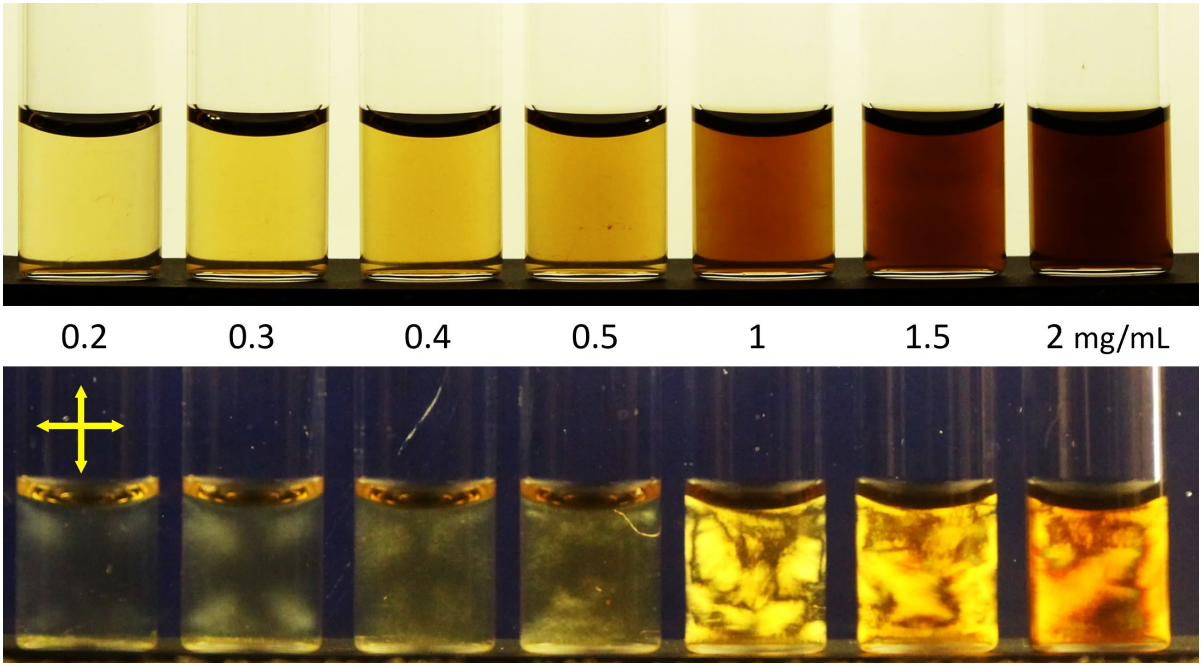

Figure 2-6. GO flakes dispersion with different concentrations (top) between crossed polarizers (down).

2.2.2 Stability of GO LC suspension

Time is an important variable for suspensions exhibiting phase co-existence. To study the stability of GO LC suspension over time for the separation of isotropic and nematic phases,

which is very important for their electro-optical applications, I prepared GO suspension with different concentration, from 2 to 0.05 mg/mL, Figure 2-7. 0.1 mg/mL (0.005 vol%) is the lowest concentration that shows a degree of brightness between crossed polarizers, on the first day of the preparation of the series of concentrations. For the phase separation studies, I kept the GO dispersions in an incubator (Memmert IPP55 Plus) at the constant temperature of 4 ºC to suppress the effect of temperature fluctuations, and to facilitate phase separation. I conducted the studies for 570 days and during this time, I took pictures of GO dispersions. Figure 2-7 also shows the GO suspensions after 57 days.

For high concentrations there was no phase separation indicating that they have a pure nematic phase; they were still homogeneous and without aggregates i.e., they are stable. GO LC phases is stable as the equilibrium state due to strong electrostatic repulsions between negatively charged flakes, confirmed by their negative zeta potential, and their high level of oxidation [110]–[112]. The zeta potential for the GO flakes were measured 36 ± 4 mV at Prof. Jang-Kun Song's laboratory at Sungkyunkwan University during my short visit to his labs. However, over time, for concentrations less than 0.7 mg/mL (0.035 vol%), I observed a phase separation. They separated over time into a top isotropic phase with low density and a bottom LC phase with high density and birefringent between crossed polarizers. Even at longer time until day 570, for concentrations higher than 0.7 mg/mL, I did not observe a phase separation or change, proving that 0.7 mg/ml (0.035 vol%) is the critical concentration for having pure GO LC phase.

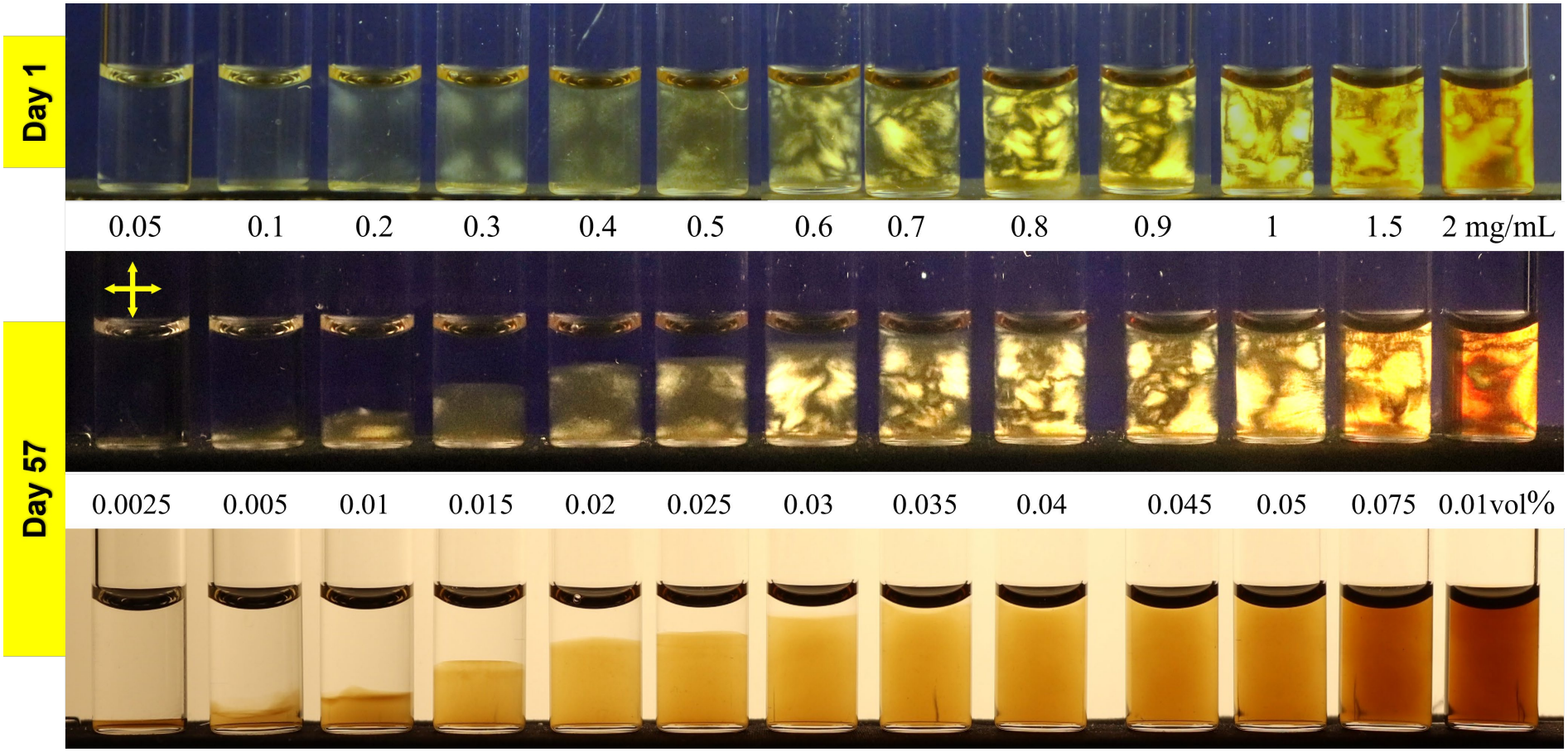

Figure 2-7. GO flakes dispersion with different concentrations on first day vs day 57 between crossed polarizers and without polarized light

2.2.3 GO LC equilibrium and critical concentration

An interesting point that I noticed during the phase separation studies was that for concentrations lower than 0.7 mg/mL, the separated bottom birefringent phases have similar intensity of the birefringence between crossed polarizers and it can be expected that they have the same density of the pure nematic phase, Figure 2-8. To check this point, I calculated the concentration of the bottom nematic phases as a function of the total GO concentration over time. I calculated the concentration of the bottom LC phase with an assumption that all or the vast majority of GO flakes are in the LC phase since top isotopic phases show zero level of birefringence and they are transparent without polarizers.

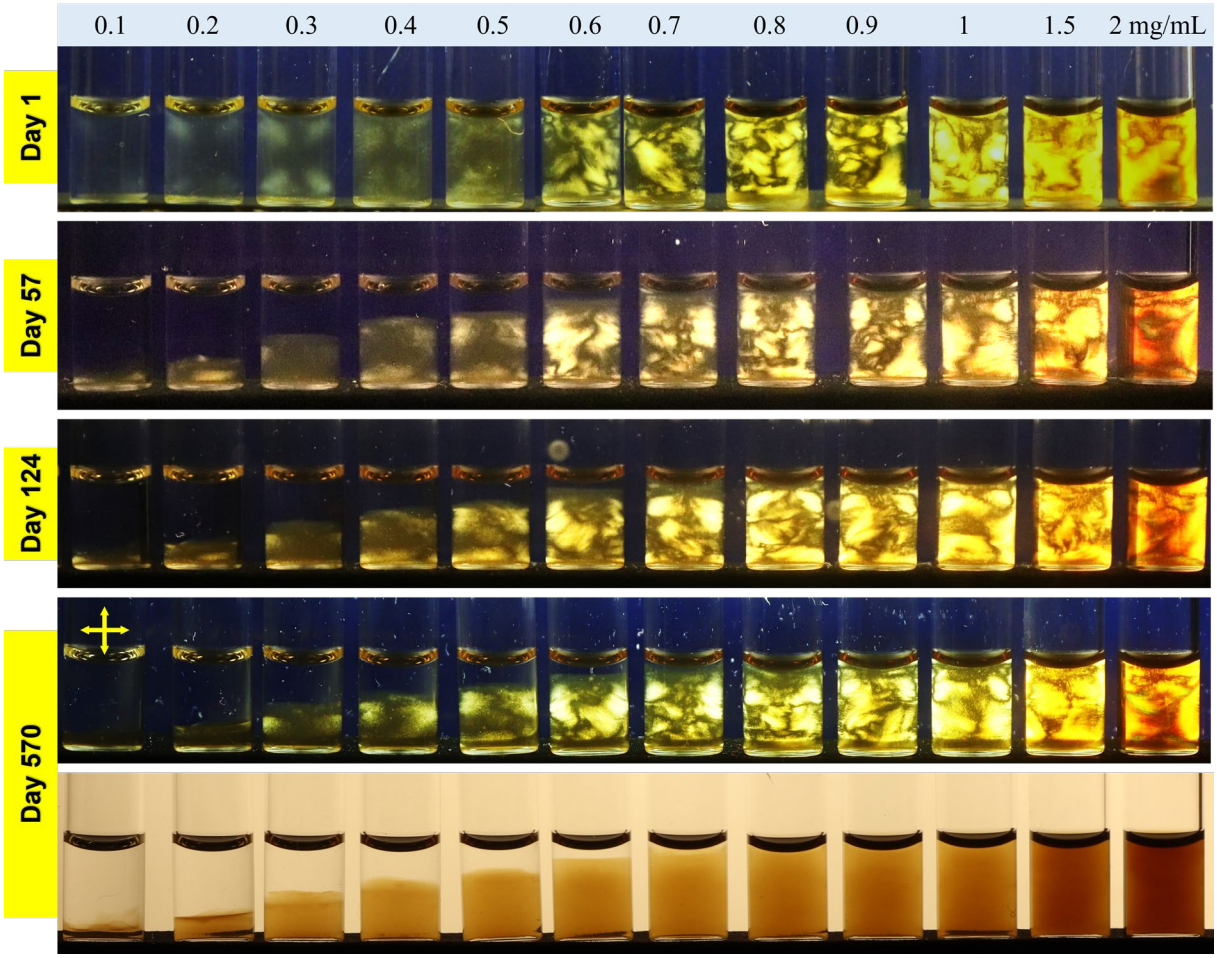

Figure 2-8. GO flakes dispersion with different concentrations day 1, day 57, day 124, day 570 between crossed polarizers; and day 570 without polarizers

To check this assumption by SEM, I removed the top phases by a micropipette, and I deposited them on silicon wafers to examine the remaining GO flakes in top phases. I observed that just a low number of very small flakes with sizes less than 2 µm remain in the top phases and the rest of flakes already moved to the bottom LC phases. I plotted the calculated concentrations for the samples in Figure 2-9. For each period of time, there is a threshold concentration after that we cannot see a phase separation in GO suspensions i.e., it is the equilibrium concentration for having LC phase, which are indicated as the vertical lines in the graph, and they increase by time. On the other hand, for each period of time, I calculated the average of all concentrations in the graph before the indicated concentration by the vertical lines, the equilibrium concentration, and I obtained values that are shown as the horizontal dash lines.

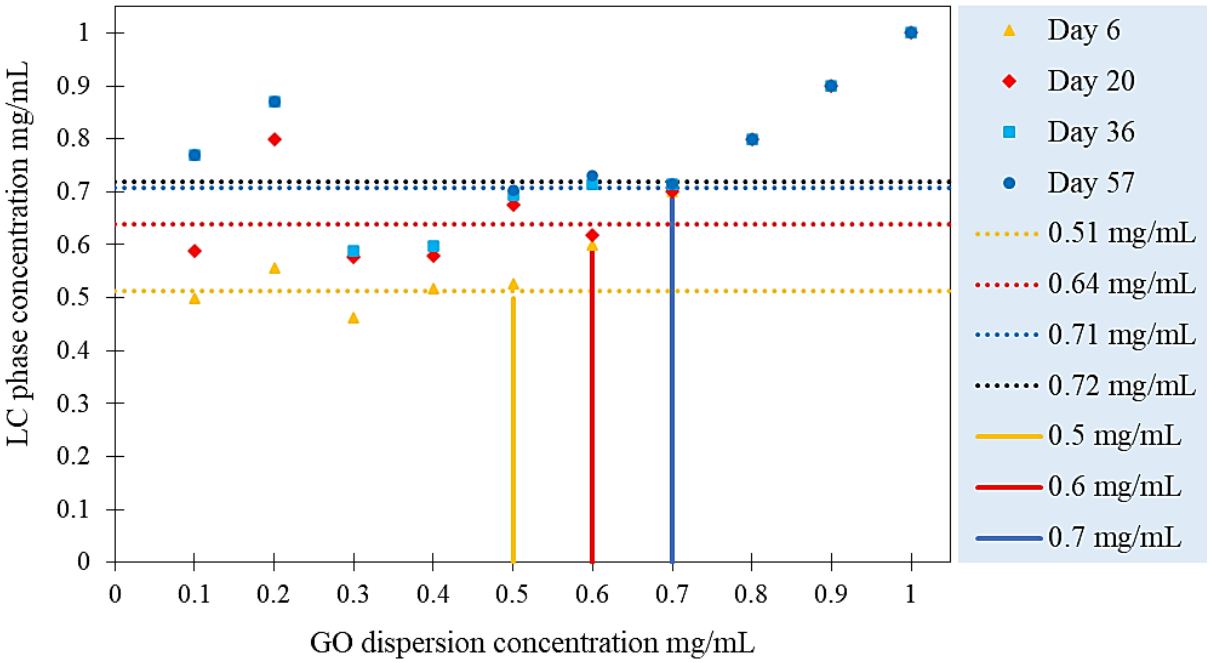

Figure 2-9. LC phase concentration versus GO suspension concentration for different study periods of samples in the stable condition. The vertical lines are the nematic phase threshold concentrations, whereas the horizontal lines correspond to the average LC concentrations below the thresholds, with corresponding values reported in the legend.

Interestingly, the concentrations corresponding to the dash lines are very close to the threshold concentrations indicated by the vertical lines in the graph for each time period, which confirms that the bottom phase has reached to the equilibrium concentration for the formation of the nematic phase in the bi-phase region until and including the threshold. The threshold is initially relative, but not absolute, since it is dependent on time until a steady-state is reached. At a closer look, the average values are slightly higher than the value for the equilibrium concentration and it is because of our assumption that all flakes move to bottom LC phase, when in fact some of small GO flakes remain in the supernatant isotropic phase [16], [100].

Figure 2-10, shows the average concentrations for the bottom LC measured in different times over 4 months. The equilibrium concentration for LC phase increases over time, the change decreases until it reaches to the critical concentration for having pure nematic phase, calculated equal to 0.7 mg/mL (0.035 vol%), and for higher concentration we have just pure nematic phase. The threshold concentration for isotropic- to -nematic phase transition for a disk-shaped colloid system can be calculated from the equation based on developed Onsager's theory for polydisperse very thin disks [11], [14], [24]:

$$\Phi_{th} = \frac{4T}{D}$$

Where Φ_{th} is the threshold volume fraction, T the thickness and D the diameter of the disk-shape colloids. The SEM and AFM measurements prove a high average aspect ratio (D/T) for the GO flakes of my studies, 1×10^3 - 7×10^5 with an average of 2.5×10^4. This very high aspect ratio results in a very low LC phase formation concentration threshold. For the GO flakes, I obtained ~ 0.01 vol% for the critical concentration of isotropic to nematic phase transition, which is lower than 0.035 vol% (0.7 mg/mL) that I obtained empirically. On the other hand, I used the experimentally found volume fraction threshold value, 0.035 vol %, and I calculate the effective thickness of GO flakes using the same formula; ~ 3 nm, larger than what we

measured for GO flakes by AFM. One explanation can be when GO flakes are dispersed in water, it is expected that the functional groups on their surface extend more outwards in water. The repulsive surface potential can also contribute to increase the value of the excluded volume. In addition, there is a water layer that can participate to the increase of the effective flake thickness; in real systems, the dimension of the disks can change in suspension due to species adsorbed around them including water molecules forming the so-called hydration shell. Since the thickness of disks is much smaller than their diameter, the relative change of dimension is larger for the thickness than for the diameter [24], [105], [110], [111]. Besides, GO flakes are very flexible materials leading them to have curvatures when they are in aqueous dispersion, which can also cause an increase in their effective thickness, which can be felt by other flakes [113].

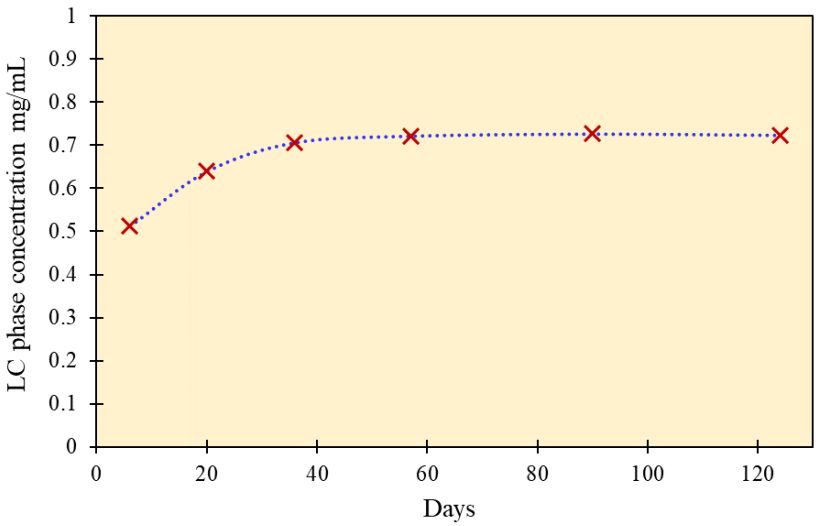

Figure 2-10. Time variation of the equilibrium concentration for the nematic phase formation over 4 months

2.2.4 GO LC Phase Diagram

To draw the phase diagram of the GO suspension, I calculated the LC volume fraction (LC volume/total volume) of different GO concentrations for 570 days, Figure 2-11. Although at

the first day, GO suspensions having a concentration higher than 0.4 mg/mL seem to have a full nematic phase, for the GO suspensions having a concentration less than 0.7 mg/mL, there was a phase separation. It indicates that indeed they are biphasic. Over time the LC volume fraction decreases until LC phase concentration reaches the critical concentration for having pure nematic phase and after that it stays constant. It means that 0.7 mg/mL (0.035 vol%) is the critical concentration for the isotropic to nematic phase transition of the GO aqueous suspension that I studied. The minimum value that I observed for the pure nematic phase is lower than what is reported in the literature, even for GO LC made of size selected large flakes [16]. The reason is directly related to the larger size of the GO flakes that I studied, compared to what typically studied and having an average size less than 10 µm [9], [16], [114]. Low concentration of pure nematic phase is very important for application of GO, for instance in electro-optical devices, for which the GO suspensions show excellent performance [19], [114]–[117]. The study of the stability of GO suspension over 570 days, clearly proves the stability of the low concentration nematic phase, and not occurring any phase separation during this time and beyond.

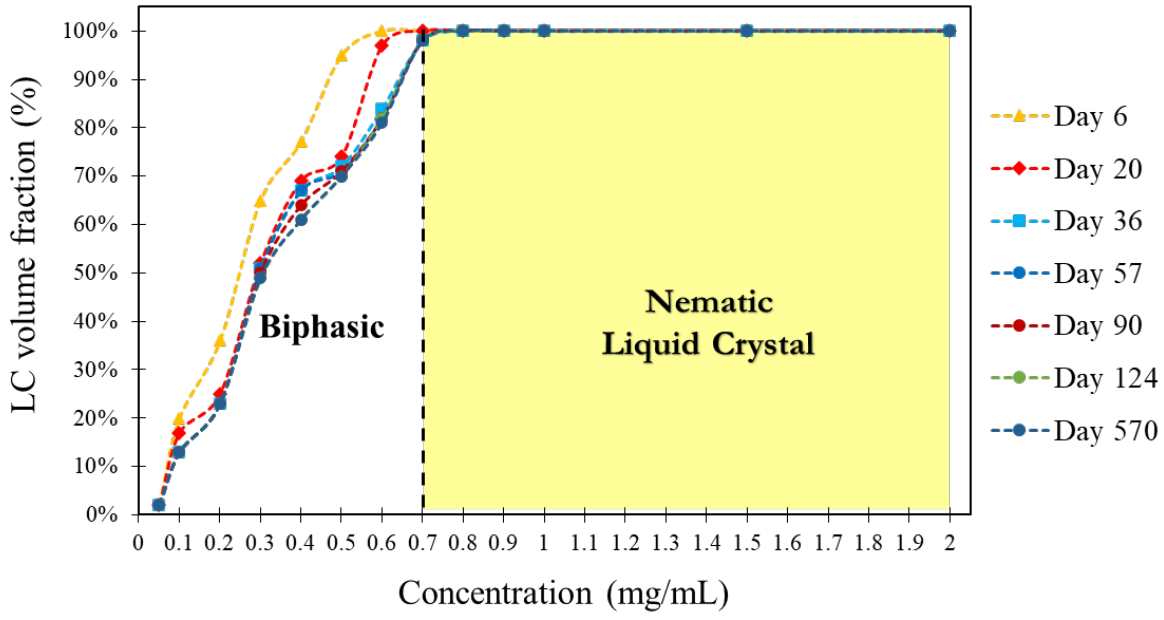

Figure 2-11. GO phase diagram: measured LC volume fraction over 570 days and the black dash line indicate the critical concentration, being border of bi-phase and LC phase.

Chapter 3: GO flakes behaviors in a confined space

3.1 Electric cell design

To perform electro-optical switching of GO flakes in their suspension, I made cells with a design showing in Figure 3-1. For the top and bottom substrates, I used cleaned microscope glass slides with a thickness of 1 mm. For experiments that a lower thickness of glass was needed, I used glass coverslips with thickness of 160 µm as the substrates. For electrodes, at the beginning I used different metals, copper, aluminum, and chromium; however eventually I just used cupper strips with thickness of 300 µm – 3 mm. Figure 3-1 shows also a cross section of a cell with cupper electrodes. The gap distance of cells (T) was determined by the thickness of electrodes, acting also as spacers. The distance between electrodes (W) could vary, but normally I used a distance of ~ 4 mm. To fill the cells with GO suspensions, I used a micropipette, while capillary was also effective in filling 300 µm cells. After filling cells, I sealed their two ends using a glue or pure beeswax.

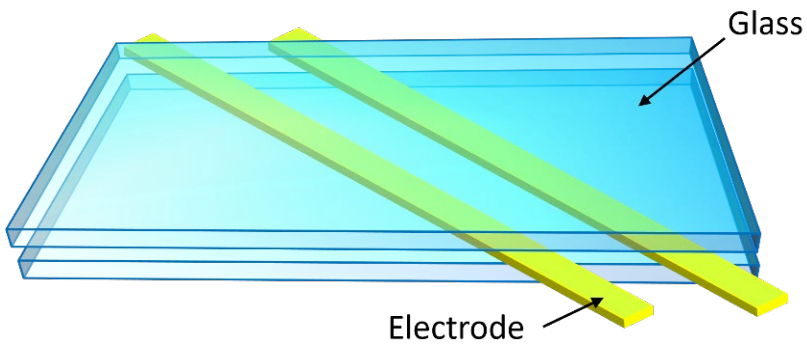

Figure 3-1. A schematic of the designed electric cell for electro-optical switching of GO flakes (top) and the cross section of the cell.

3.2 GO flakes order in LC phase

Before applying an electric field to GO flakes, I studied their orientational orders in the confined space of cells. Figure 3-2 shows a large view of a filled cell with 2 mg/mL concentration, having 7 mm wide and 3 mm gap distance, between crossed polarizers. I observed that GO dispersion along the whole cell is birefringent, revealing the vertical alignment of GO flakes to the glass substrates in the cell since GO flakes with planer alignment cannot have a contribution to birefringence. The large areas with different brightness, are results of different orientation of GO flakes in different part of the cell.

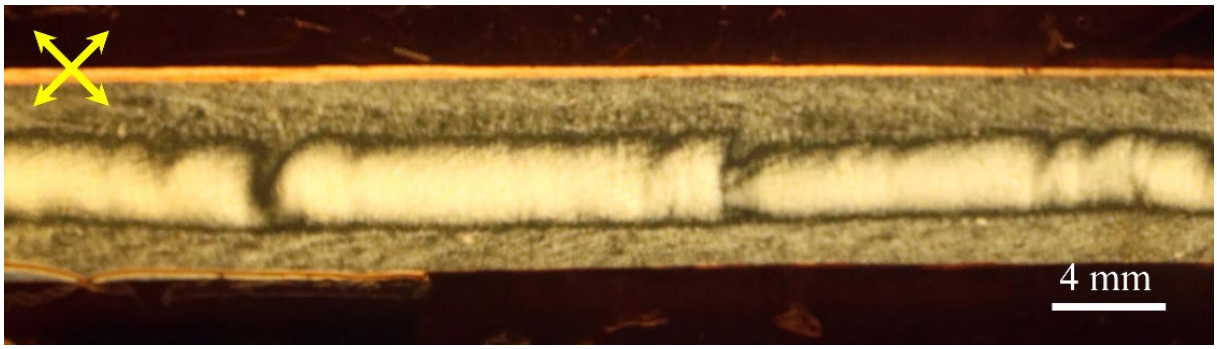

Figure 3-2. A top view of a cell with 3 mm cell gap (T), filled with 2 mg/mL GO suspension between crossed polarizers.

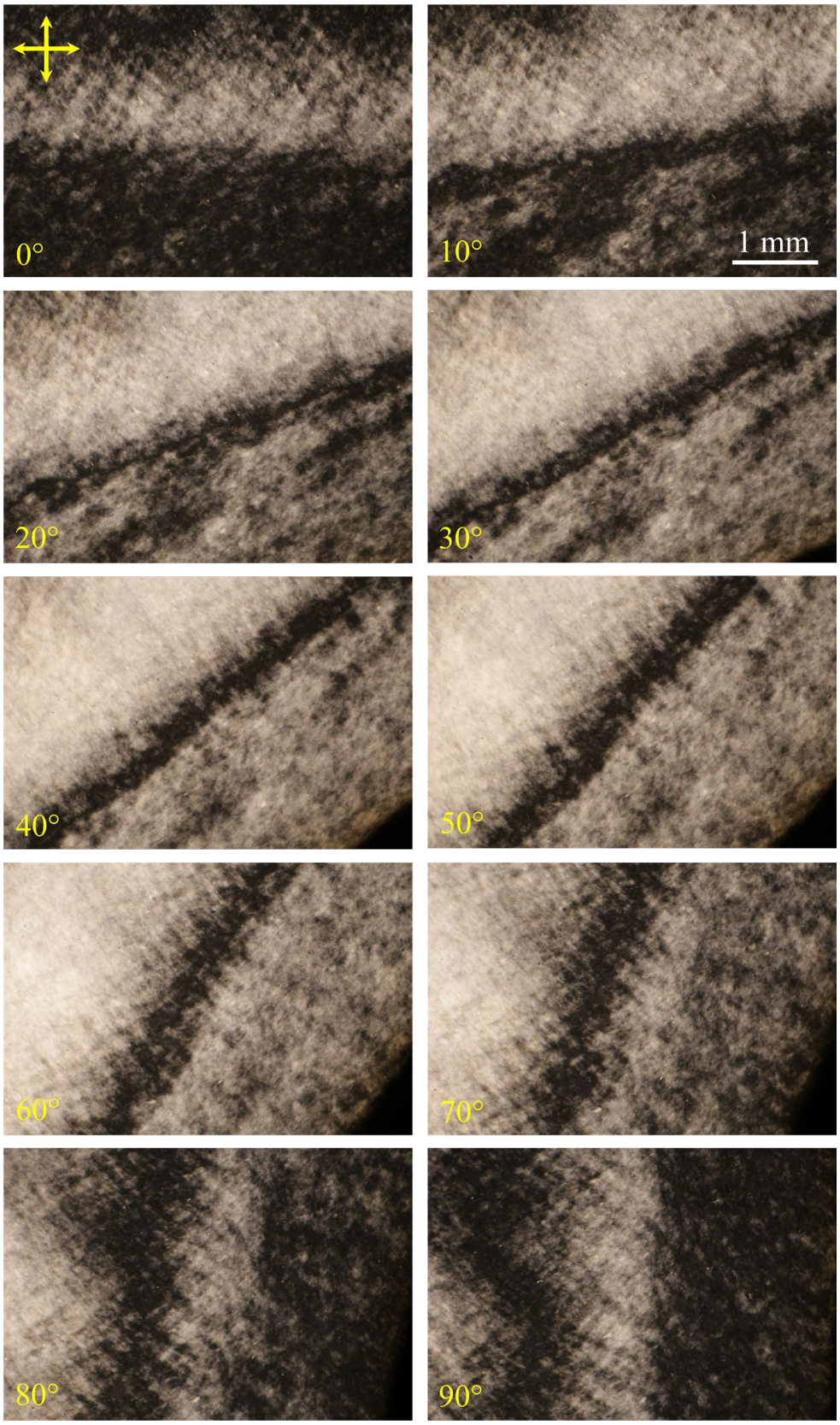

Figure 3-3. POM images of the 3 mm cell filled with 2 mg/mL GO suspension and rotated between crossed polarizers

For a better displaying the order of GO flakes in their liquid crystal phase, Figure 3-3 shows a closer look at the side of cell using polarized optical microscopy (POM) and by a 4x objective. POM observations were performed with a Nikon Eclipse LV100ND Microscope, equipped with a CANON EOS6D camera. The images captured when the cell was rotated on the rotary stage of the microscope, between the polarizer and the analyzer. The indicated angle (θ) on the POM images is the angle between the direction of electrodes (the cell side) and the polarizer (or the analyzer). In Figure 3-3, there is a clear difference in the degree of brightness, birefringence, in between areas close to the side walls and center of cell. The birefringence difference is because of the different angles that GO flakes have in different area in the cell. The transmitted intensity is proportional to the angle between the analyzer and the GO flakes direction φ, $I \propto I_0 sin^2 2\varphi$ and I_0 is the light intensity after the polarizer. The direction of the polarizer and analyzer are indicated in Figure 3-7, by crossed yellow arrows. At θ = 0°, the areas close to side and center of the cell are dark and by increasing θ, their degree of brightness initially increase and then decrease to get dark again at θ = 90°. These changes indicate that GO flakes have an orientational order parallel or perpendicular to analyzer at the side and center of the cell but is not similar in the whole cell area.

3.2.1 Determination of GO flakes orientation by a retardation plate

For GO flakes, the axis along the basal plane is the direction that the ordinary (o) ray passing through with ordinary refractive index (n_o) and it also represents the GO flake slow (high refractive index) axis, Figure 3-4. While the axes normal to plane is the direction that the extraordinary (e) ray passing through and having extra ordinary refractive index (n_e) and it is the fast axis of GO flake [14]. Hence, GO flakes is a negative birefringent material, $B = n_e - n_o < 0$. Knowing the slow and fast axis of GO flakes make it possible to determine the

average orientation of GO flakes using a full wave retardation plate (lambda λ plate). The full wave retardation plate is ideal for use with birefringent samples that have very low birefringence, only gray-level colors, when observed by POM.

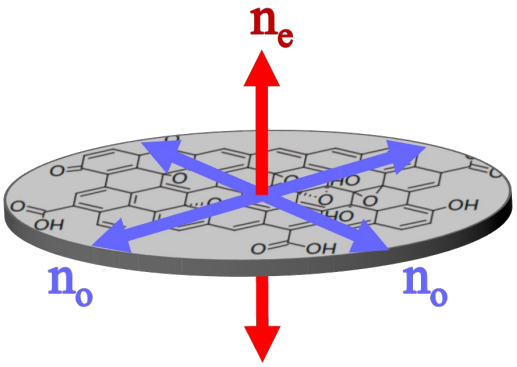

Figure 3-4. A schematic showing ordinary and extraordinary refractive indexes (respectively slow and fast axes) in a GO flake

The full wave retardation plate is a standard accessory that is usually employed to determine the birefringence sign (positive or negative) of a sample in POM. The retardation plate is also effective for enhancing contrast in weakly birefringent samples like GO. It is made to introduce a relative retardation of precisely one wavelength, usually 530 - 550 nanometers (in the green), between the ordinary and extraordinary rays going through the plate, if the birefringent retardation material is illuminated by a linearly polarized light that have a 45-degree incident angle to the slow or fast axis of the material. Consequently, green wavelengths are still linearly polarized when passing from the retardation plate and having the same orientation as before entering the retardation plate i.e., parallel to the polarizer. Hence, they do not pass the analyzer as they are perpendicular to it. On the other hand, the remaining light wavelengths when they pass through the retardation plate, all of them will face some level of retardation (less than a full wavelength) and they have different levels of elliptical polarization. Therefore, these wavelengths are not absorbed by the analyzer and can pass through it. Once the analyzer blocks just the green wavelengths, and subtracts them from white light, the result is a bright magenta-

red color. When a retardation plate is inserted between crossed polarizers in the microscope, the observed magenta color is a direct result of the combination of all visible light spectral colors, except the missing green wavelengths. The effect of a retardation plate on polarized white light is simplified in Figure 3-5a, by separately showing red, green, and blue light colors. In Figure 3-5a, without a sample between crossed polarizers, the linearly polarized red and blue light turn into elliptical polarized waves when they pass through the retardation plate, however the green light passes through the plate as a linearly polarized wave and then it is absorbed by the analyzer. Thus, only the red and blue light can pass the analyzer and they generate a spectrum of light, which looks like a bright magenta background in the microscope.

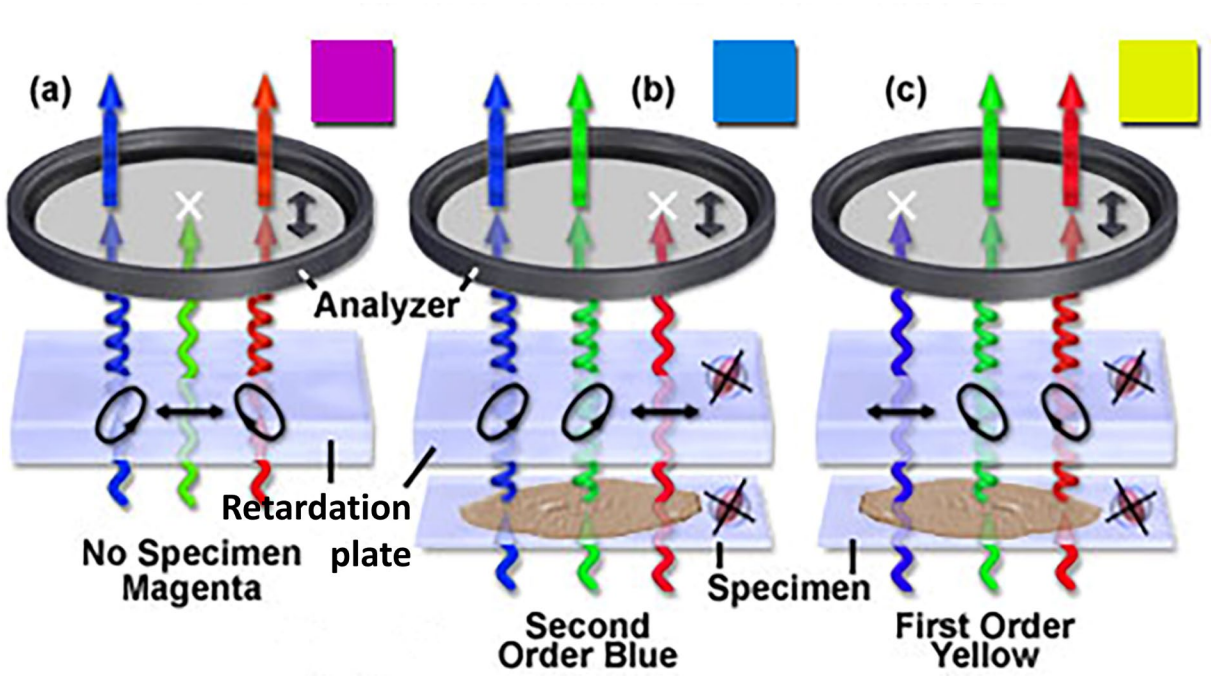

Figure 3-5. Schematic of the effect of a retardation plate on polarized white light that is simplified by separately showing red, green, and blue light colors. (a) without a specimen. (b) with a specimen having its slow axis parallel to the slow axis of the retardation plate, (c) the specimen rotated by 90 degrees between crossed polarizers [118].

The retardation plate can be used for simple uniaxial birefringent materials to determine the sign of birefringence i.e., if the extraordinary refractive index is higher or lower than the

ordinary refractive index. For an analysis of birefringence, specimens must first be oriented with its extraordinary or ordinary axis having 45-degree angle with respect to the microscope polarizer and analyzer. In Figure 3-5b, a birefringent specimen having positive birefringence is inserted into the optical pathway, in a way that its slow axis (with higher refractive index) is parallel to the slow axis of the retardation plate. As a result, the relative retardation is increased and since the phase difference δ is proportional path length (d) and it is given by $\delta = \frac{2\pi}{\lambda}(n_e - n_o)d$, the light wavelength that now showing linear polarized behavior is shifted to longer wavelengths i.e., red, which is then blocked by the analyzer. Elliptically polarized blue and green wavelengths that are not blocked by the analyzer eventually recombine to form a blue color. In Figure 3-5c, the specimen is rotated by 90 degrees between crossed polarizers in a way that its slow axis is perpendicular to the slow axis of the retardation plate now (or its fast axis is parallel to the slow axis of the plate). In this case, the relative retardation is decreased so the shorter wavelengths pass through the retardation plate as the linearly polarized light i.e., blue to be absorbed by the analyzer. The green and red color wavelengths are elliptically polarized, so they can pass through the analyzer, and their combination result is a yellow color [118], [119].

Figure 3-6 shows POM images of the 3 mm cells that was rotated on the rotary stage of the microscope when a retardation plate, 530 nm, is inserted between crossed polarizers in the microscope. A white arrow indicates the direction of the slow axis of the retardation plate, which has 45-degree angle with the polarizer and the analyzer. All the images consist of magenta-red, blue, and yellow colors which represent the different orientation of GO flakes. The normal POM images in Figure 3-3, already revealed that GO flakes should have a preferred orientational order parallel or perpendicular to the analyzer at the side and center of the cell. But in Figure 3-6 the different colors indicate that GO flakes have different orientational orders at the side and the center of the cell, and they are perpendicular to each other.

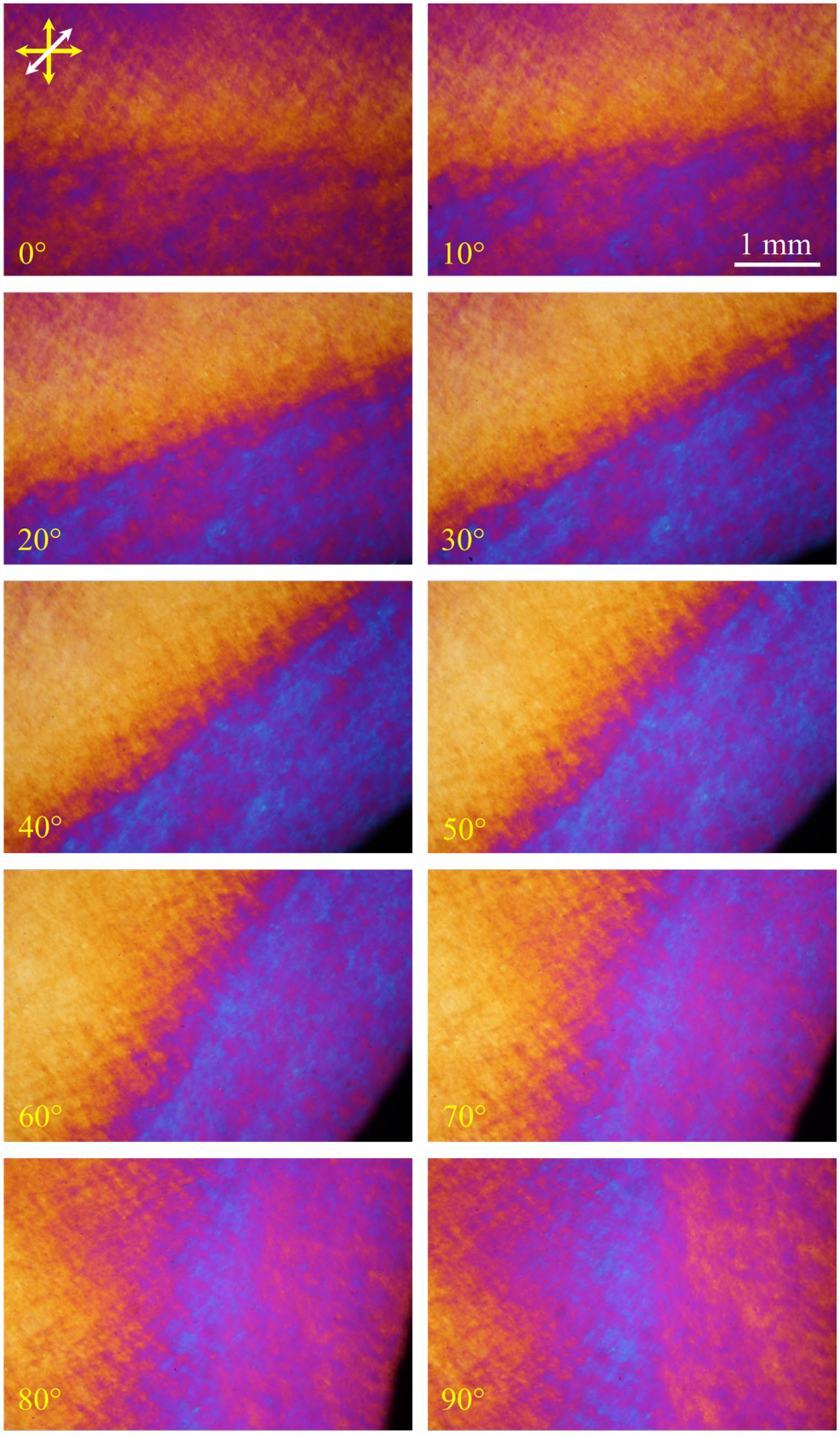

Figure 3-6. POM images, with a retardation plate, of the 3 mm cell filled with 2 mg/mL GO suspension and rotated between crossed polarizers

To carefully determine the orientation of GO flakes in the 3 mm cell, Figure 3-7a show its POM images when the cell is place between crossed polarizer in a way that its side walls (electrodes) make a 45-degree angle with the polarizer, $\theta = 45°$. At this cell position, I observed the maximum degree of brightness. However, the center of cell looks brighter in comparison with the side of the cell. Using the retardation plate in Figure 3-7b, the appearance of bluish color (addition of phase retardations) at center of the cell indicates that GO flakes have an average orientation that their slow axis is parallel to the slow axis of the retardation plate (the white arrow). This means that in area close to the center of cell, GO flakes have a preferred orientation order perpendicular to the side wall. Furthermore, the yellowish color at side of the cell indicates that at the side, GO flakes have an average orientation parallel to the side wall. Between bluish (at the center) and yellowish (at the side) areas, there is a narrow pinkish area where GO flakes have an orientation between perpendicular and parallel to the side wall and the transition of GO flakes orientation happens. This assembly of GO flakes is induced through a shear flow that is created by relative motion between the side electrodes and the GO dispersion, during filling the cell [113], [120]. In addition GO flakes may attach to electrodes and it can be a reason for their alignment parallel to the cell side [121]. Hence, at close distance to the electrodes, GO flakes prefer to have an orientation parallel to the side wall, and at larger distance, they have a different orientation. In Figure 3-7c-d, the 3 mm cell is anticlockwise rotated by 90 degrees. Without the retardation plate, the Figure 3-7c seem to be a mirror image of Figure 3-7a. However, in Figure 3-7d with the retardation plate, the position of blue and yellow colors is reversed, since the color are a direct result of GO flakes orientation that are reversed by 90 degrees rotation of the cell.

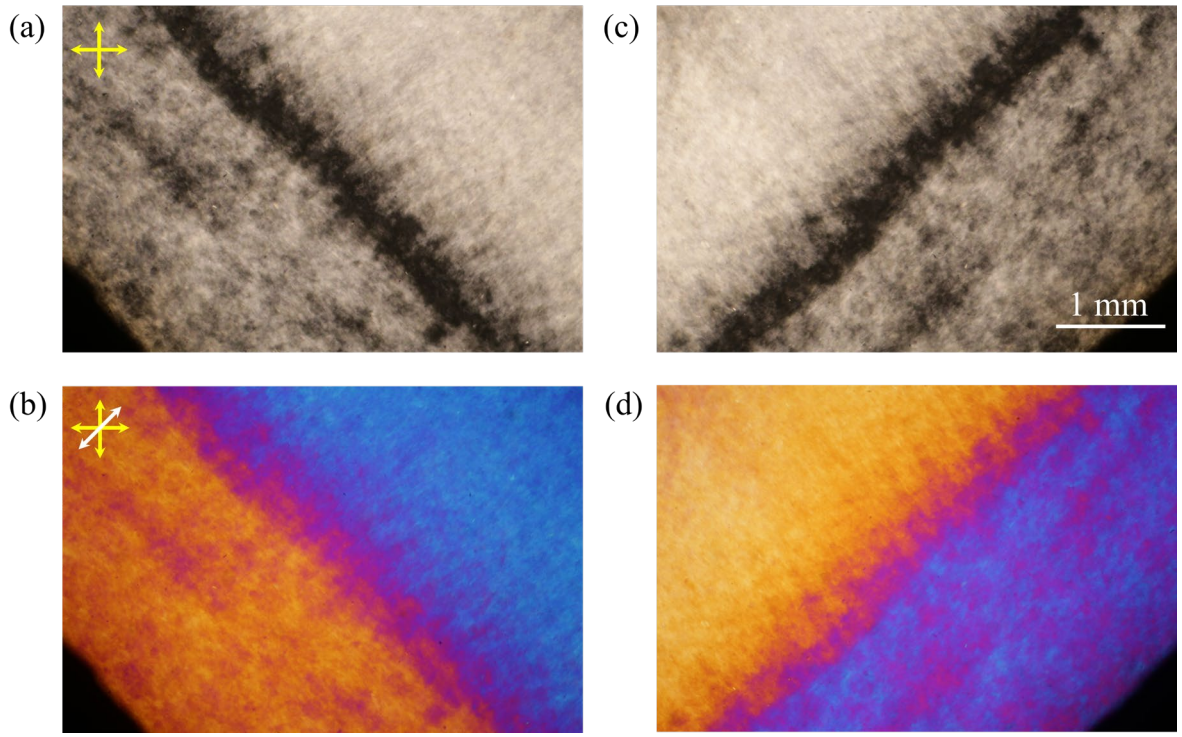

Figure 3-7. (a) POM image of the 3 mm cell filled with 2 mg/mL GO suspension, and its side wall electrodes have 45-degree angle with polarizer, (b) the POM image with a retardation plate, (c-d) after 90-degree rotation of the cell on the rotary stage of microscope.

3.3 Effect of the cell gap size and electrode materials on GO flakes order

I made cells with different gap distances (T), and I studied its effect on assembly of GO flakes. Figure 3-8a shows a POM image of 2 mg/mL GO suspension in a cell with T = 2 mm and having copper electrodes. The degree of brightness of the cell is lower than the 3 mm cell, but GO flakes still have their preferred ordination at the side and center of cell, respectively parallel and perpendicular to the cell wall, as the retardation plate reveals in Figure 3-8b. By further reducing the cell gap, the degree of cell brightness between crossed polarized decreases more, since the transmitted light is directly related to the distance that polarized light passes through a birefringent material, $I \propto I_0 \, sin^2(\pi d \Delta n / \lambda)$ where I_0 is the light intensity after the polarizer and d is the cell gap.

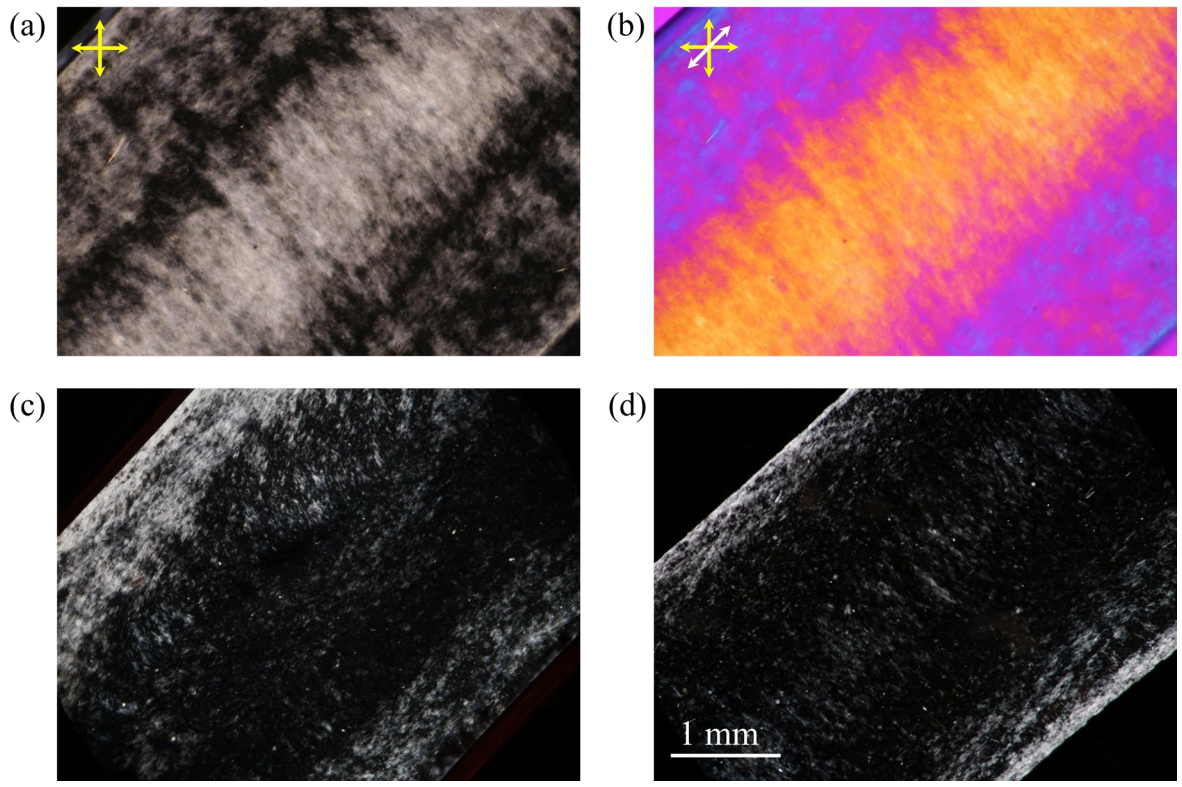

Figure 3-8. POM images of 2 mg/mL GO suspension in: (a) a cell with 2 mm gap distance, (b) with the retardation plate; (c) a cell with 600 µm gap distance, (d) a 600 µm cell with chrome electrodes.

A POM image of 2 mg/mL GO suspension in a cell with T = 600 µm with copper electrodes is shown in Figure 3-8c. The light transmission of the cell is significantly low and just areas close to the electrodes where GO flakes have a shear-induced alignment parallel to the side wall are bright and the center of cell looks dark. However, still a low degree of brightness can be observed at the center indicating the order of GO flakes at the center of the cell. To study the effect of the electrode materials on the order of GO flakes, I also made cells using aluminum and chrome foil and I observed that GO flakes show same behavior in the cells with different type of electrodes. A POM image of a 600 µm cell with chrome electrodes is displayed in Figure 3-8d. Here also only the shear-induced alignment of GO flakes at the cell sides are

visible. GO flakes regardless of their high aspect ratio that results in forming LC phases at a very low concentration, they are very low birefringence material. Hence, they can be observed between crossed polarizer only if an enough number of GO flakes are vertically oriented in the same direction. The 2 mg/mL GO suspension, contains very low amount of GO flakes and this is one of the reasons that the 600 µm cell looks dark between crossed polarizers.

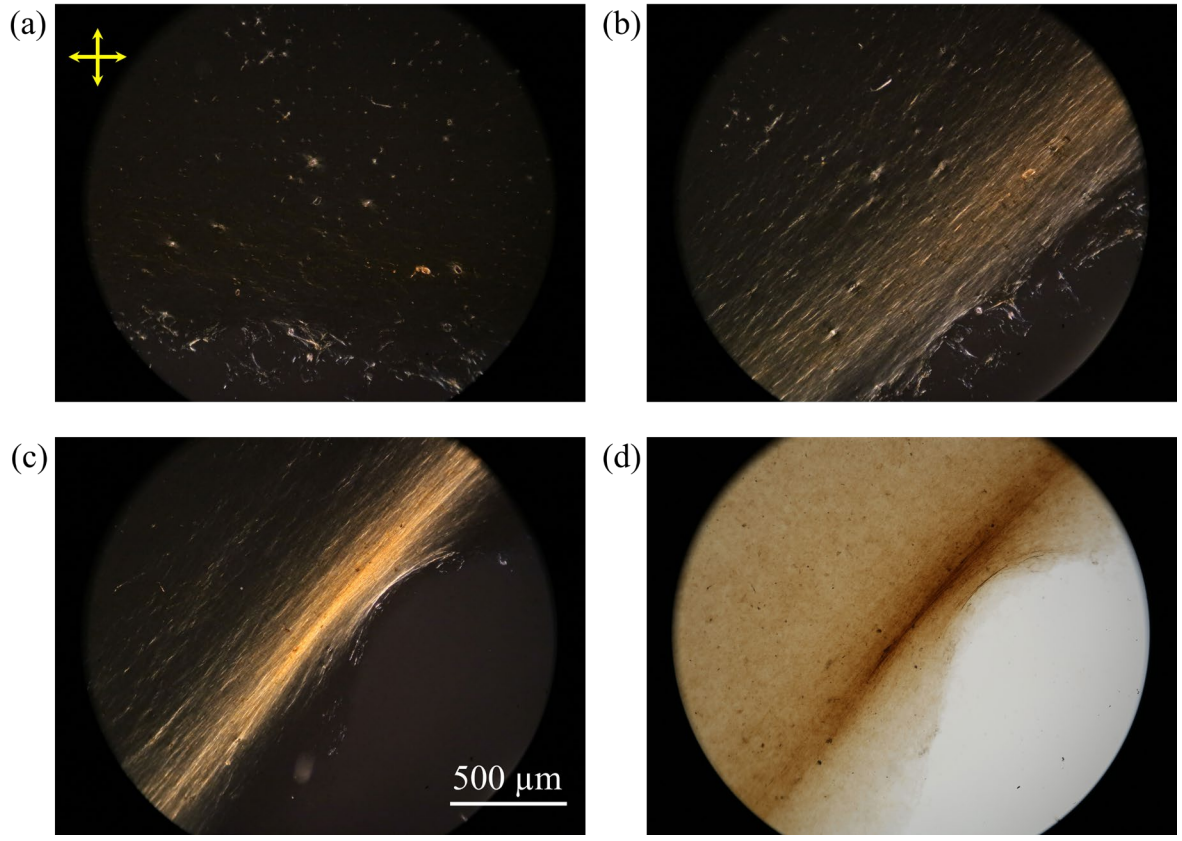

Figure 3-9. Images of a thin film of GO flakes in a 600 µm cell, filled with 2 mg/mL GO suspension and after that the cell got dried and its top glass substrate and electrodes are removed. Between crossed polarizers when the cell side (a) is parallel to the polarizer, (b) & (c) has a 45-degree angle with the polarizer. (d) without polarized light.

Figure 3-9a shows a POM image of GO flakes in a 600 µm cell after that the filled cell was dried and its top glass substrate and electrodes are removed. In the image, the cell is placed parallel to the polarizer and the GO flake film looks dark between crossed polarizers. By

rotating the cell 45-degree angle, Figure 3-9b, the area close to the cell side appears bright, since GO flakes have a shear-induced alignment parallel to the electrode that was removed. In Figure 3-9c, the dried film is gently wrinkled using a tweezer to bring the aligned GO flakes close to each other. However, even the wrinkled film still shows a low degree of brightness between crossed polarizers because of GO low birefringence. GO flakes are transparent and it is difficult to observe them by a microscope. In Figure 3-9 without polarized light, the darkness of the dried GO flakes film indicating that it consists of a high number of GO flakes.

3.4 Effect of the GO suspensions concentration on flakes order

To understand the effect of GO suspension concentration on the spontaneous orientational order of GO flakes in the confined space of a cell, I performed a transmitted light measurement at the center of 300 μm cells that were filled with different concentrations of GO suspensions. The suspensions had concentrations from pure LC phase to bi-phasic. For this aim, I placed the cells between crossed polarizers in the microscope with 10x objective, and I measured the transmitted light from the analyzer when I rotated the cells on the rotary stage of the microscope. To measure the light intensity, I used a THORLABS DET36A/M Si Biased detector mounted on the microscope, which was connected to a Tektronix TBS1064 oscilloscope to read the values.

I drew the measured transmitted lights for GO suspensions having 2 and 1 mg/mL concentration, in Figure 3-10. The graph is in a polar coordinate system, and the points in the graph show the measured intensity for different angles between the polarizer and the side wall (electrode) directions θ. The values are normalized to the maximum measured intensity for 2 mg/mL suspension. The lines are a sine-square fitting to the measured values because the

transmitted intensity is proportional to a sine-square of the angle between the polarizer and the GO flakes direction φ, $I \propto I_0 sin^2 2\varphi$.

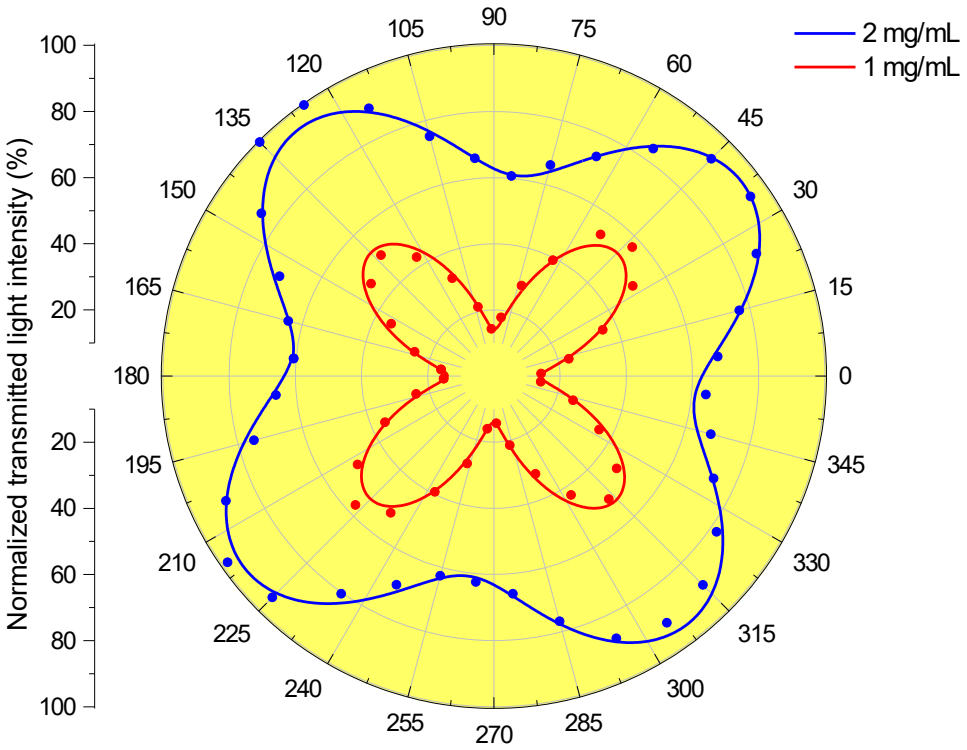

Figure 3-10. Normalized transmitted light at center of 300 μm cells filled with 2 and 1 mg/mL concentrations at different θ angles between crossed polarizers with their sine-square fitting lines

For both concentrations, the maximum transmitted lights are measured when the side wall has around 45-degree angle with the polarizer in agreement with our POM measurements, indicating that GO flakes have a preferred average orientation perpendicular to the side wall at the center of cells. For the 2 mg/mL suspension, because of higher concentration there is a relatively higher birefringence in comparison with 1 mg/mL. However, the measured light intensity for 2 mg/mL do not change significantly in different angles and the lowest intensity when the cell side is parallel to the polarizer, is equal to 60 percent of the maximum. This

behavior reveals the existence of domains of orientated GO flakes with the same assembly, but different orientations in the center of the cell. Nevertheless, a preferred orientation in a direction perpendicular to the side wall is still detectable. This preferred orientational direction at the center of cell is more noticeable for 1 mg/mL suspension when its lowest intensity is equal to 25 percent of its highest intensity at 45-degree angle. I performed the transmitted light measurements also for the critical concentration for having pure LC phase, 0.7 mg/mL, and 0.5 mg/mL concentration being biphasic, Figure 3-11. Both show almost the same light intensity but a lower one comparing to 2 mg/mL. For both of them at the center of cells, the preferred orientational order perpendicular to the side wall is pronounced.

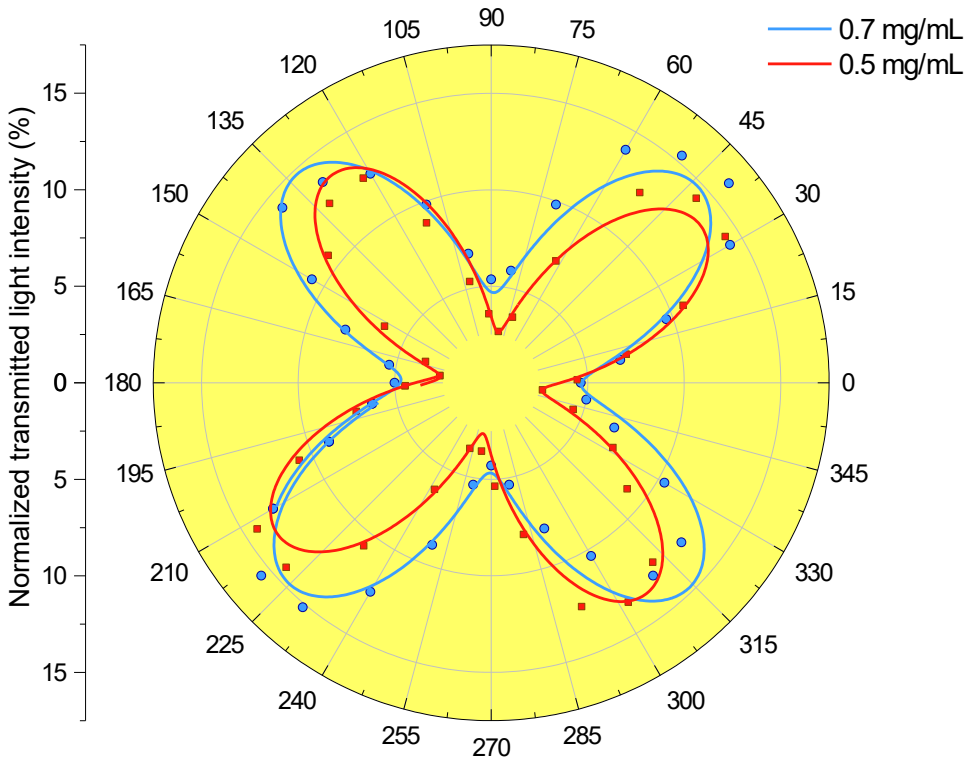

Figure 3-11. Normalized transmitted light at center of 300 µm cells filled with 0.7 and 0.5 mg/mL concentrations at different θ-degree angles between crossed polarizers, with their sine-square fitting lines.

All the concentrations have their four maximum transmitted lights when the side wall had 45-degree angle with the polarizer during the cell rotation between crossed polarizers. I calculated the average of the four maximum transmitted lights, and I compared them in Figure 3-12, with an error bar showing the variation of the maximum transmitted lights for each concentration. By decreasing the concentration, the light transmission decreases rapidly in LC part of the GO suspension phase diagram, but this rapid decreasing is not continued to the biphasic part of the phase diagram. The main reason is that the 0.5 mg/mL concentration is the equilibrium concentration for having LC phase for first days of GO suspension preparation as the GO LC suspension stability demonstrated. Hence 0.5 mg/mL concentration shows a level of birefringence similar to the critical concentration, 0.7 mg/mL.

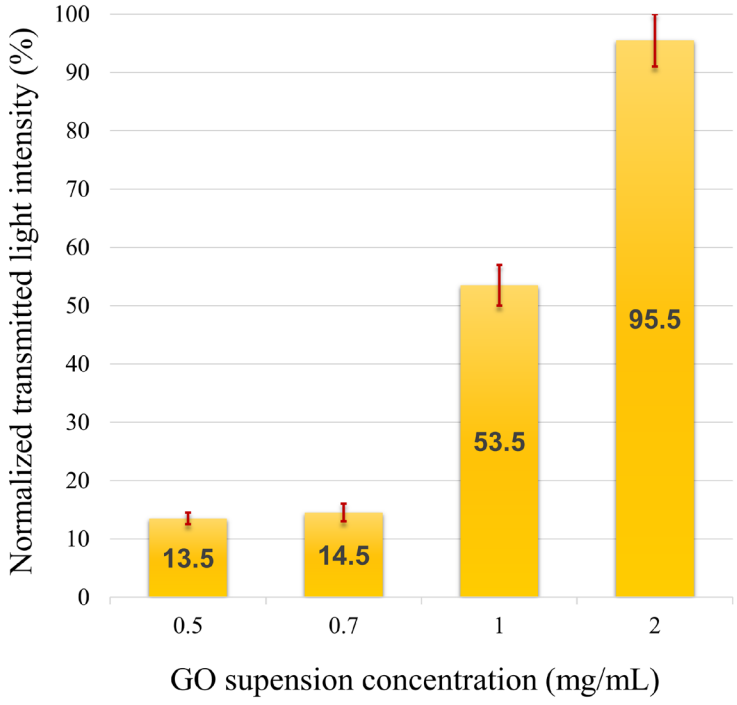

Figure 3-12. Average of the four maximum measured transmitted lights between crossed polarizers when the side wall had 45-degree angle with the polarizer, for different concentrations. The error bar showing the variation of the maximum transmitted lights for each concentration.

Figure 3-13 shows the POM images of GO suspensions with different concentrations at two different angle, $\theta = 0°$ and 45°; a visual summary of the concentration effect on GO flakes order. In the images, the reduction of the birefringence by decreasing the concentration is obvious. For 2 mg/mL, regions with different GO flakes orientation are visible and the GO suspension looks similar at both angles. However, for lower concentrations the noticeable difference between two angles proving the preferred orientational direction for GO flakes. 0.5 mg/mL, being biphasic, looks similar to 0.7 mg/mL, having pure LC phase, as 0.5 mg/mL is the equilibrium concentration for having LC phase at first day. For lower biphasic concentration, 0.2 mg/mL, a preferred direction for GO flakes at the center of 300 μm is still detectable.

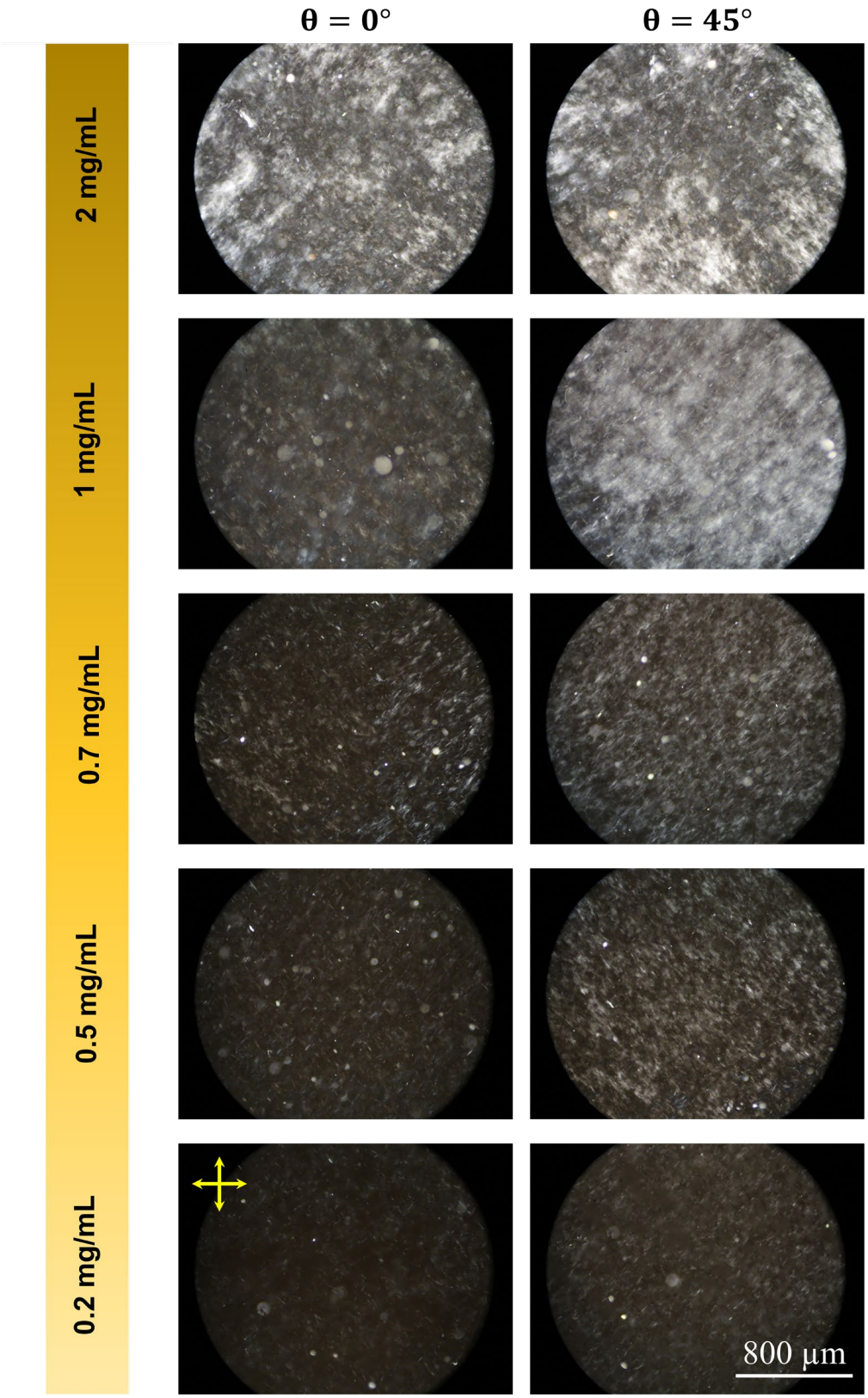

Figure 3-13. POM images of GO suspensions with different concentrations at the center of 300 µm cells at two different angles, when the side walls are parallel to the polarizer θ = 0° and it has 45-degree angle, θ = 45°.

Chapter 4: Electro-optical switching of GO flakes

4.1 GO LC electro-optical switching

Showing pure liquid crystal phase at very low concentrations, make large GO flakes very attracting for electro-optical switching applications. I could successfully perform the GO flakes electro-optical switching using electric cells having Cu, Al and Cr as electrode materials and cell gap of 300 to 600 µm.

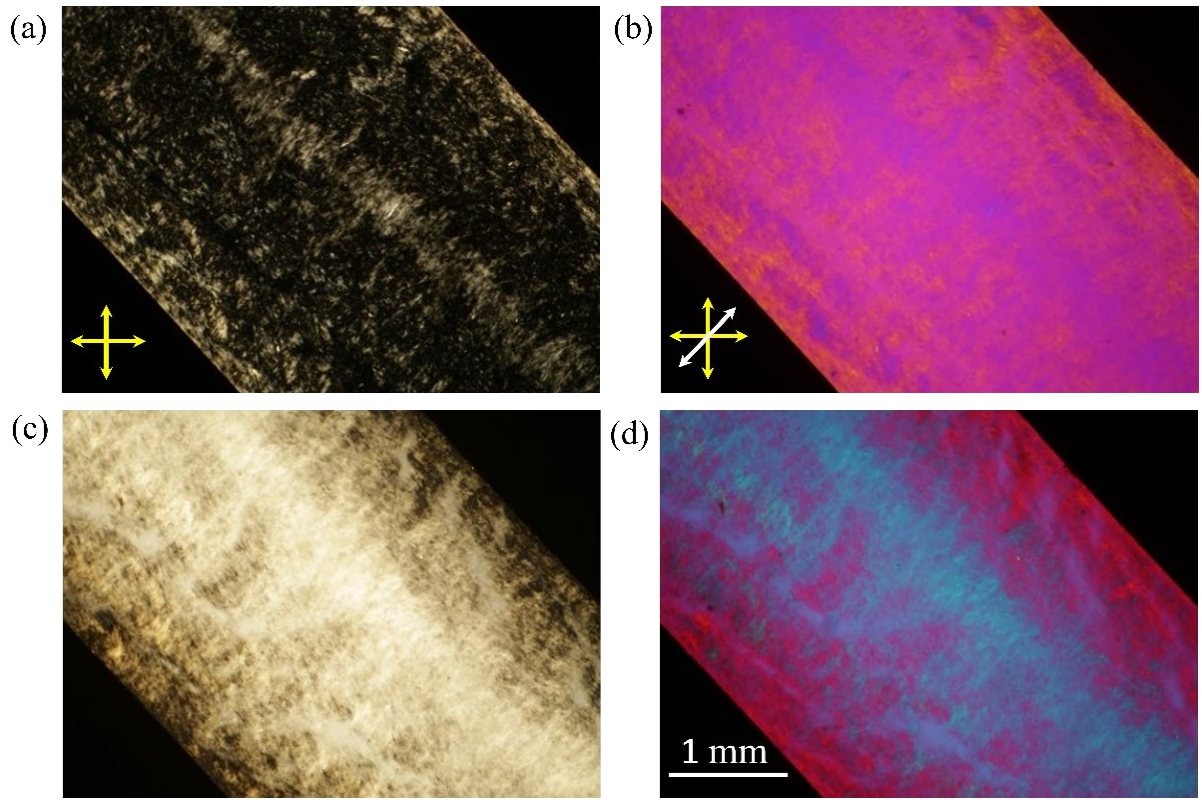

Figure 4-1. POM images of 2 mg/mL GO suspension in a 300 µm cell, (a) before applying electric field, (b) using a retardation plate and (c) under 7.5 V/mm electric field, (h) with a retardation plate. The white arrow indicates the slow axis of retardation plate.

Figure 4-1a shows a POM image of a cells with 300 µm gap distance and filled with 2 mg/mL GO suspension. In the POM image, GO suspension looks different and dark in comparison with 3 mm cell as the direct result of lower amount of GO flakes that polarized light pass through in the confined space of the 300 µm cell. However, there are still two bright areas at the center and side of cell and using the retardation plate, Figure 4-1b, having different orientations and perpendicular to each other. This means that flow-induced alignment is effective even in a confined space, where GO flakes flow slowly in the cell.

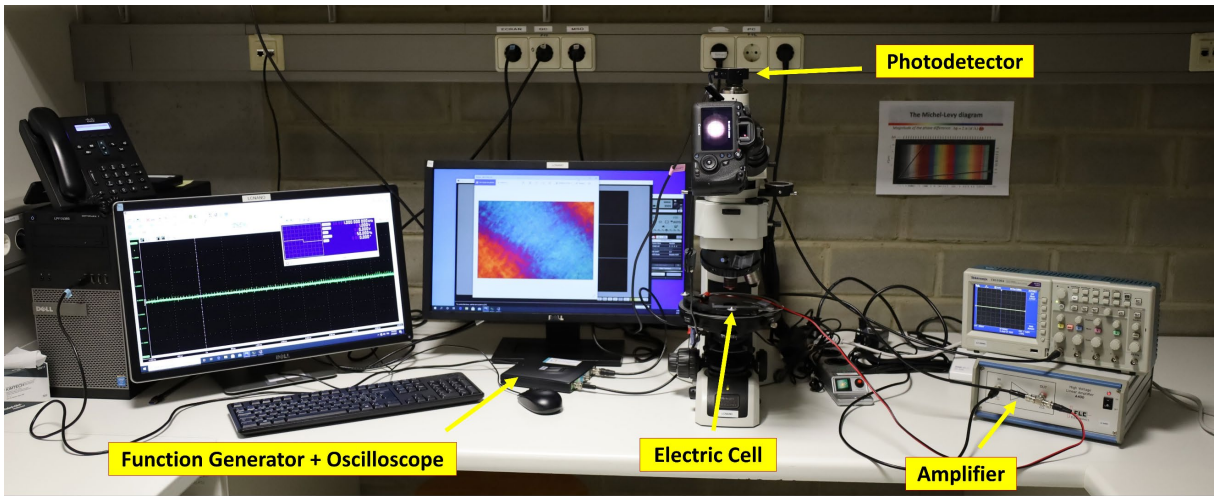

Figure 4-2. The electric setup was used for performing electro-optical switching of GO flakes, consists of a function generator (+ oscilloscope), an amplifier and a photodetector hat is independently connected to an oscilloscope.

For the electro-optical switching of GO flakes, I used an electric setup showing in Figure 4-2, to control and apply the electric field. The setup consists of a function generator producing square electrical waveforms, TiePie Handyscope HS5, and an amplifier, Single Channel High Voltage Linear Amplifier A400 FLC Electronics. The TiePie Handyscope HS5 was also an oscilloscope, and it was controlled by a computer. Using the setup, I generated variable electric field of about 5-12.5 V/mm in the KHz frequency range in the electric cells, which were placed

between crossed polarizers in the microscope. For the optical measurements, the microscope was equipped also with a photodetector that was independently connected to an oscilloscope.

The first successful electro-optical switching of GO flakes was reported in their bi-phase, and the switching of GO flakes was not passible in their LC phase. This problem was a direct consequence of small size of GO flakes that were used and had a mean size of < 5 μm. Because of small size of GO flakes a high concentration of GO flakes was required for having pure nematic phase, 1.1 Vol% (22 mg/mL) [19]. This results in a dramatic increase of the inter-flakes interaction making GO flakes switching impossible. However, the large GO flakes that I studied have an average size of 38 μm and they form pure nematic LC phase at a very low concentration; this allows the electro-optical switching of GO LC, under low electric fields.

Figure 4-1c shows the GO flakes in 2 mg/mL suspension when they are switched under an interestingly low 7.5 V/mm electric field, using a high frequency (10 KHz) AC current. In the POM image, under the electric field, there are two areas in the cell. A very birefringence at center where GO flakes are switched and have an orientation parallel to electric field and they appear bluish using a retardation plate, Figure 4-1d. In addition, there are narrow yellowish areas parallel to the electrodes (side walls) where GO flakes are not switched and have orientation perpendicular to electric field. The yellowish areas are because close to the electrodes, the GO flakes form a concentric layer driven by shear flow and homeotropic anchoring on the surface of the electrodes [120]. Hence In these areas GO flakes cannot switch under electric field and they keep their initial shear-induced alignment.

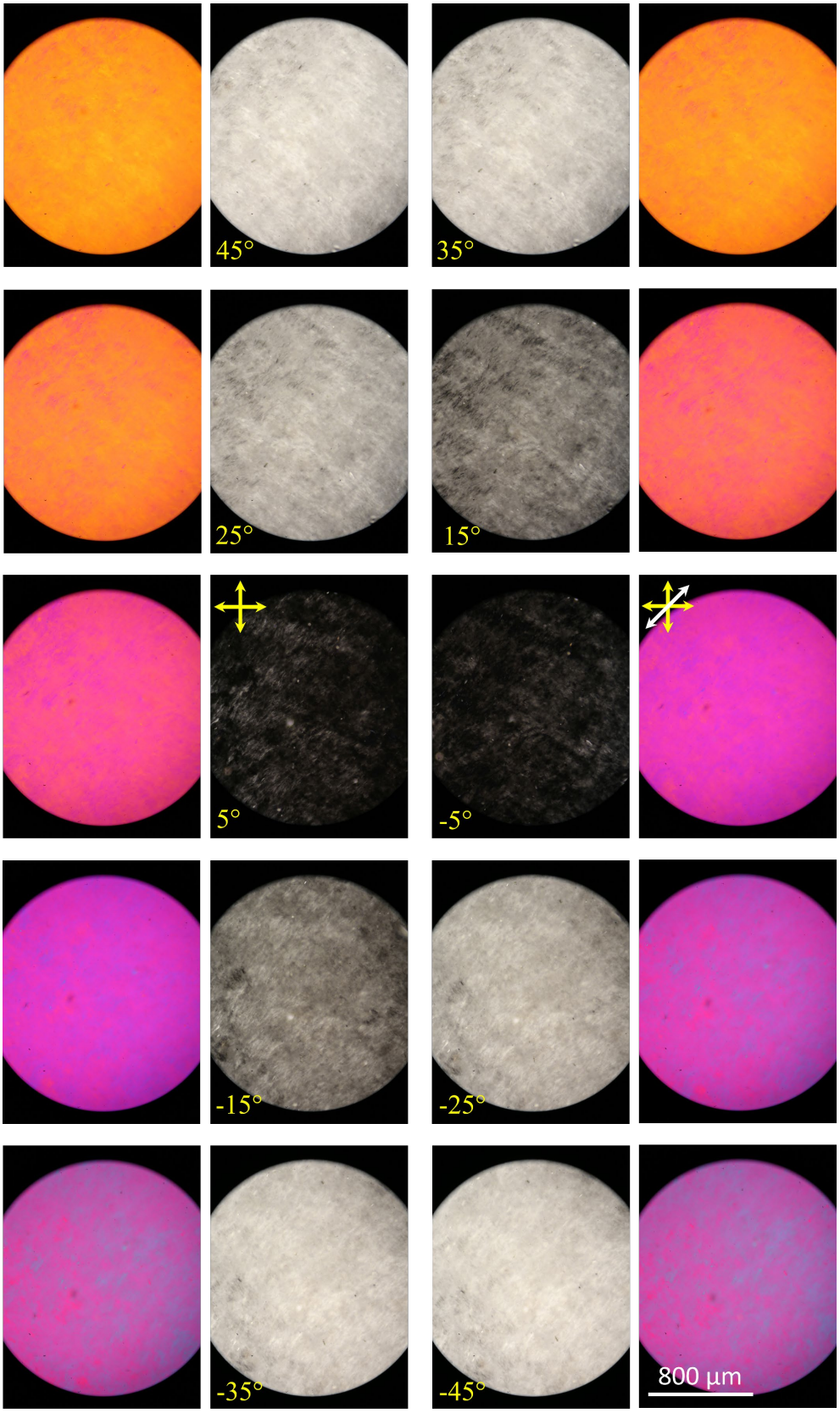

Figure 4-3. POM images of the 300 µm cell filled with 2 mg/mL GO suspension under 10 V/mm electric field when rotated between crossed polarizers, also using the retardation plate

Large GO flakes show a great response to a high frequency electric field in their LC phase to get aligned parallel to electric field direction. Figure 4-3 show POM images of aligned GO flakes at the center of a 300 μm cell under 10 V/mm electric field, also with the retardation plate, when the cell was rotated between crossed polarizers. The indicated angle in the images is the angle between the electrodes (side walls) and the polarizers. I observed the maximum light transmission when the electrodes had 45- degree angle with polarizers i.e., when the angle between electric field direction and the polarizers was 45 degrees. This indicate that GO flakes are well aligned in the electric field direction.

Using the photodetector, I measured the transmitted light intensity for all the angles, and I drew in Figure 4-4. The points in the graph show the measured intensities that are normalized to the maximum measured intensity. The lines are a sine-square fitting to the measured values as the transmitted intensity is proportional to a sine-square of the angle between the polarizer and the GO flakes direction φ, $I \propto I_0 sin^2 2\varphi$. The significant difference between transmitted light at 0 and 45- degree angle, validates the great alignment of GO flakes parallel to the electric field direction. Although under electric field and without electric field, the maximum measured intensity is at 45-degree angle, without electric field it is just about 3 percent of when the electric field is applied to GO flakes, due to their field-induced alignment. Besides, under electric field because of GO flakes great alignment, the lowest measured intensity at 0-degree angle is lower than without electric field when GO flakes form aligned domains with different orientations.

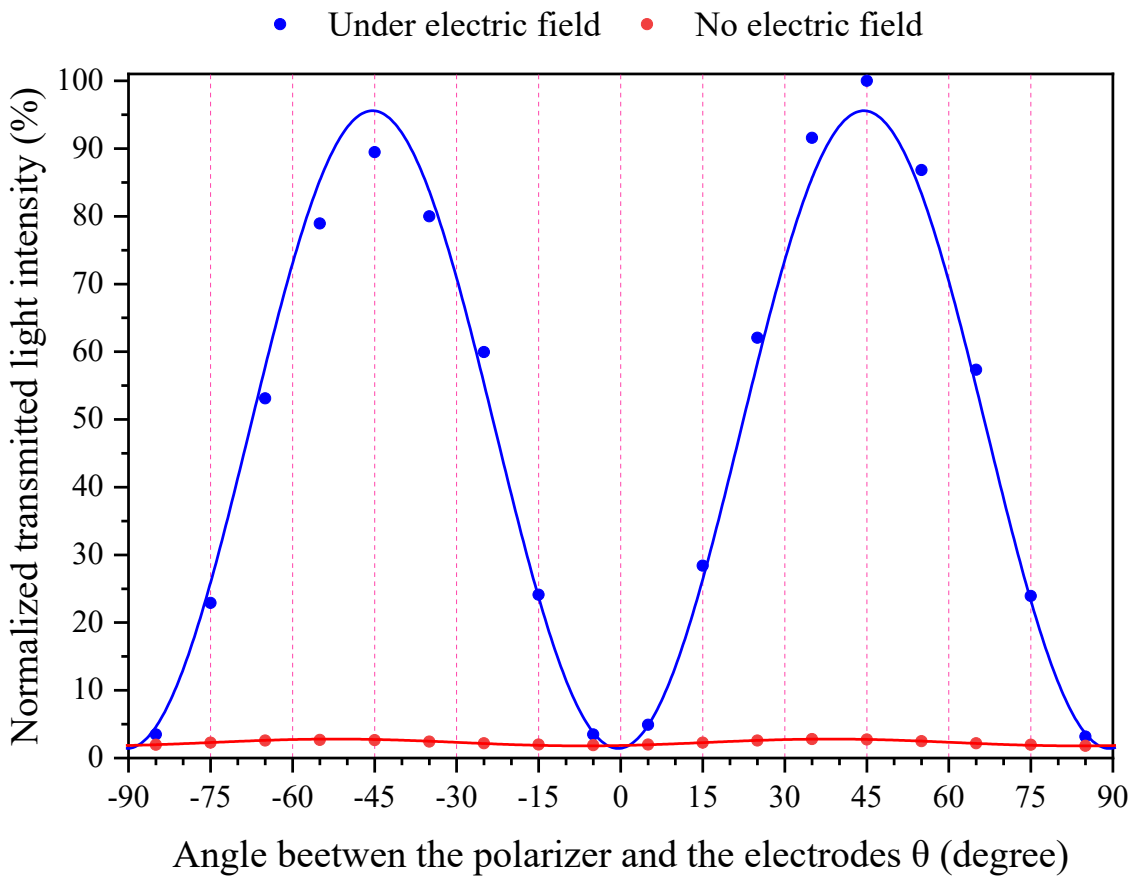

Figure 4-4. Normalized transmitted light at the center of 300 µm cells filled with 2 mg/mL GO suspension, under electric field and without electric field, at different θ angles between crossed polarizers with their sine-square fitting lines

4.2 Effect of voltage and frequency on GO flakes switching

To control the shear-induced alignment of GO flakes and to reduce the concentric layer at the side of the cell, I gently filled a 300 µm cell with 2 mg/mL GO suspension, Figure 4-5a. When the side walls have 45- degree angle with the polarizer, the cell is homogeneously dark between crossed polarizers and there is not bright area parallel to the electrodes.

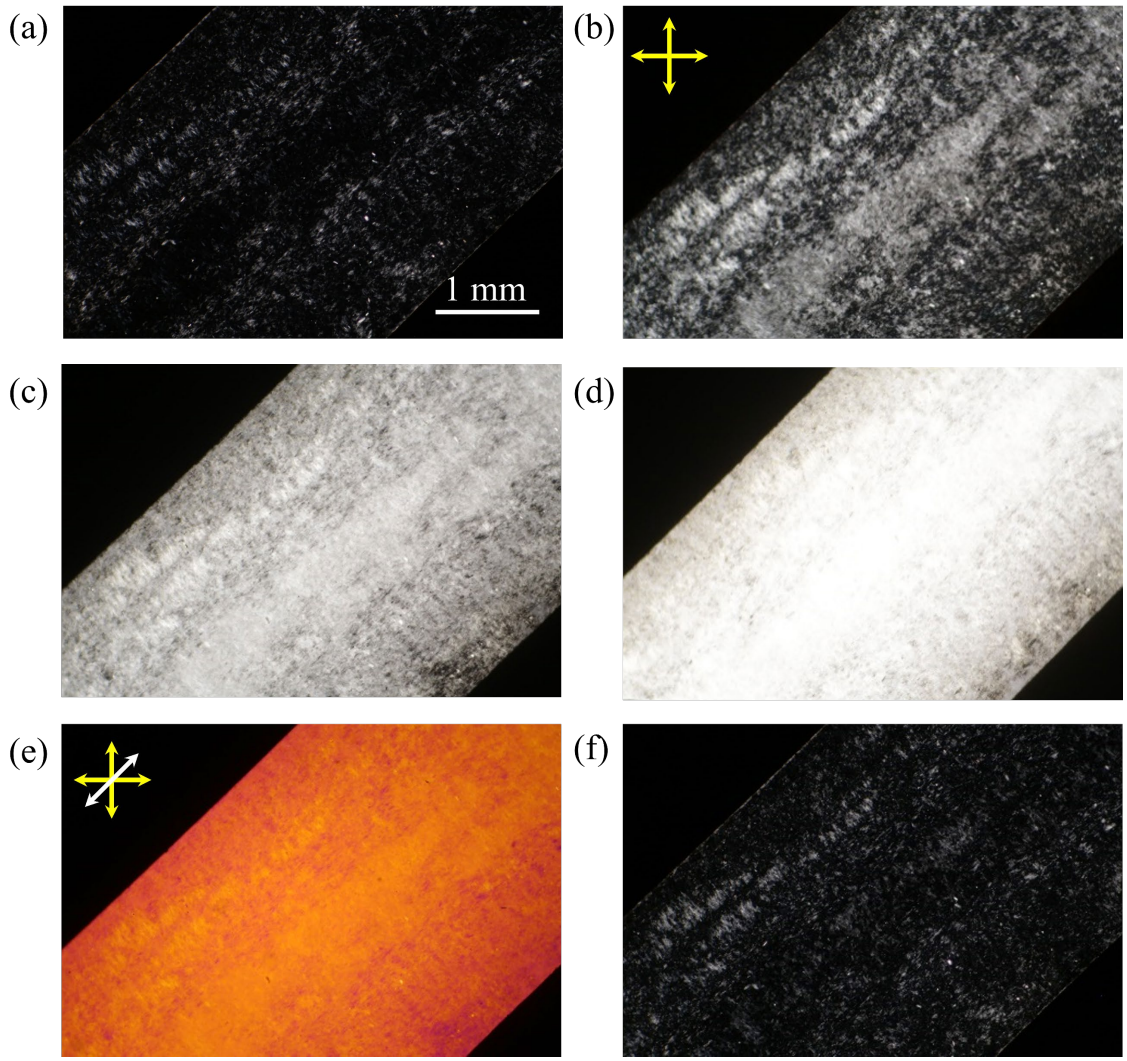

Figure 4-5. POM image of GO flakes in 300 µm cell with 2 mg/mL GO suspension, (a) before applying electric field. Under electric field (b) 5 V/mm, (c) 7.5 V/mm, (d) 10 V/mm. f) Under 7.5 V/mm electric field using the retardation plate. e) After switching off the electric field.

Using high frequency AC field, large GO flakes are sensitive even to very low electric field of 5 V/mm, Figure 4-5b. The higher electric field of 7.5 V/mm lets the GO flakes field-induced alignment to extend over the entire cell, Figure 4-5c, even nearby the electrodes. Figure 4-5e, using the retardation plate, shows how successfully the shear-induced and field-induced alignment of GO flakes can be controlled. Increasing the electric field to 10 V/mm results in a

strong light transmission, Figure 4-5d, since higher number of GO flakes switch to have a perfect orientation toward the electric field at the center of the cell.

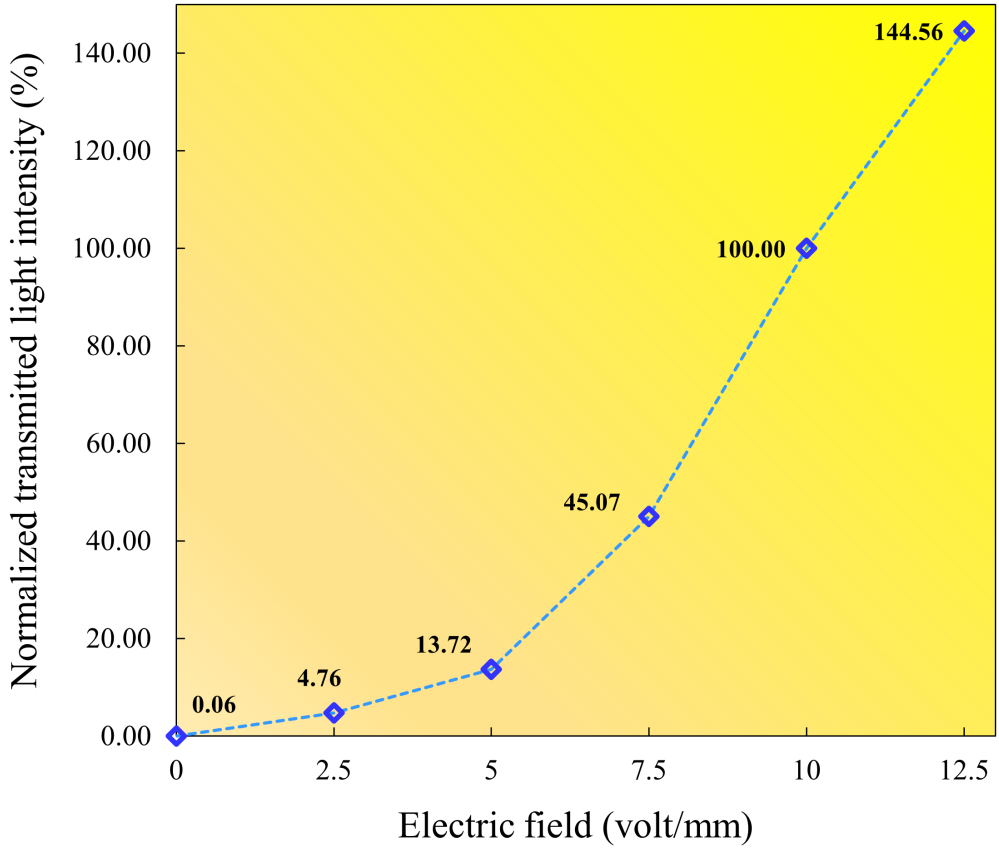

Figure 4-6. Normalized transmitted light at the center of 300 µm cells filled with 2 mg/mL GO suspension, under various electric fields while the electrodes have 45- degree angle with the polarizer.

Measured transmitted light intensities using the photodetector are drew in Figure 4-6 and all the values are normalized with the measured amount for 10 V/mm electric field. In the graph, by increasing the electric field, the light intensity does not increase linearly, and the increasing rate rise for equal steps between 0 to 2 V/mm and after 2 V/mm, the rate decreases. By increasing the electric field more than 2 V/mm, at the beginning the GO flakes that are well aligned parallel to electric field extend in the whole cells area. However, after a few seconds,

applying high electric fields results in appearance of H_2 bubbles in cells beside the electrodes, Figure 4-7a. The formation of H_2 bubbles is due to electrolysis of water occurring when a high voltage is applied to the electrodes [19]. By the H_2 bubbles formation, the electro-optical switching of GO flakes declines and eventually no switching can be observed, Figure 4-7b. When H_2 bubbles expand in GO suspensions, they force GO flakes to get close each other, hence the area around the H_2 bubbles look bright between crossed polarizers. In Figure 4-7c, the retardation plate reveals that GO flakes form a concentric layer around the bubbles and they have an orientation parallel to the bubbles surface.

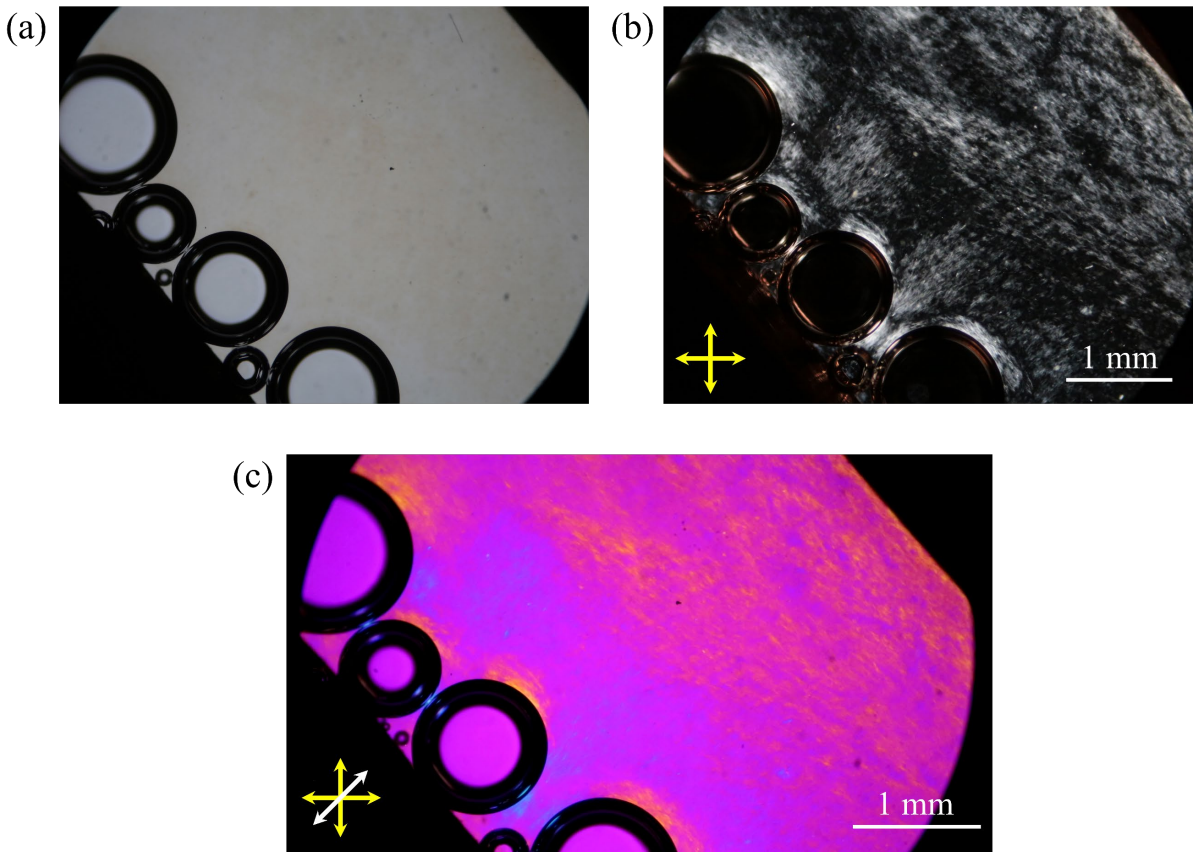

Figure 4-7. Images of the H_2 bubbles due to electrolysis of water in a 300 µm cell filled with 2 mg/mL GO suspension, (a) not polarized light, (b) between crossed polarizers, (c) with the retardation plate

For 2 V/mm or lower electric fields, there is no formation of H_2 bubble, hence this the range of electric field that I used for electro-optical switching of GO flakes. By switching off the electric fields, GO flakes switch back to have their initial orientational order before applying electric field, Figure 4-5e, and the spontaneous diffusive particle motion is involved in the restoring process. This behavior means that the electro-optical switching of GO flakes is a reversable process since GO flakes have their state with a lower free energy when they are not switched in the confined space of 300 µm cell and form oriented domains with different directions. To compare GO flakes orientation before applying an electric field and after switching off the field, Figure 4-8 shows the measured transmitted light intensity at the center of the cell. In both cases, GO flakes show a preferred average orientational order perpendicular to the electrode directions. However, it is not strong since the difference between the maximum and minimum light intensity is at a low level, below 35 percent.

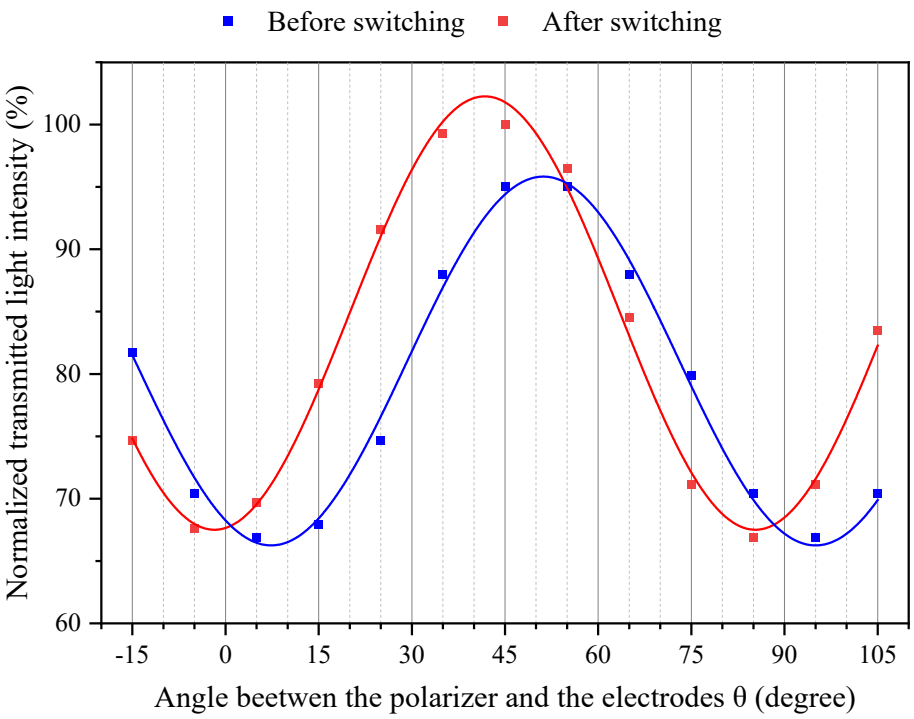

Figure 4-8. Normalized transmitted light at the center of 300 µm cells filled with 2 mg/mL GO suspension, before and after electro-optical switching using 10 V/mm electric field, at different θ angles, between crossed polarizers, with their sine-square fitting lines

I also studied the effect of AC current frequency on GO flakes electro-optical switching, Figure 4-9. In the graph the points show the measured intensities that are normalized to the maximum measured intensity for 10 KHz. By increasing the frequency from 1 KHz to 10 KHz, the light intensity increases significantly about 40 percent. However, increasing frequency from 10 KHz to 100 KHz does not have an effect on the transmitted light intensity. On the other hand, for all the frequency the maximum transmitted light measured when the electrodes have 45-degree angle with polarizers i.e., frequency don't have any effect on the orientation direction of switched GO flakes. For these reasons, I generally used 10 KHz frequency for performing electro-optical switching of large GO flakes.

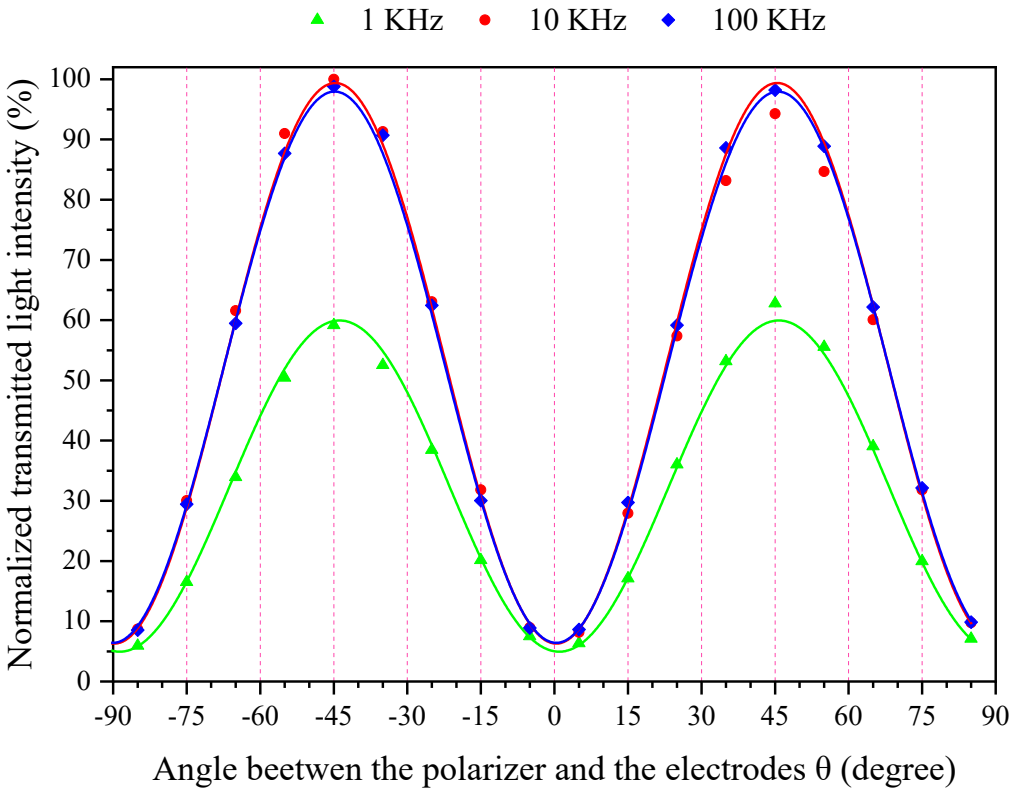

Figure 4-9. Normalized transmitted light at the center of 300 µm cells filled with 2 mg/mL GO suspension, under 10 V/mm electric field using AC currents with different frequencies, at different angles, between crossed polarizers, with their sine-square fitting lines

4.3 Effect of GO suspension concentration on the flakes electro-optical switching

The ability of performing the electro-optical switching of large GO flakes in their LC phase, make it possible to compare their switching in different GO suspension concentrations, from biphasic to LC phase. I studied the GO flakes field-induced reorientation by measuring the transmitted light at the center of cells with different concentrations, using POM and the photodetector, under 10 V/mm electric field with 10 KHz frequency. For GO LC phases because of their initial spontaneous orientational order and more important their higher concentrations, I measured a high transmitted light intensity, Figure 4-10. It is in opposite of what was reported that GO flake electro-optical switching is not possible in their LC phase [19]. For 1 mg/mL suspension having also pure LC phase, I measured the maximum transmitted light just 28 percent of 2 mg/mL suspension.

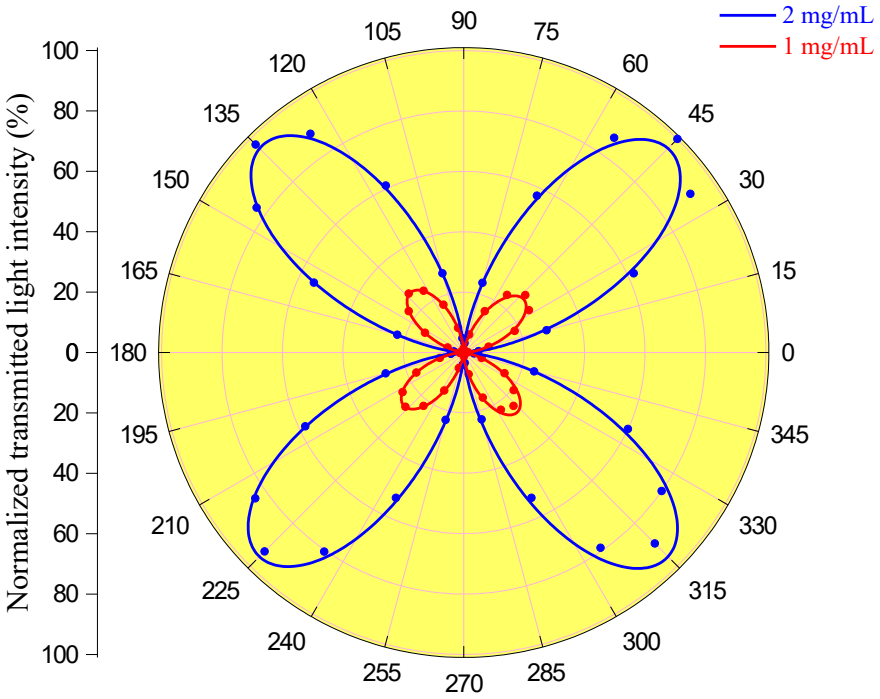

Figure 4-10. Normalized transmitted light at center of 300 µm cells filled with 2 and 1 mg/mL suspensions, under 10 V/mm electric field, at different angles of the analyzer and electric-field direction; the points are the measured values, and the lines are their sine square fitting.

For the critical concentration for having pure LC phase, 0.7 mg/mL, and bi-phasic suspension, 0.5 mg/mL, the transmitted light intensity drops rapidly to 6 and 4 percent, respectively, Figure 4-11. The graphs obviously show that concentration has a remarkable effect on the field-induced birefringence. My results clearly prove the great advantage of electro-optical switching of GO flakes in their pure LC phase. The high sensitivity of large GO flakes to electric field, because of their high polarizability, can overcome their inter-flakes interaction that is against flakes switching [90].

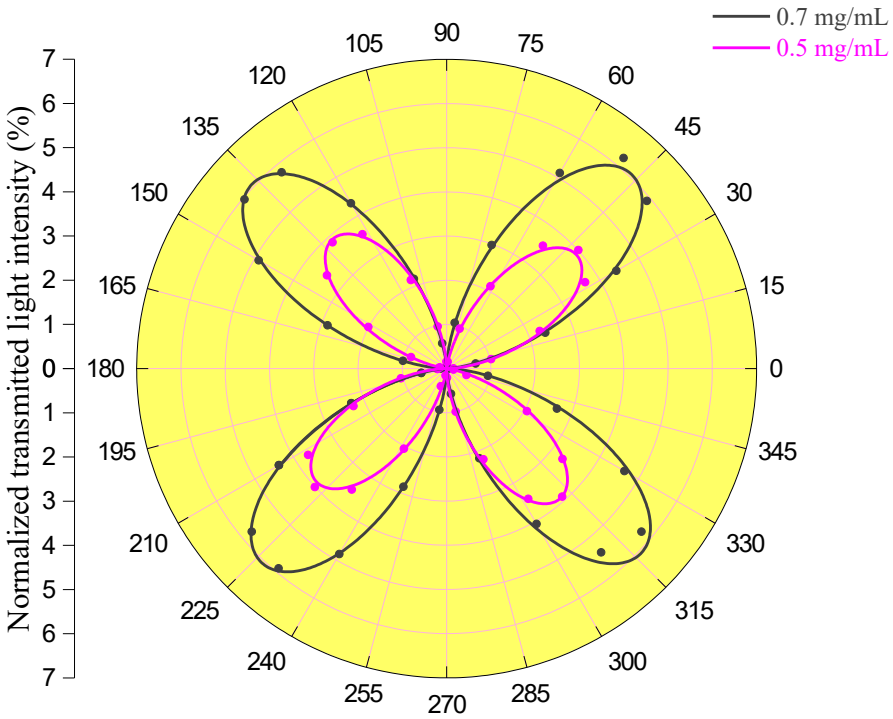

Figure 4-11. Normalized transmitted light at center of 300 µm cells filled with 0.7 and 0.5 mg/mL suspensions, under 10 V/mm electric field, at different angles between the analyzer and electric-field direction; the points are the measured values, and the lines are their sine square fitting.

Regardless of concentration, large GO flakes always show a great response toward electric field direction. In Figure 4-12, I compared the average orientation of GO flakes to the electric field direction by calculating an average for the angles between the four measured maximum

light intensities and electric field direction (perpendicular to the electrodes direction), for each concentration. The graph shows that GO flakes are well oriented at center of cells in the electric field direction, especially in GO suspension with 2 mg/mL concentration.

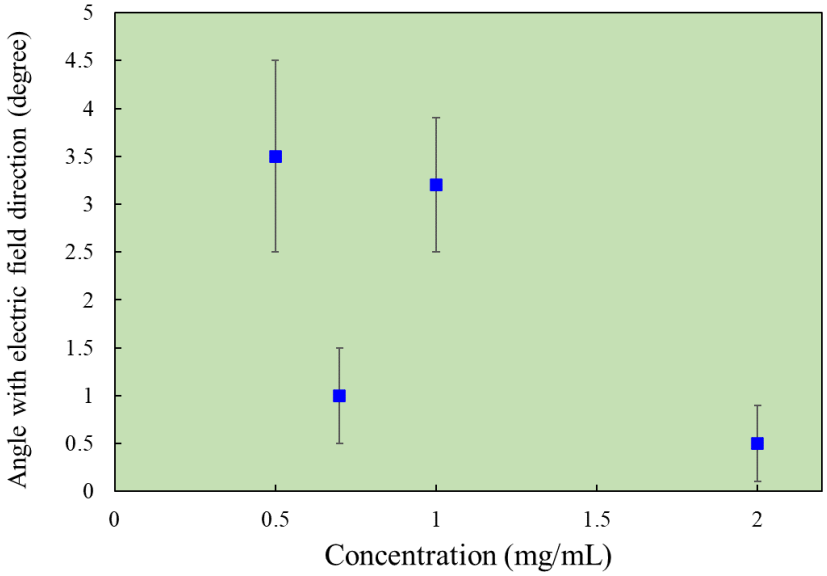

Figure 4-12. Angle between the measured maximum transmitted light intensities and the electric field direction

I plotted the normalized light intensity for different concentration in Figure 4-13, without and under the electric field, to compare them for GO flakes electro-optical switching. By increasing GO suspension concentration, the transmitted light intensity increases rapidly in both conditions, without electric field and under electric field, but it stronger under electric field. For all the concentration, there is a crucial difference between two conditions, indicating the great response of large GO flakes to the electric field. In Figure 4-14, the sharp contrast between two angles confirming the great field-induce alignment of GO flakes toward the electric field direction. The linear graph in Figure 4-13 demonstrations that under the electric field, how many times the transmitted light intensity increased which is also rises by increasing the concentration. For 2 mg/mL concentration it is about 34 time, proving the great advantage of pure GO LC over biphasic GO suspensions for electro-optical applications.

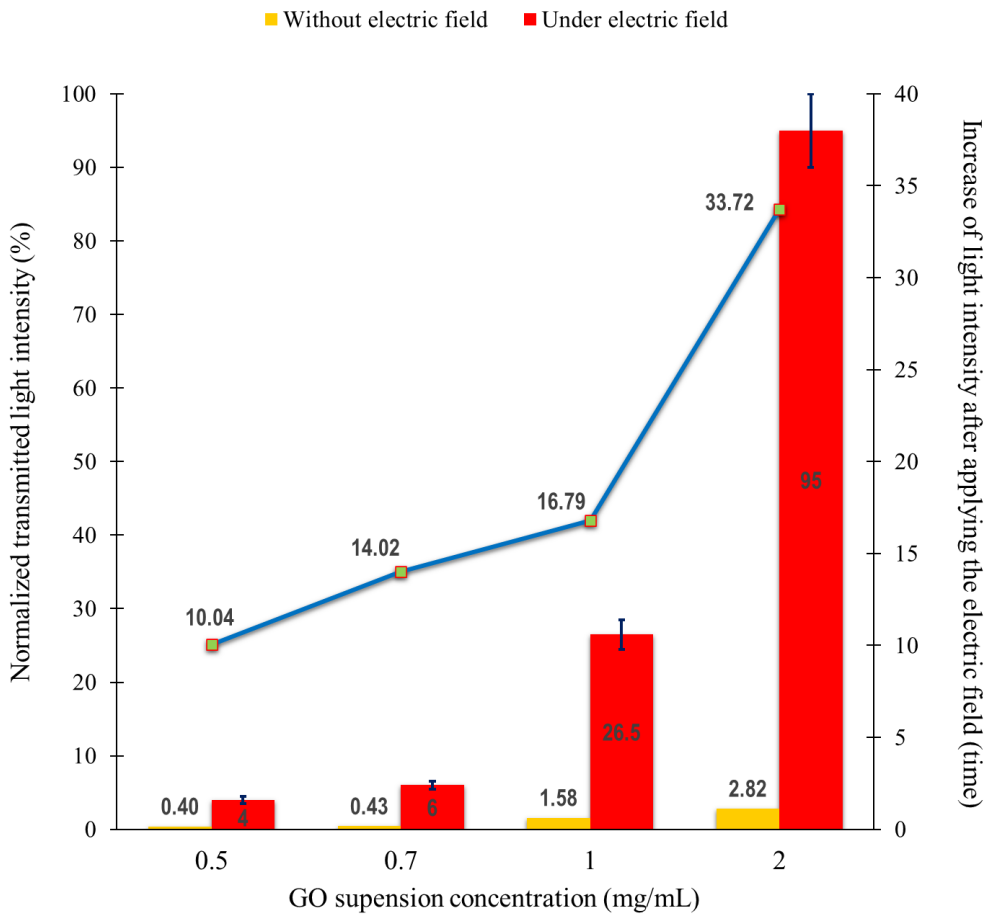

Figure 4-13. Average of the four maximum measured transmitted lights between crossed polarizers when the side wall had 45- degree angle with the polarizer, for different concentrations, without and under the electric field. The error bar showing the variation of the maximum transmitted lights for each concentration. In addition, the green points show how many times the light intensity increased after applying the electric field.

Figure 4-14 shows the POM images of GO suspensions with different concentrations under 10 V/mm with 10 KHz frequency, at two different angle, $\theta = 45°$ and 5°, also with the retardation plate; a visual summary of the concentration effect on electro-optical switching of GO flakes. Since there were a significant difference between transmitted light intensities for different concentrations, I used the camera in different light sensitivity modes for different concentrations to be able to take picture of maximum and minimum light intensities. Hence, just pictures for each concentration are comparable, but not for different concentrations.

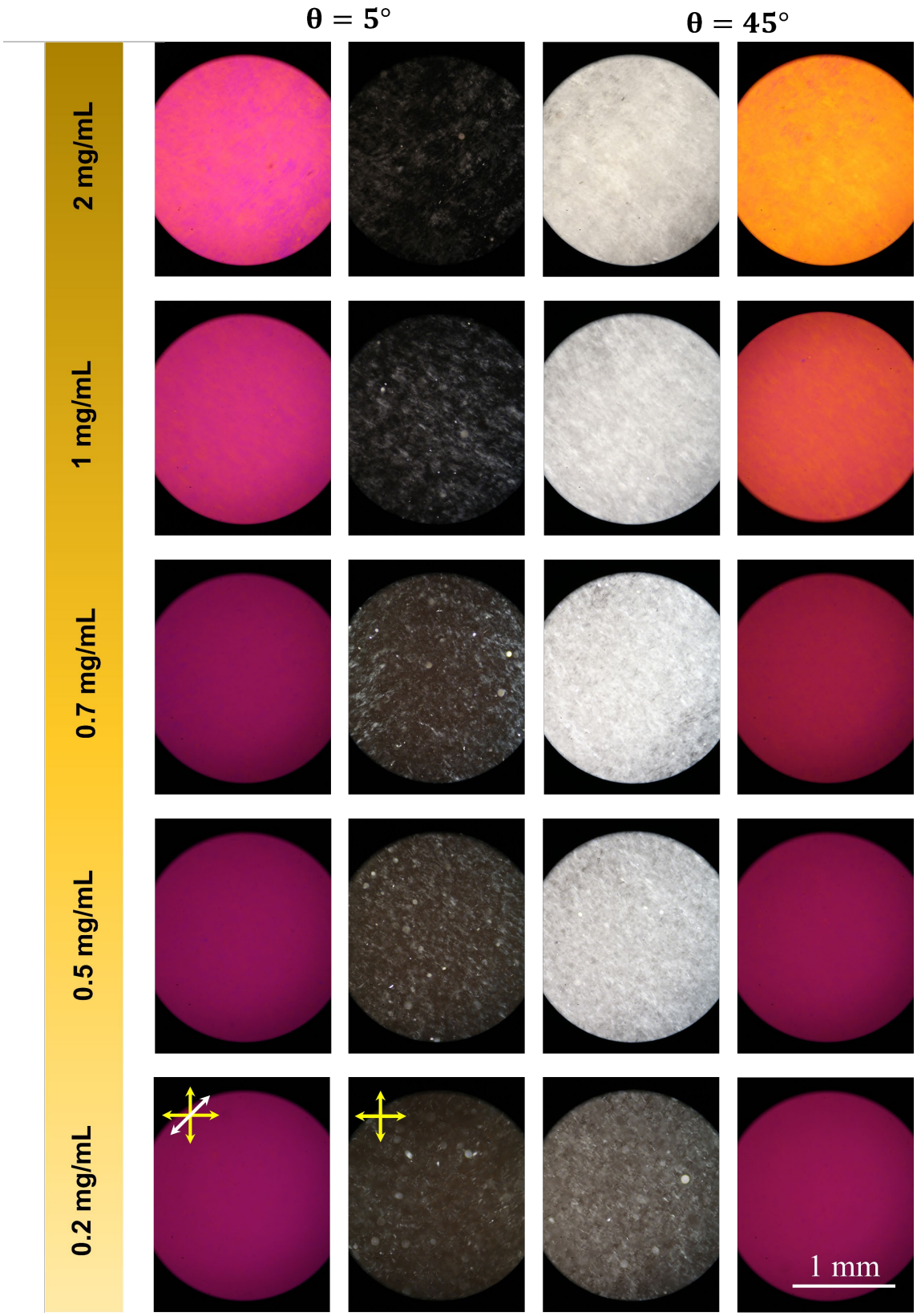

Figure 4-14. POM images of GO suspensions with different concentrations at the center of 300 µm cells under 10 V/mm electric field, at two different angles, θ = 5° and θ = 45°, also using the retardation plate.

Chapter 5: GO flakes assembly

5.1 Resolving the GO flakes orientational order by synchrotron SAXS

POM could reveal the different orientation and direction of GO flakes in the confined space of cells. However, what I could define by POM is their averaged orientational order. For a precise examination of GO flakes orientational order in the confinement space of cells, I decided to perform Small-Angle X-ray Scattering (SAXS) measurements on my cells. For this aim, I applied for a beamline time at ALBA and ESRF synchrotrons as the main proposer of the projects.

5.1.1 Small-Angle X-ray Scattering

X-ray scattering methods are perfectly efficient for the structural inspection of soft matter and nanomaterials systems both in bulk and at the interfaces [122]. SAXS can give resolution of the order of 1–100 nm for structural examinations in the bulk, allowing to determine the structure at atomic and molecular scales in systems without perfect crystalline order [123]. Developments in equipment have made possible that SAXS reach length scales up to micrometer and beyond by ultra-small-angle X-ray scattering (USAXS) method.

A remarkably powerful source of X-rays is a synchrotron. In a synchrotron, as high energy electrons circulate around the synchrotron, the X-rays are produced. The whole world of synchrotron science is based on one physical concept: a moving electron emits energy when it

changes direction. If the moving electron is fast enough, the emitted energy is at X-ray wavelength. At a synchrotron, the electrons are accelerated to very high energy and then they are made to change their direction periodically. As a result, lots of thin X-rays beams are emitted, each one guided to a beamline close to the accelerator, Figure 5-1.

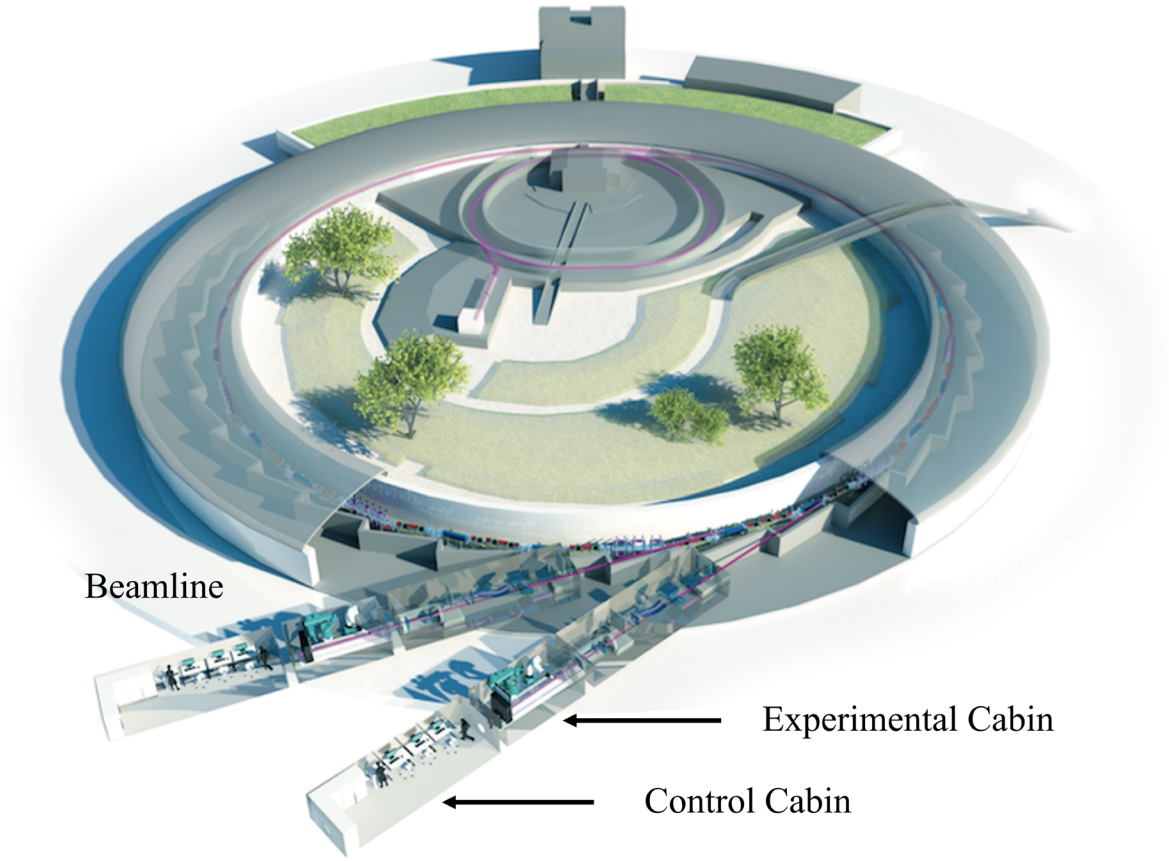

Figure 5-1. Schematic of a synchrotron showing beamline and its different sections [124]

The modern synchrotrons offer high brilliance to study very dilute systems, and investigate time-dependent processes in real-time by X-ray scattering methods. The high brilliance is the main strength of the synchrotron radiation that means high flux, low divergence, and small beam size. This results in high angular, spatial, and temporal resolutions in the examination of microstructure and dynamics, especially when it combine with advanced detectors [125], [126].

The key formalism of small angle scattering method is alike for light, neutrons, and X-rays. However, there is a difference and it is the interaction between the incident radiation and the scattering medium. Figure 5-2 shows a representation of the scattering geometry for a standard SAXS experiment setup. An extremely collimated and monochromatic X-ray beam having λ wavelength, traverse a sample and the scattered beam is recorded by a 2D detector in the forward direction. A beamstop before the detector blocks the transmitted X-ray beam and the detector counts the number of scattered photons as a function of the scattering angle, θ. To prevent absorption and scattering by air, the flight paths of the scattered beam are in vacuum. Scattering at small angles is completely elastic, therefore the incident and scattered wave vectors (k_i and k_s,) are equal to $2\pi/\lambda$ [123], [127].

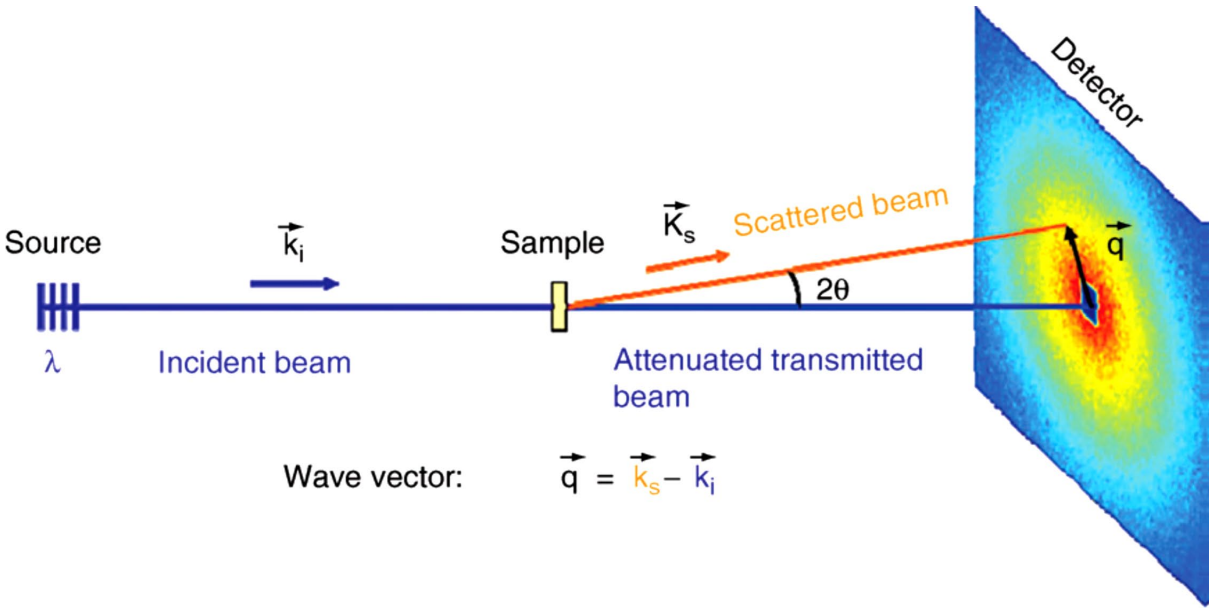

Figure 5-2. Schematic of a SAXS experiment set-up representing the incident, scattered, and transmitted beams; the 2D detector; and the beamstop.

$q = k_s - k_i$ is the scattering vector and its magnitude is determined by

$$q = \frac{4\pi}{\lambda} \sin\theta$$

This amount is the normal length scales measured by the scattering experiment and by using Bragg's law:

$$2d \sin\theta = n\lambda;\ \ n = 1,2,3, \ldots.$$

The scattering vector is determined by

$$q = \frac{2\pi}{d}$$

Therefore, the smallest scale size measured by a scattering experiment is calculated by the range of 2π/q. In synchrotron SAXS, the covered q-range can typically be 0.006 nm^{-1} < q < 6 nm^{-1} using 1 Å X-ray wavelength, equivalent to real-space dimensions of 1 μm to 1 nm.

The number of scattered photons into unit of the detector is the value that can be compared in different SAXS measurements. It is normalized by the incident flux (photons per second per unit area) and the thickness of sample, which is so-called the differential scattering cross section per unit volume (dS/dW) [123]. It is in units of reciprocal length per solid angle and in practice it is represented by I(q). For a specified λ, different size scales can be measured depending on the sample-detector distance (i.e., θ). Normally, using SAXS can measure sizes from about 1 nm to above 100 nm, and by USAXS can probes sizes larger than 100 nm up to several microns [127].

X-ray diffraction patterns recorded on oriented samples like LC phases are helpful to determine their structural parameters. In Figure 5-3, the common nematic and smectic LC phases, and their corresponding X-ray diffraction patterns on a two-dimensional detector are shown. Since q = 2π/d, thus, the diffraction patterns recorded toward the outer edges of an image plate detector correspond to a shorter dimension and the ones seen near the center of the image plate correspond to longer dimension. The sharpness of the peaks is qualitatively related to the spatial range of periodic order occurring in the system. In the isotropic phase, i.e., without a long-

range positional or orientational order among particles, the diffraction pattern is made of weak diffuse rings Figure 5-3a. Any diffraction pattern can be observed in the isotropic state since a short-range positional order exists in classical liquids. It demonstrates the distance between the particles along their widths.

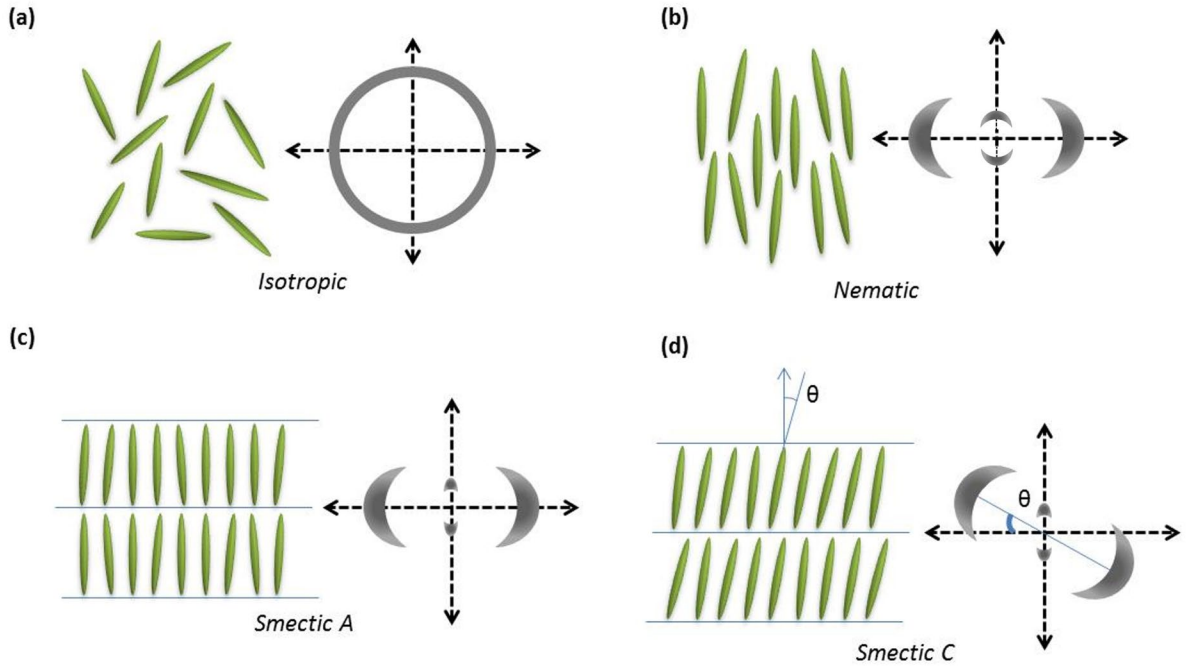

Figure 5-3. Schematic of 2D X-ray diffraction of various types of LC phases: (a) isotopic, (b) nematic, (c) smectic A, and (d) smectic C [128].

LC is a transitional state between solid and liquid phases. Nematic LC phases have long range orientational order and short-range positional order between the particles. In nematic phases, the particles prefer to align along a macroscopic direction, specified by the director ***n*** but the centers of mass of the molecules are still randomly distributed. In Figure 5-3b for an aligned sample of mesophase nematic LC, X-ray diffraction patterns display two sets of diffuse spots with the form of broad arcs at perpendicular directions: one set with two symmetrical arcs at low scattering angles and along the direction of alignment, the second set is made up of two

symmetrical arcs perpendicular to the direction of alignment and at larger angles. The diffuse arc at the larger radius represents the distance between particles along their widths.

An unaligned sample of nematic LC has a diffraction pattern similar an isotropic state, however in place of a diffuse ring, its diffraction pattern shows a sharper intensity distribution. In the unaligned state, the X-ray diffraction pattern might still look like the isotropic phase but even a weak external stimulus like electric field, results a field-induced anisotropy of the system and brings in a dramatic change in the macroscopic uniformity of the nematic phase that is easily detected in the X-ray diffraction experiments.

In smectic phases, the molecules' centers of mass are restricted in their motion in at least one direction. Within the layers, the molecular motion is liquid-like but molecular movement perpendicular to the layers is restricted. In the case of the smectic-A phase, the X-ray beam probing the layers gives rise to an X-ray pattern as shown in Figure 5-3 c and two sets of diffuse peaks are detected in diffraction pattern. The diffuse peak at small angles condenses into sharp quasi-Bragg peaks. On the other hand, because molecules within the smectic planes are arbitrarily organized, the peak intensity distribution at large angles are not very sharp. Due to the presence of one-dimensional translational order, the small-angle peaks become dramatically sharper as compared to the nematic phase.

A smectic-C phase has the same translational symmetry of the smectic-A phase but differs in rotational symmetry. Molecules in the SmC phase are tilted with respect to the layer normal, Figure 5-3d. In an aligned sample, the distinction between the SmA and SmC phases can be made from the angular separation between the large and small angle reflections. This angle can easily be understood in the diffraction pattern as the diffuse peaks at smaller and larger angles are not anymore perpendicular to each other. The large angle peaks now rotate relative to the small angle peaks by an amount equal to the tilt angle (θ). As the particles tilt, the layer spacing

will also decrease and the small angle reflections move away from the center by a factor. The value of smectic spacing d calculated from the position of the quasi-Bragg peak can also be used to estimate θ.

5.2 SAXS measurements at ALBA synchrotron

ALBA (in Catalan and in Spanish meaning "Sunrise") is a third-generation synchrotron light source facility sited in the Barcelona Synchrotron Park in Cerdanyola del Vallès neighboring Barcelona, in Catalonia (Spain), Figure 5-4a. I was granted two days (6 shifts) time at beam line BL11 - NCD-SWEET to conduct my SAXS measurements.

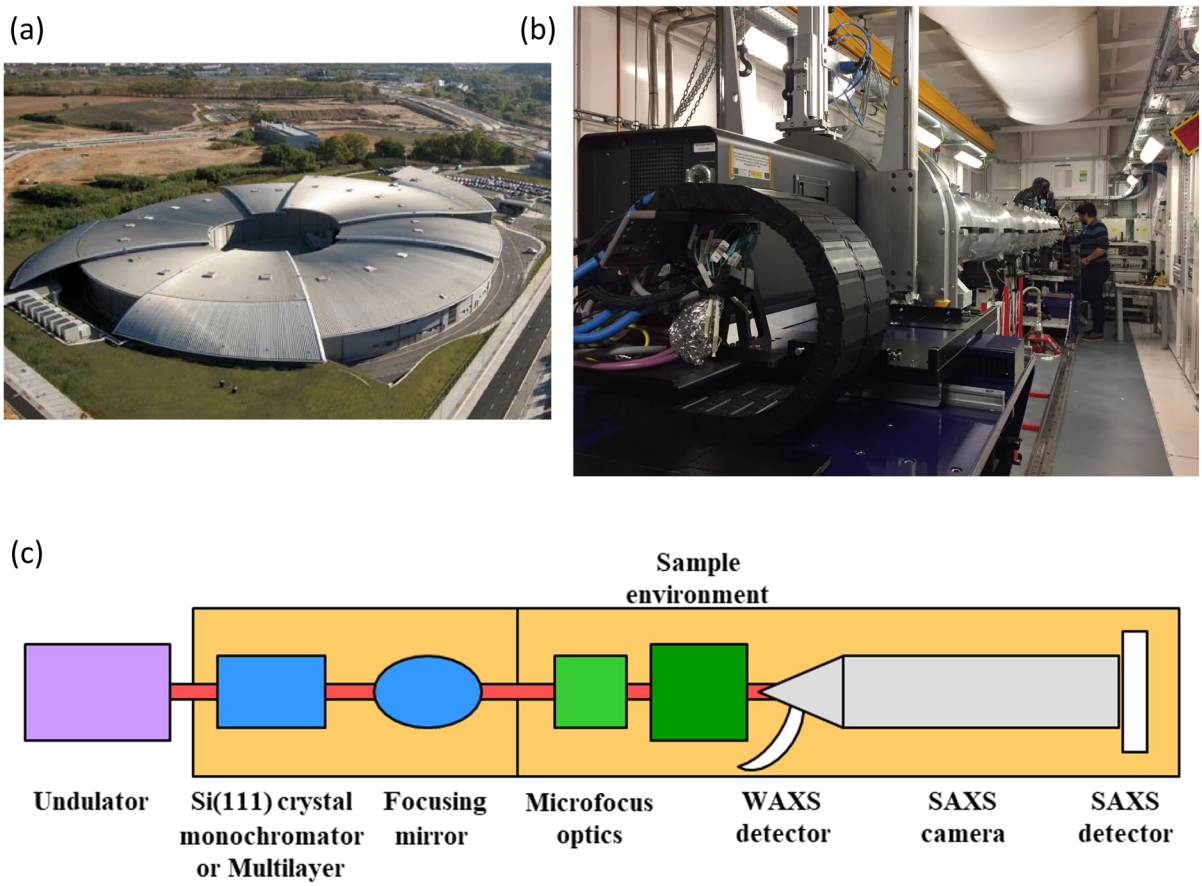

Figure 5-4. (a) ALBA synchrotron, (b) the experimental cabin of BL11 - NCD-SWEET beamline, (c) a scheme of the beamline.

Figure 5-4b shows the experimental cabin of the beamline area where is accessible to the beamline users. Figure 5-4c is a simplified schematic of the beamline showing its main parts. The experimental cabin of the beam line is at right side the schematic including the sample environment. In Figure 5-4b, my location indicates the place where I mounted my samples before the long tube, the SAXS camera. The long tube is under vacuum, and it is the flight paths for the X-ray beam after passing the sample. At its end, the tube is attached to SAXS detector that is seen as a big box at a close distance in the picture. At ALBA, I performed my SAXS measurements with support of my local contact, Dr. Eduardo Solano Minuesa who helped me to use the facilities there.

At NCD-SWEET beamline, I used an X-ray beam having fixed wavelength of 0.99987 Å. I employed the longest sample to detector distance of 6.35 m to reach the highest possible resolution at the lowest q because I expected an interparticle spacing higher than 100 nm for GO flake in their suspensions. I used an exposure time of 30 seconds since the low concentrations of the GO suspensions results in a low scattered light counted by the detector. The beam size at sample position was 150×150 μm^2, which allowed using small steps measurements for a precise mapping of GO flakes orientational order in the confined space of cells. I performed the synchrotron SAXS measurements using the normal designed cells, but because of high absorption of X-ray beam by glass substrates, I used thin glass substrates with a thickness of 160 μm to reduce the X-ray beam absorption.

5.2.1 SAXS measurement at the center of cell

For processing and reducing the measured data, I used DawnDiamond software which is an open-source software for the visualization and processing of SAXS data. In the data processing, the raw data were normalized against a transmission measurement and the background was

corrected using a blocked beam measurement. Figure 5-5 shows the 2D measured SAXS patterns at the center of 3 mm cell that was filled with 2 mg/mL GO suspension, after calibration and masking. For 2 mg/mL GO suspension, the anisotropy of the 2D SAXS patterns confirming a strong orientational order of GO flakes [129], [130] and this in agreement with the POM measurements. The expected patterns for a nematic phase with the shape of broad arcs are not evident and the 2D SAXS pattern has an elliptical shape, indicating the variation of the inter-flake spacing in the suspension.

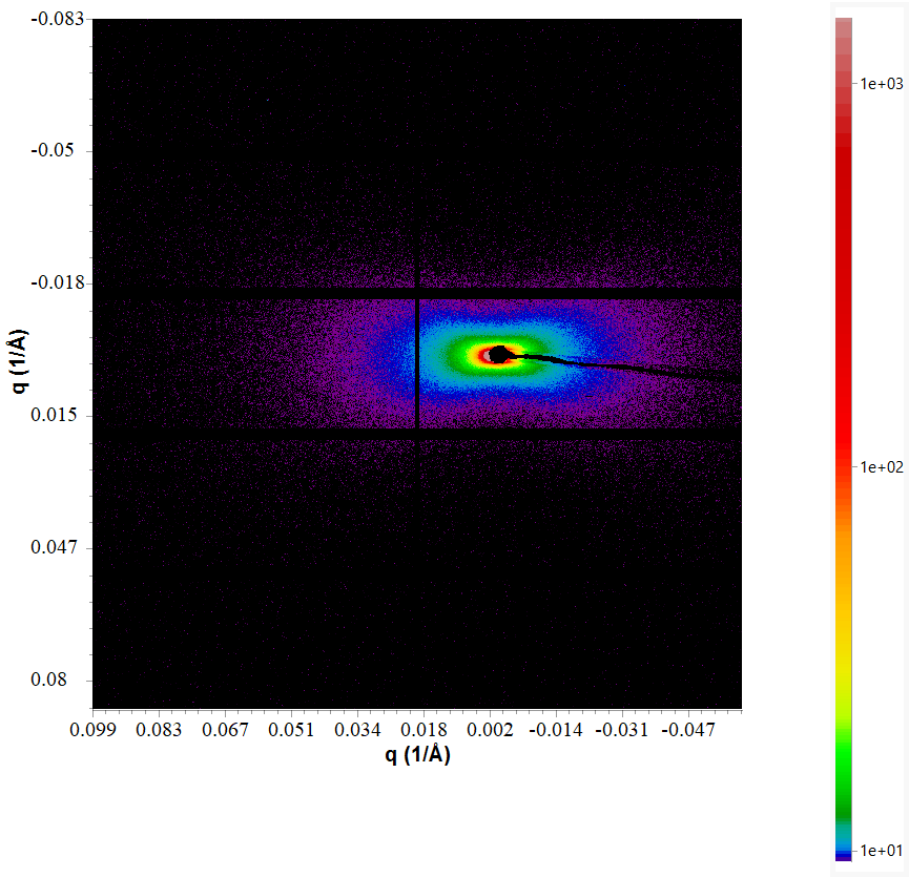

Figure 5-5. 2D SAXS pattern at the center of 3 mm cell filled with 2 mg/mL GO suspension, when the side wall is parallel to the horizontal direction.

For my all measurements, samples were mounted on a sample holder before SAXS camera in a way that the incident X-ray beam was perpendicular to the glass substrate and the side wall

of cells were parallel to the horizontal direction. In Figure 5-5, the elliptical SAXS pattern has an orientation in the horizontal direction, indicating that GO flakes have an orientational direction in perpendicular direction i.e., perpendicular to the side wall. This agrees with the POM measurements. However, my SAXS measurements revealed the great perpendicular orientation of GO flakes at very central area of cell, even without applying an electric field.

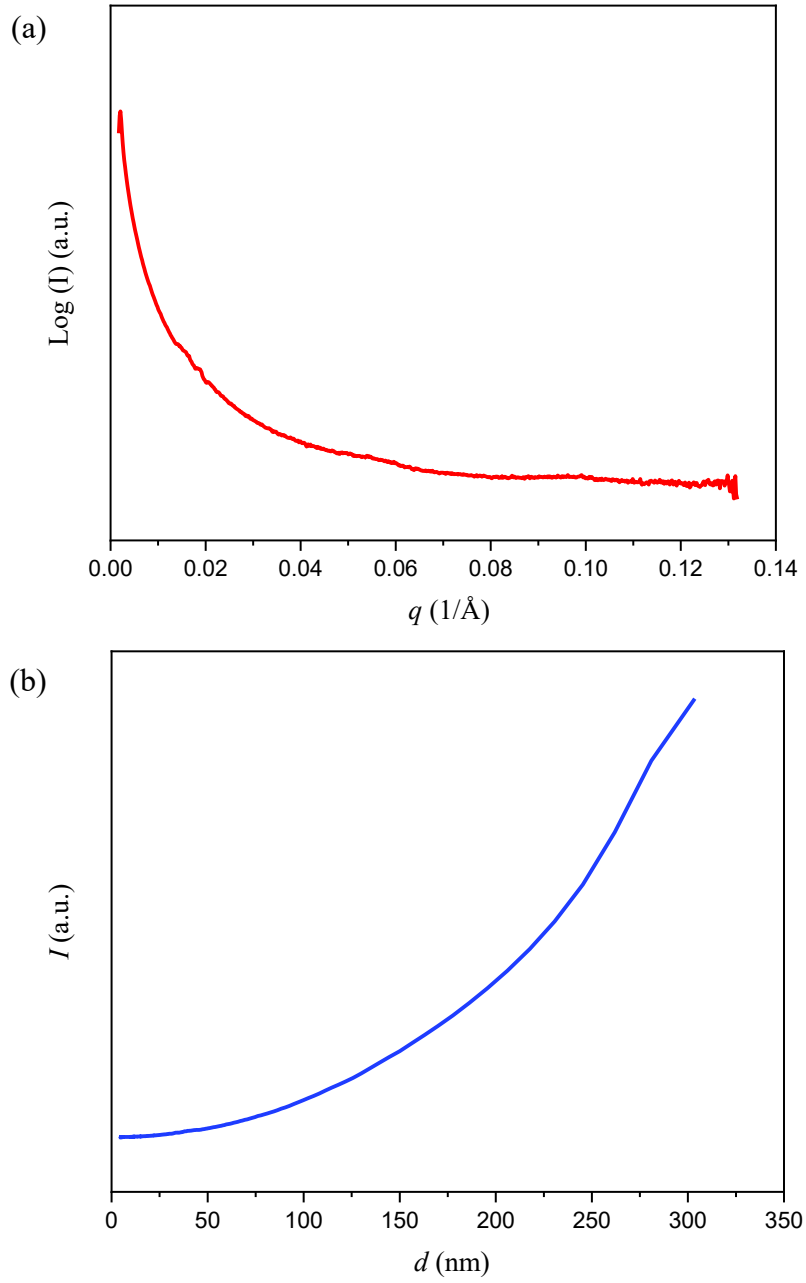

Figure 5-6. Profiles of scattering intensity as a function of (a) scattering vector q (1/Å) and (b) d-spacing (nm), at the center of 3 mm cell filled with 2 mg/mL GO suspension

Figure 5-6a shows the profiles of scattering intensity as a function of scattering vector q. To obtain 1D scattering patterns, the 2D scattering patterns were integrated using azimuthal integration (360-degree angle). There is no evident peak in the measured q range, 0.002 to 0.13 $Å^{-1}$. This means that even though GO flakes form a nematic phase, but the inter-flake spacing in GO suspensions is not homogeneous to result in a strong scattering at the range of q to observe a peak. It is normal for low concentration of GO flakes when they are polydisperse.

Figure 5-6b shows the profiles of scattering intensity as a function of d-spacing (nm) since $d=2\pi/q$. There is no peak between 5 to 300 nm. In some of the 1D scattering patterns, I found a weak peak around 300 nm, however this range of q is very close to the beamstop, so the peak is probably an artificial effect of scattering because of the beamstop. To check for this, it is needed to perform the SAXS measurement at lower q ranges i.e., larger sample to detector distance.

The elliptical shape of the 2D scattering patterns is because of the stronger scattering along the widths of GO flakes in their nematic phase. In cases like GO suspension that show a weak anisotropic scattering, once can compare the 1D scattering patterns along the directions with the maximum and minimum intensity. This way makes it possible to enhance their difference i.e., the scattering along the widths of GO flakes to detect the related peak. Figure 5-7 shows the radial integration of the 2D scattering patterns. The obtained scattering pattering does not have a perfect ellipsoidal shape because of a beamstop artificial effect. The graph indicates that the scattering pattern has orientation toward the horizontal direction. by neglecting the effect of the beamstop, the maximum scattering intensity is at 180- degree angle and the minim intensity at 90- degree angle.

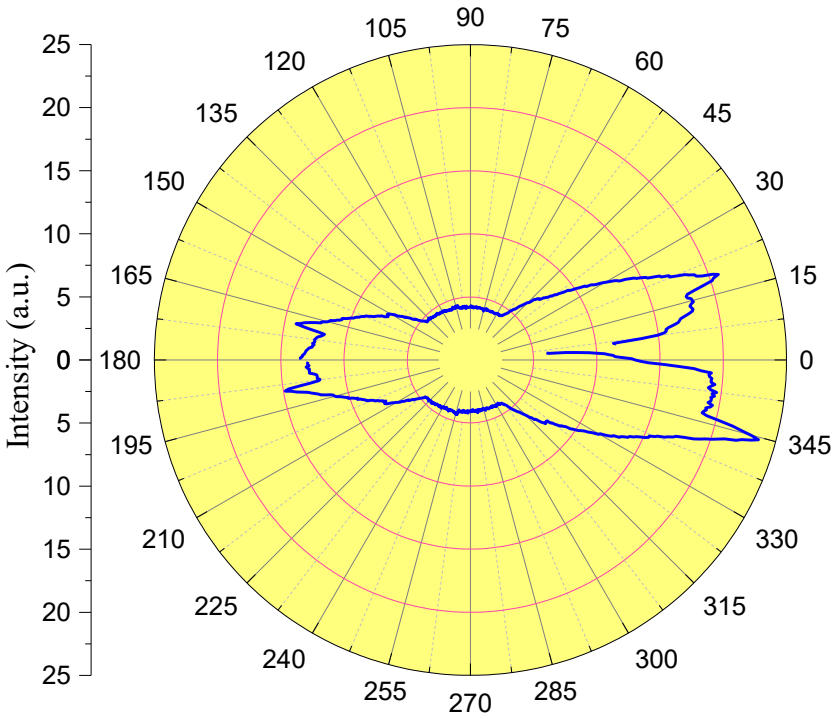

Figure 5-7. The radial integration of the 2D SAXS patterns vs azimuthal angle, at the center of 3 mm cell filled with 2 mg/mL GO suspension

Figure 5-8 shows 1D SAXS profiles obtained by integrating azimuthal cuts of 2D scattering pattern between 85 to 95 and 175 to 185- degree angle. As expected, there is a higher profile intensity between 175 to 185-degree angle. However, still I could not find a peak for X-ray scattering along the widths of GO flakes in their nematic phase. The gap in the 1D profile lines is because the SAXS detector is actually made of some small pieces and between them there are gaps where scattered photons are not detected. The small peaks in the full 1D profile are not real and they are the results of the gaps in the detector.

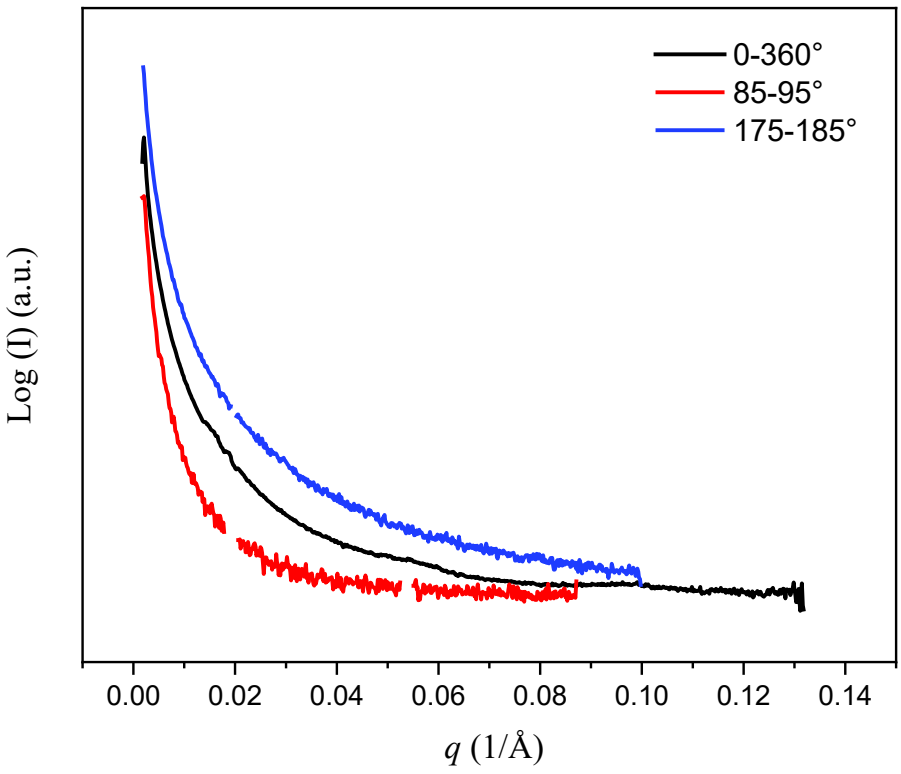

Figure 5-8. 1D SAXS profiles by different radial integration of the 2D SAXS pattern, at the center of 3 mm cell filled with 2 mg/mL GO suspension

Figure 5-9 shows the double-logarithmic plot of SAXS intensity versus q. Between 85 to 95-degree angle, the scattering profile is weak, but the two other 1D SAXS profiles show a linear region having a slope of -2. If the plot of the log I vs. log q forms straight-line section, then it is a sign of a fractal-type structure. The slope of -2 i.e., $I \propto q^{-2}$, is indicative of scattering from a flat, planer structure. For disk shape particles with diameter of D, thickness of T and having size scales of 1/q between the disk particles, the number of scattering domains is equivalent to the disk surface, D^2, divided by the scattering area size, $1/q^2$, or $N_p = D^2q^2$. In addition, the number of electrons per scattering domain is determined by the volume of a domain, T/q^2. Since, the scattering intensity is proportional to the number of scattering elements in the irradiated volume, then $I(q) = D^2T^2/q^2$, or $I(q) \propto 1/q^2$ [123], [131]–[134].

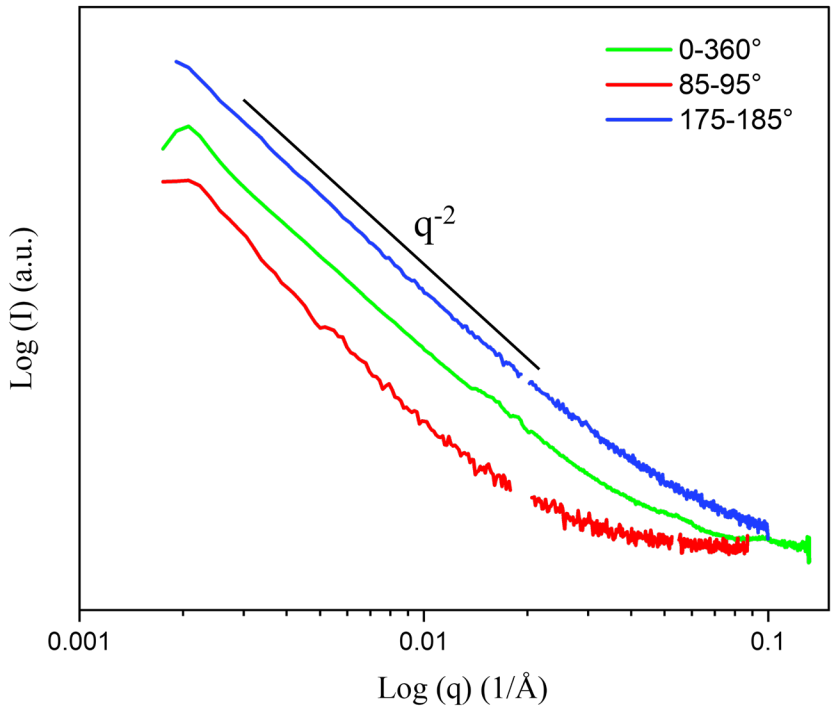

Figure 5-9. The double-logarithmic plot of SAXS intensity versus q for different radial integration of the 2D SAXS patterns, at the center of 3 mm cell filled with 2 mg/mL GO suspension

5.2.2 SAXS measurement at the side of cell

The POM measurements indicated that GO flakes have an orientation parallel to the electrodes at the cell side. This is what my SAXS measurements at very close distance from the electrodes, Figure 5-10, also confirmed. The 2D SAXS patterns indicate that GO flakes have a great orientation in the horizontal direction i.e., parallel to the electrodes. Figure 5-11 shows the radial integration of the 2D scattering patterns. By neglecting the beamstop effect, the obtained scattering pattering have a full ellipsoidal shape. This is because of GO flakes form a concentric layer driven by shear flow and homeotropic anchoring on the surface of the electrodes, result in a stronger scattering in comparison with the center of cell. The graph indicates that the scattering pattern has orientation toward the vertical direction and the maximum scattering intensity is at 90- degree angle and the minimum intensity at 180- degree angle.

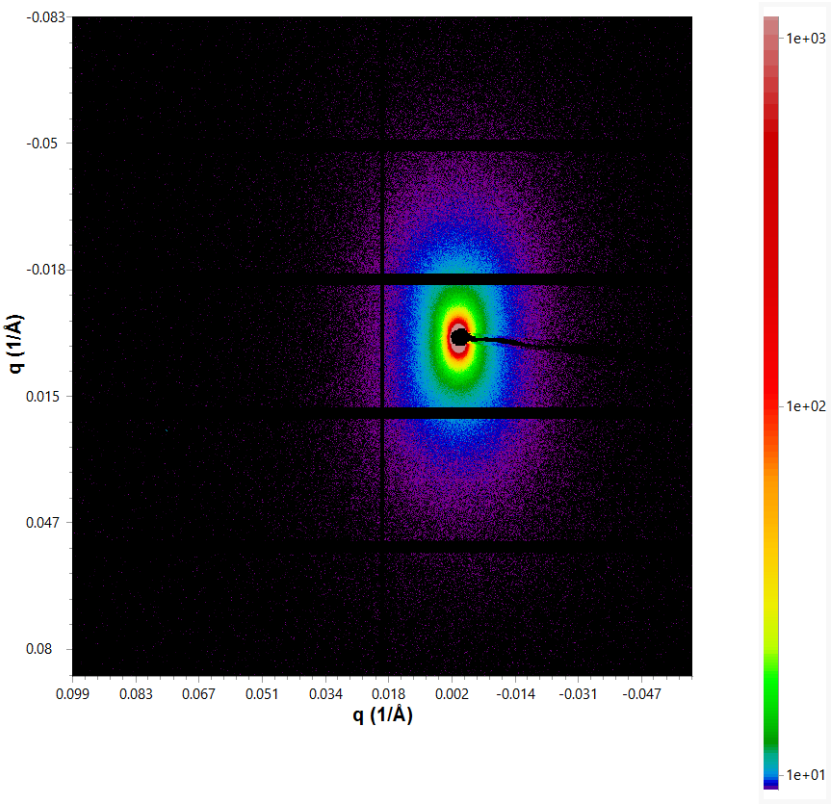

Figure 5-10. 2D SAXS pattern at a close distance to the cell side of 3 mm cell filled with 2 mg/mL GO suspension, when the cell side is parallel to the horizontal direction.

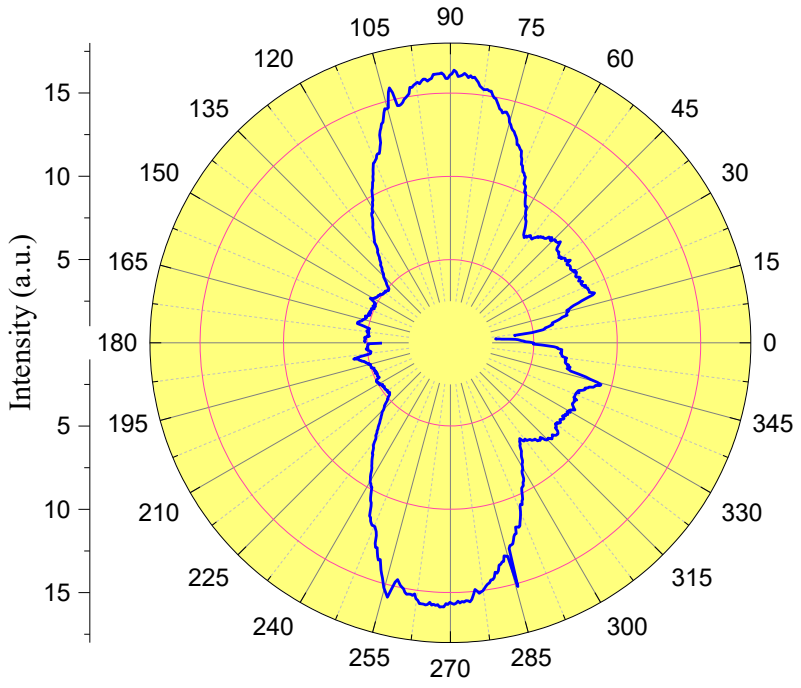

Figure 5-11. The radial integration of the 2D SAXS patterns vs azimuth angle, at a close distance to the electrode side wall of 3 mm cell filled with 2 mg/mL GO suspension

Even at the side of cell, the 1D SAXS profiles at maximum intensity direction, obtained by integrating azimuthal cuts of 2D scattering pattern between 85 to 95- degree angle, does not show a peak for X-ray scattering along the widths of GO flakes, Figure 5-12. This is because of inter-flake spacing variation and an effective reason on that is the superflexibility of GO flakes making them to have curvatures when they are dispersed in suspensions [113]. In the double-logarithmic plot of SAXS intensity versus q, Figure 5-13, all the 1D SAXS profiles show a linear region having a slope of -2, $I \propto q^{-2}$, which is indicative of scattering from a flat structure.

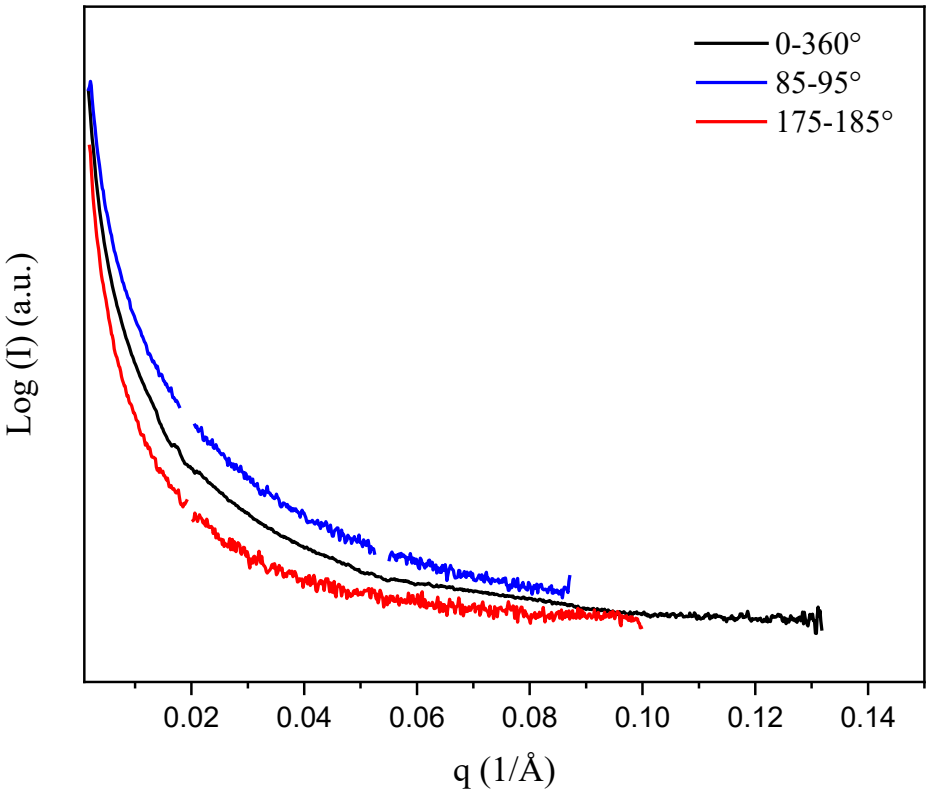

Figure 5-12. 1D SAXS profiles by different radial integration of the 2D SAXS patterns, at a close distance to the cell side of 3 mm cell filled with 2 mg/mL GO suspension.

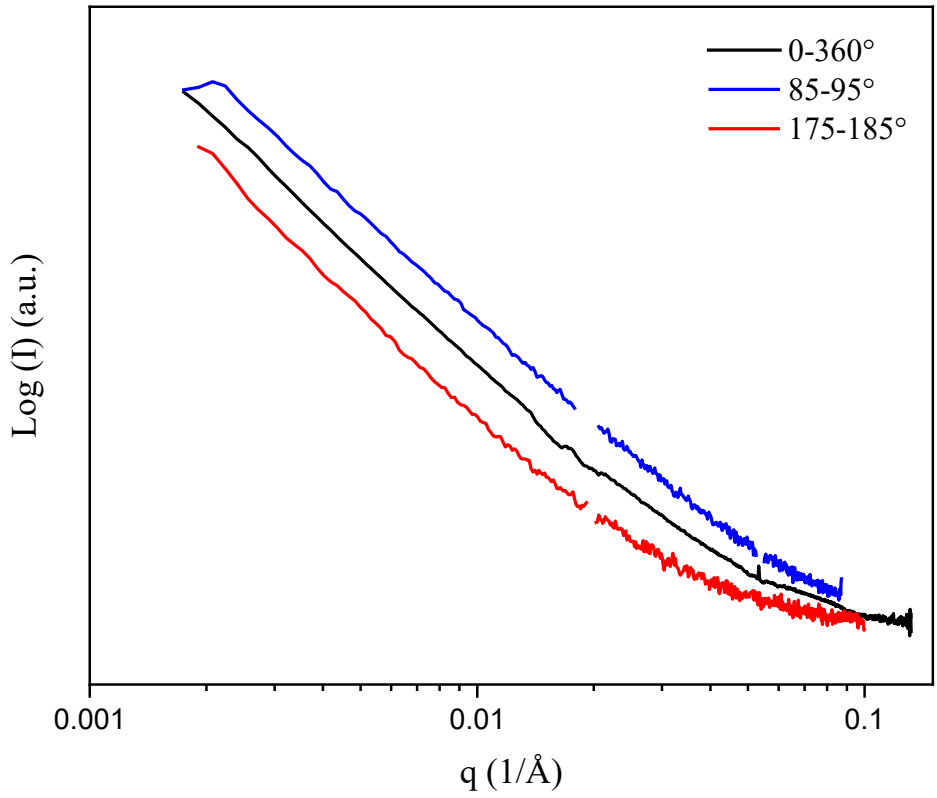

Figure 5-13. The double-logarithmic plot of SAXS intensity versus q for different radial integration of the 2D SAXS patterns, at a close distance to the cell side of 3 mm cell filled with 2 mg/mL GO suspension

5.2.3 Mapping the GO flakes orientation direction by SAXS

To determine the variation of GO flakes orientations in the confined spaces of cell, I performed a precise SAXS measurements on a 3 mm cell filled with 2 mg/mL GO suspension and I scanned the whole cell using a small step measurement. Figure 5-14a-e shows the elliptical SAXS diffusive patterns for different areas in the cell. The anisotropy of the SAXS patterns confirming a strong orientational order of GO flakes in the whole cell, in agreement with my POM measurements. Figure 5-14a and e indicate the orientation of GO flakes close to the sides walls and being parallel to the electrodes. At closer distances to the center of cell, the GO flakes

orientations are between parallel to perpendicular to the side walls, Figure 5-14b and d, which are getting more perpendicular when we move to the center. Figure 5-14c, shows the elliptical SAXS diffusive pattern for a narrow area at the center of cell, where GO flakes have a clear preferred orientational order perpendicular to side of cell. Figure 5-14f demonstrates a summary of GO flakes orientational order in different areas in the cell.

The SAXS measurements revealed that GO flakes orientational order transition from parallel at side to perpendicular at center, actually happen in a large area which our POM measurements could not clarify exactly. In addition, I should mention that the transition is not continuous as the rotation of SAXS patterns orientation from side to center of the cell, from horizontal to vertical, is not continuous. The different GO orientational order in a cell resemble a profile of laminar follow, which indicated as a dash line in figure 5f. It is indeed the profile of GO suspension flow when we fill a cell. I observed this flow-induced self-assembly in all cells with different thickness, even in thin cell with 300 μm thickness where the capillary effect is also a motivation for GO suspension to fill the cell. This proves that a weak shear force is enough for flow-induced assembly of super-flexible GO flakes [135].

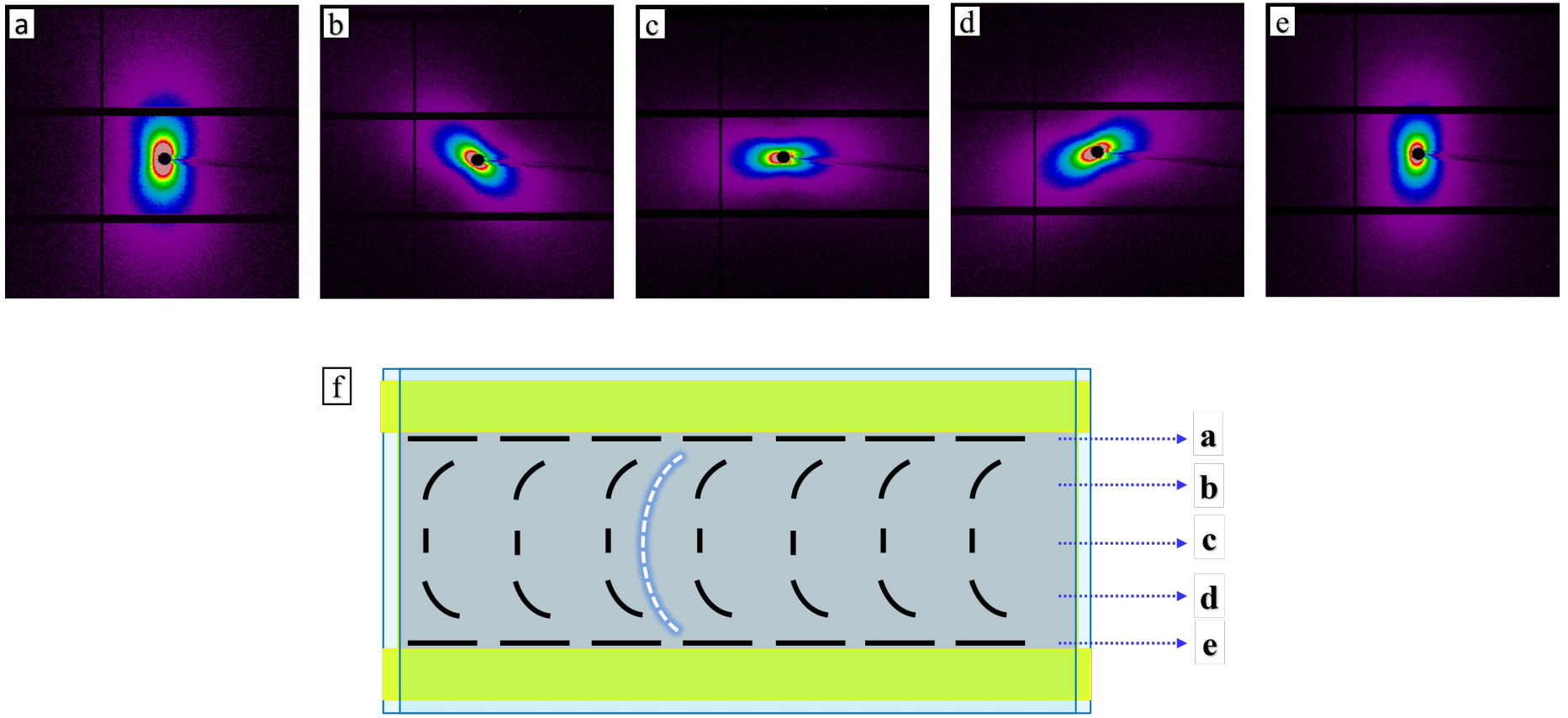

Figure 5-14. (a-e) The 2D elliptical SAXS diffusive patterns measured for 2 mg/mL GO suspension in different areas of a 3mm cell which are indicated in f. (f) Schematic of GO flakes flow-induced orientational order in different areas of the cell.

5.2.4 Tracking GO flakes reorientation under electric field by SAXS

At ALBA synchrotron, I performed SAXS measurements during GO flakes electro-optical switching process to study the reorientation of GO flakes under high frequency electric fields.

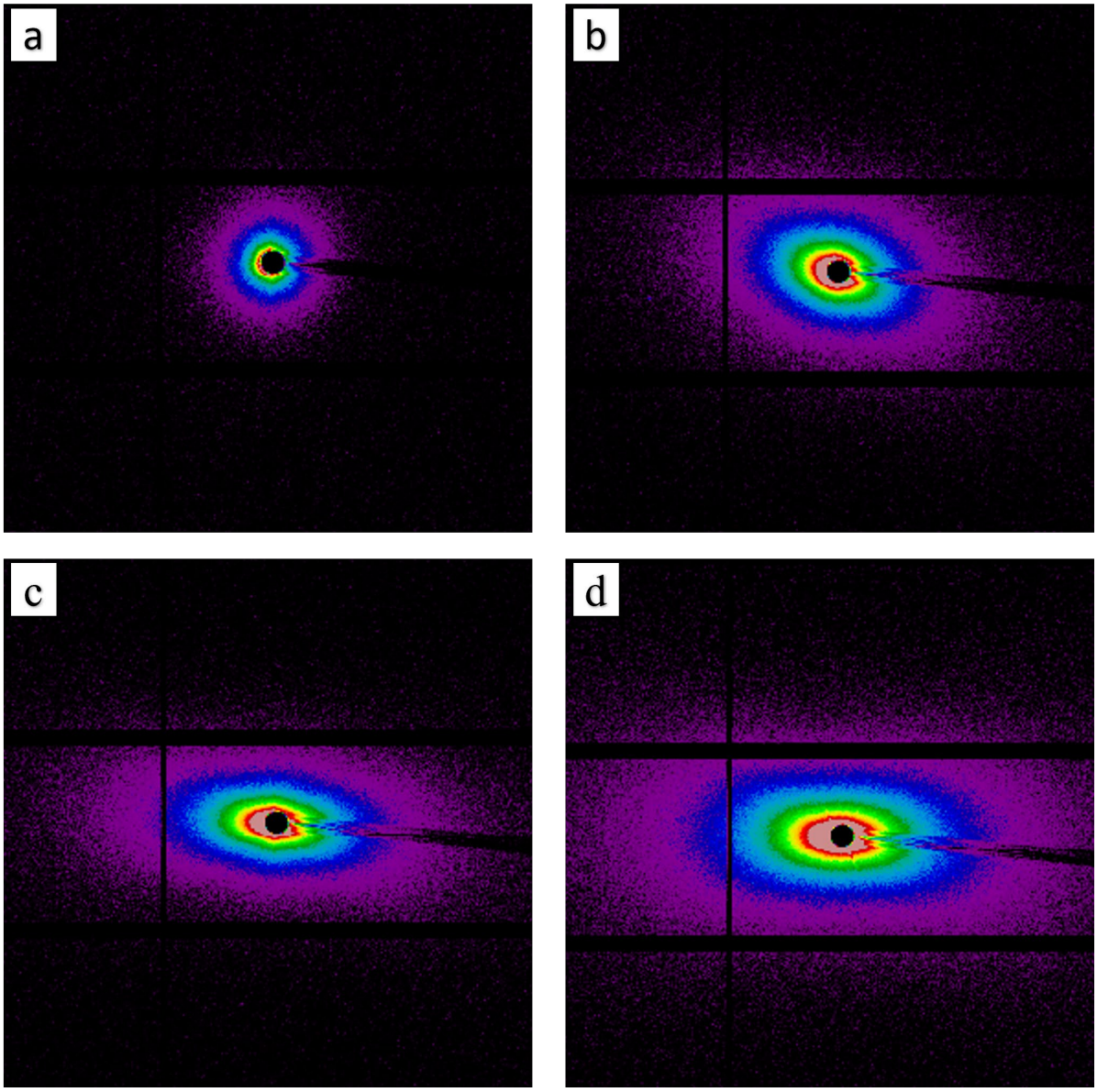

Figure 5-15. The 2D SAXS diffusive patterns measured for 2 mg/mL GO suspension at the center of a 300 µm cell during electro-optical switching: (a) without electric field, and under 7.5 volt/mm electric field (b) at the beginning, (c) at 30 seconds, (1) at 1 minute. The electrodes are along the horizontal direction.

For this aim, I used the same setup that I normally used for the electro-optical switching of GO flakes, consists of a function generator producing square electrical waveforms and an amplifier. I placed the setup in the experimental cabin, and I control the electric field by laptop from the control cabin of the beamline. To perform the electro-optical switching process, I used 300 μm cells filled with 2 mg/mL GO suspension, and 7.5 volt/mm electric field with 10 kHz frequency. Figure 5-15 shows the 2D SAXS patterns at the center of the cell during the electro-optical switching process.

Without applying an electric field, I could not observe any anisotropy, Figure 5-15a, revealing a very poorly aligned sample. In the confined space of 300 μm cell, large GO flakes cannot freely self-organize into a large nematic domain and they distribute in small and almost randomly oriented nematic domains [129]. This is what my POM measurement also revealed. By starting to apply the electric field, I could observe appearance of an anisotropy, Figure 5-15b, indicating the beginning of GO flakes switching to have an orientation parallel to the electric field direction (along the vertical direction). At 30 seconds of applying electric field, Figure 5-15c, the strong anisotropy and an elliptical pattern with a larger axial ratio indicates a strong orientational order of GO flakes in the direction of electric field. By increasing time, Figure 5-15d, the GO flakes alignment were enhanced and they are well orientated to the electric field direction, as our POM measurements revealed too. No diffuse arc, i.e. the Bragg reflection, in the patterns indicating the sole orientational ordering and no positional ordering [13]. A low electric field is enough to overcome the initial self-assembly of flakes, but as soon as I switch off the electric field, the anisotropy of SAXS pattern disappears. This means that GO flakes lower their free energy when they form randomly oriented nematic domains in the confined space of our 300 μm cells and there is a competition between flow-induced and field induced alignment. In fact, the artificial alignment of LC wants to spontaneously relax to a

random distribution as it is nonequilibrium state for LC. The relaxation characteristics of GO LCs determine the stability of flow-induced assemblies [25].

5.3 SAXS measurements at ESRF synchrotron

My SAXS measurements at ALBA synchrotron allowed me to precisely determine the orientational order of GO flakes in the confined spaces of a cell. Beside the GO flakes orientation, I was also interested in studying the effect of concentration on GO flakes assembly, especially to determine the inter-flake spacing in GO suspensions. For this reason, I applied for a time at ID02 beamline at European Synchrotron Radiation Facility (ESRF) and I was granted three days (9 shifts) time to conduct my SAXS measurements.

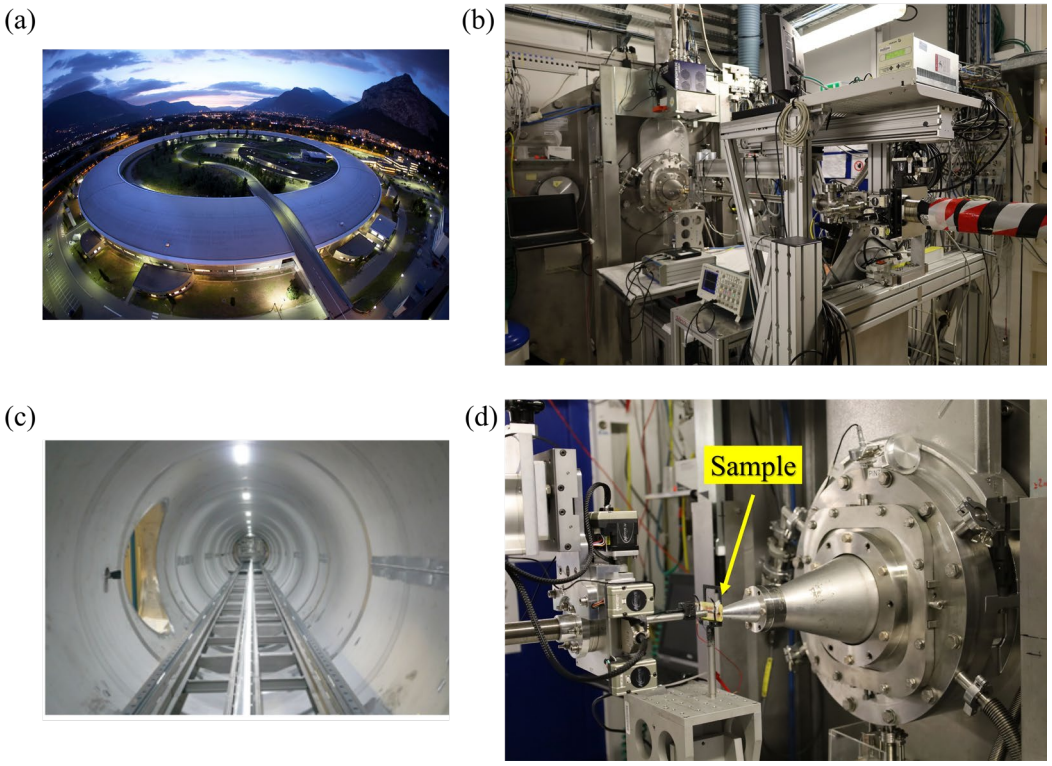

Figure 5-16. (a) ESRF synchrotron. (b) Experiment station at ID02 beamline. (c) A view of the detector tube having 34 m long and 2 m diameter from inside having the detector carriage at the end. (d) The photo displays incident side telescopic tube, the sample mounted on the sample table, and the entrance cone of the detector tube.

The ESRF is a joint research facility situated in Grenoble, France, Figure 5-16a, and after the second improvement to the facilities, now named the "Extremely Brilliant Source" (ESRF-EBS). ESRF became the first fourth-generation high-energy synchrotron in the world. Beamline ID02 at the ESRF is a multipurpose instrument adjusted for time-resolved small-angle X-ray scattering (TR-SAXS) with high angular resolution. Figure 5-16b to d represents the experiment set-up having an evacuated detector flight tube with 34 m length. The sample – detector distance can be changed from about 1 m corresponding to the typical SAXS range to 31 m spanning the USAXS region. The set-up covers a wide range of q, from 10^{-3} nm^{-1} to approximately 60 nm^{-1}, equivalent to a real space dimension from about 0.1 nm to 6 µm. Access to such an extensive range of size scales was the most interesting point to do my SAXS measurements at ESRF. Moreover, a point detector embedded in the beamstop simultaneously recorded the transmitted primary beam intensity for a precise normalization of measured scattered intensities to dS/dW [127].

For my measurements At ID02 beamline, the X-ray beam had a fixed wavelength of 1.01377 Å and the sample to detector distance was 30.65 m to reach the highest scattering profile resolution at the lowest q. The ESRF extremely brilliant source (EBS) allowed to use an exposure time of 2 seconds. The beam size at sample position was 100×100 $µm^2$, for a precise mapping of GO flakes orientational order in the confined space of cells. I performed my SAXS measurements at ID02 beamline with support of my local contact, Dr. Thomas Zinn who helped me to use the facilities there.

Even though, I made my cells using glass substrates with 160 µm thickness, I found that just 20 percent of X-ray beam intensity can pass through an empty 3 mm cell. The transmitted light intensity from a 3 mm cell filled with deionized water was about 8 percent. For a 3 mm cell filed with 2 mg/mL GO suspension, the transmitted light intensity was the same about 8 percent, indicating that GO flakes have a very low X-ray beam absorption. For data processing

and data reduction, I used SAXSutilities2 software which is a free software package has been developed for processing and analysis of Small-Angle X-ray Scattering data. For analyzing my SAXS measurement data, I subtracted from the data the scattering profile for corresponding cell size filed just with deionized water.

5.3.1 Ultra-small-angle X-ray scattering

Figure 5-17 shows the 2D measured USAXS patterns for a 3 mm cell that was filled with 2 mg/mL GO suspension. Although I used an exposure time of 2 seconds to prevent damage of my samples by the ESRF extremely brilliant source, the elliptical SAXS diffuse pattern for GO flakes was still adequately detectable.

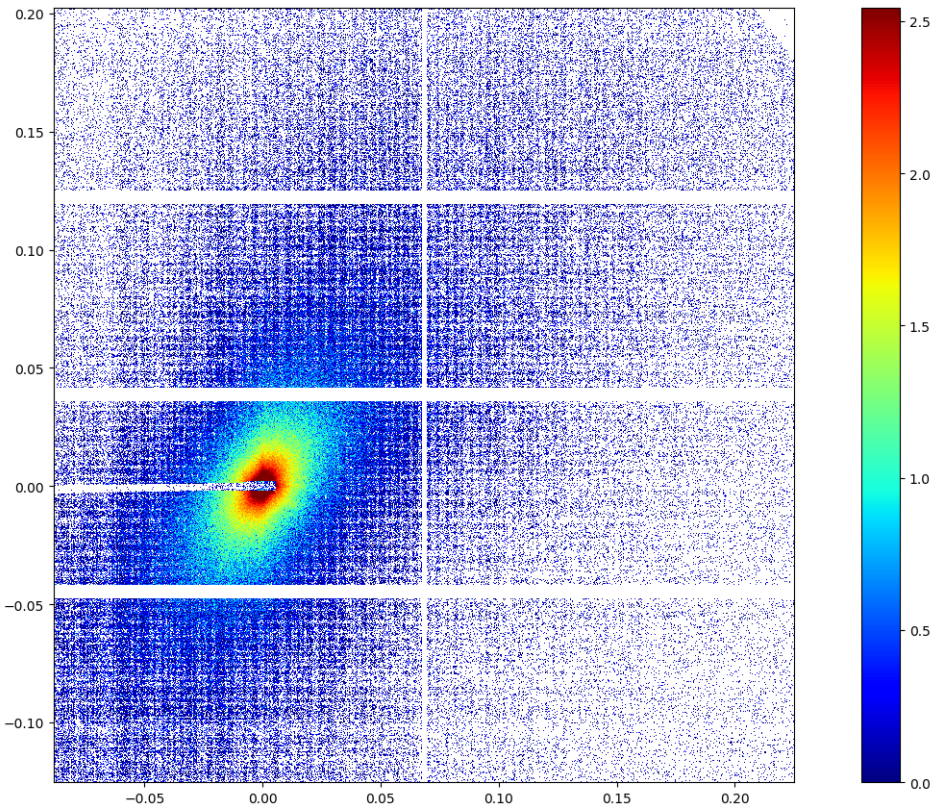

Figure 5-17. 2D USAXS pattern for 3 mm cell filled with 2 mg/mL GO suspension, when the cell side wall is parallel to the horizontal direction.

My USAXS measurement allowed me to study the inter-flakes spacing of GO flakes up to 2.6 µm that was not possible to do at ALBA. Figure 5-18a and b present the profile of scattering intensity as a function of scattering vector q.

(a)

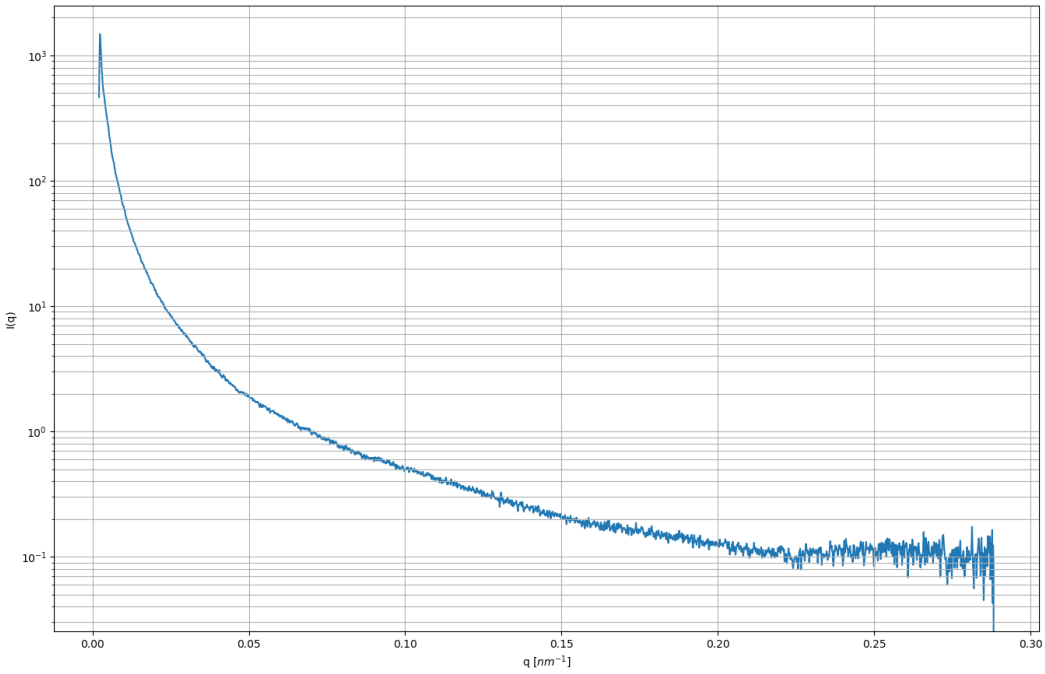

(b)

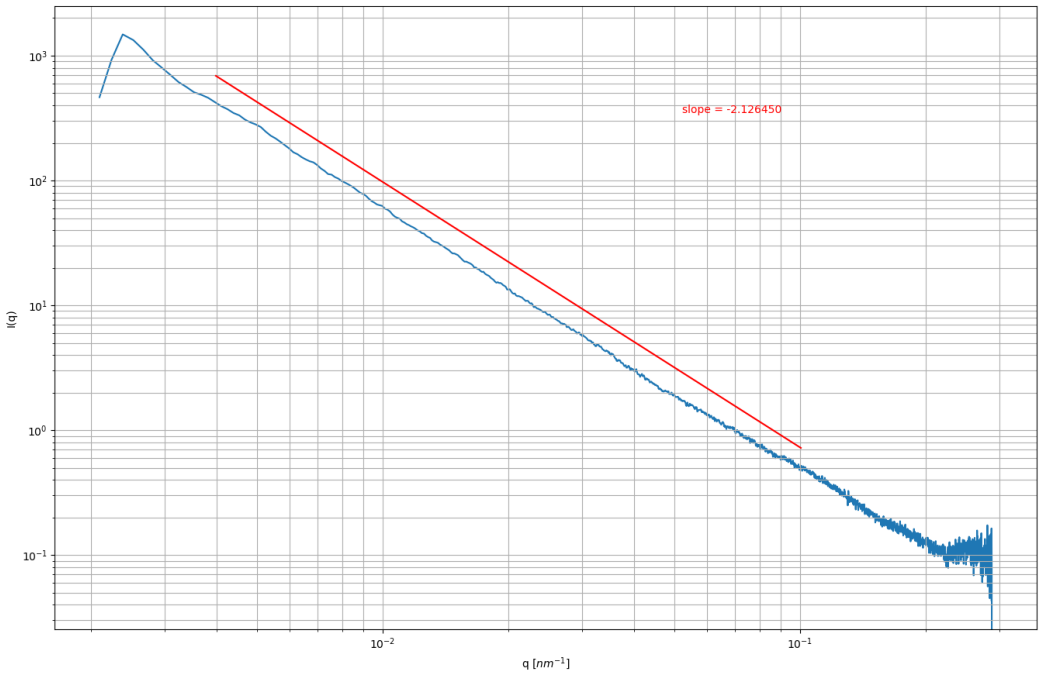

Figure 5-18. (a) 1D USAXS intensity profile versus q and (b) its double-logarithmic plot for a 3 mm cell filled with 2 mg/mL GO suspension.

Even in the q range of 0.0024 to 0.2 nm^{-1}, I could not observe a peak. This again confirms the variation of inter-flakes spacing in GO LC suspensions; a direct result of GO flakes polydispersity and superflexibility. Furthermore, the double-logarithmic plot of SAXS intensity versus q in the ultra-small q range, Figure 5-18b, shows a linear region having a slope of -2 i.e., $I \propto q^{-2}$; indicative of scattering from a flat structure.

(a)

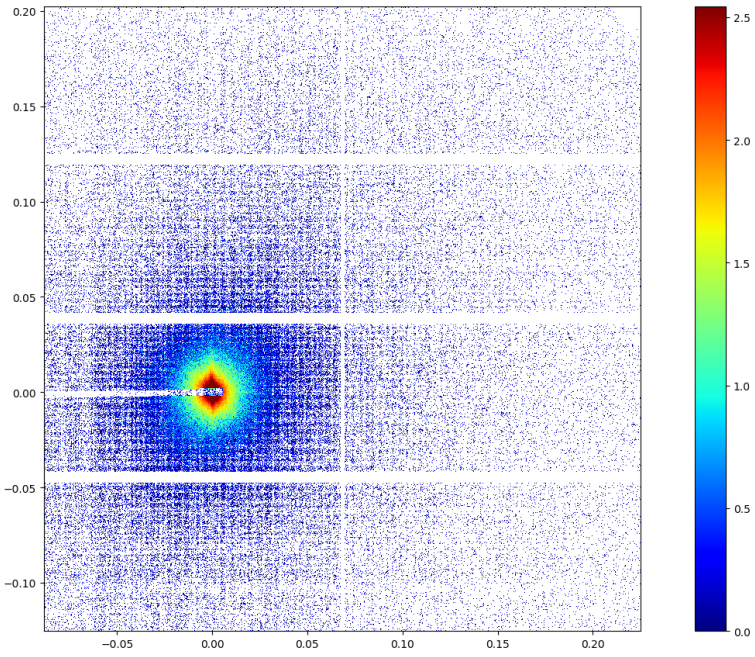

(b)

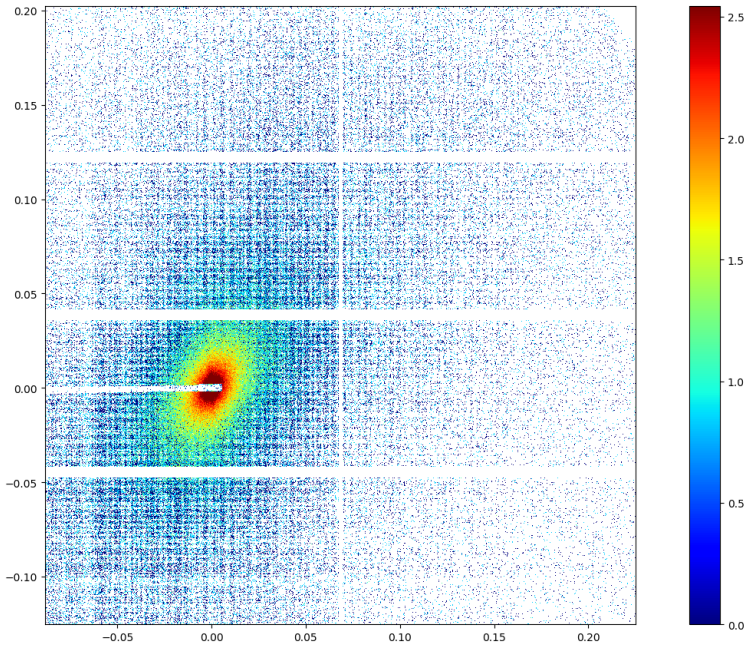

Figure 5-19. 2D USAXS pattern for 2 mg/mL GO suspension in a (a) 1 and (b) 5 mm cell

At ESRF, I performed USAXS on 2 mg/mL GO LC suspension in cell with gap distances between 1 to 5 mm to study the effect of the confined space of cells on GO flakes assembly. For the 1 mm cell the 2D USAXS pattern shows a weak anisotropy and it is almost circular, Figure 5-19a. This indicates that even 1 mm gaps distance is not enough for large GO flakes to gain their ideal self-organization. Figure 5-19b shows 2D USAXS pattern for a 5 mm cell having a strong anisotropy and an elliptical pattern with a larger axial ratio. This reveals a stronger orientational order of GO flakes when there is enough freedom for them to ideally self-organize. I also tried to study the effect of concentration on GO flakes assembly using the ESRF extremely brilliant source. Hence, I prepared 3 mm cells filled with GO suspension having different concentrations from biphasic to pure LC phases. However, even for 1 mg/mL GO suspension the 2D USAXS pattern showed a weak anisotropy, Figure 5-20.

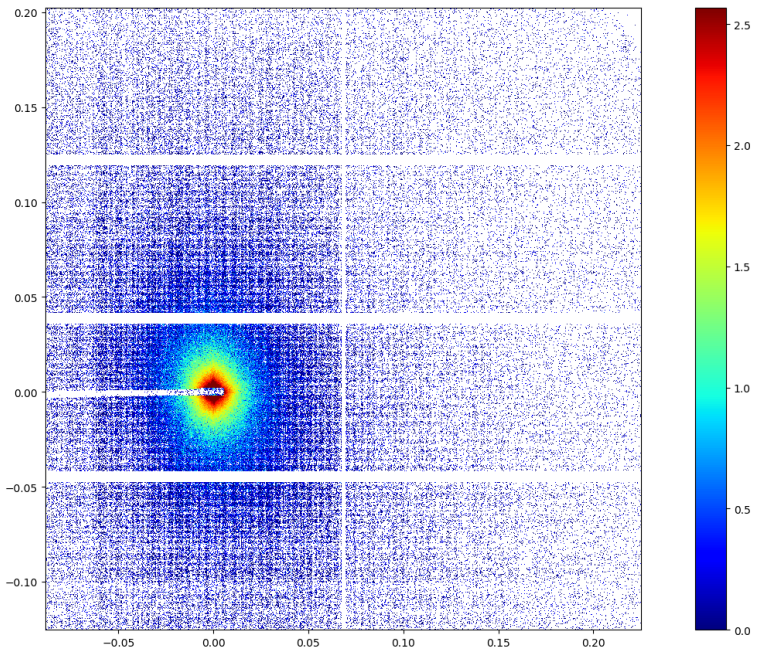

Figure 5-20. 2D USAXS pattern for 1 mg/mL GO suspension in a 3 mm cell

Chapter 6: Direct visualization of GO flakes assembly

Forming LC phase at low concentrations and having different preferred orientational order in different parts of the cells, makes essential the direct visualization of GO flakes in their suspensions to understand and control their assembly. The direct and individual visualization of GO flakes assembly in their suspension is the part of one decade discovery and studies of GO LC phases that is missing [12]. During my study on GO flakes properties, I found that the large single-layered GO flakes that I studied, are highly fluorescent, making them individually discernible using confocal laser scanning microscopy (CLSM). Hence, I decided to examine the GO suspensions using CLSM to carefully determine the assembly of large GO flakes.

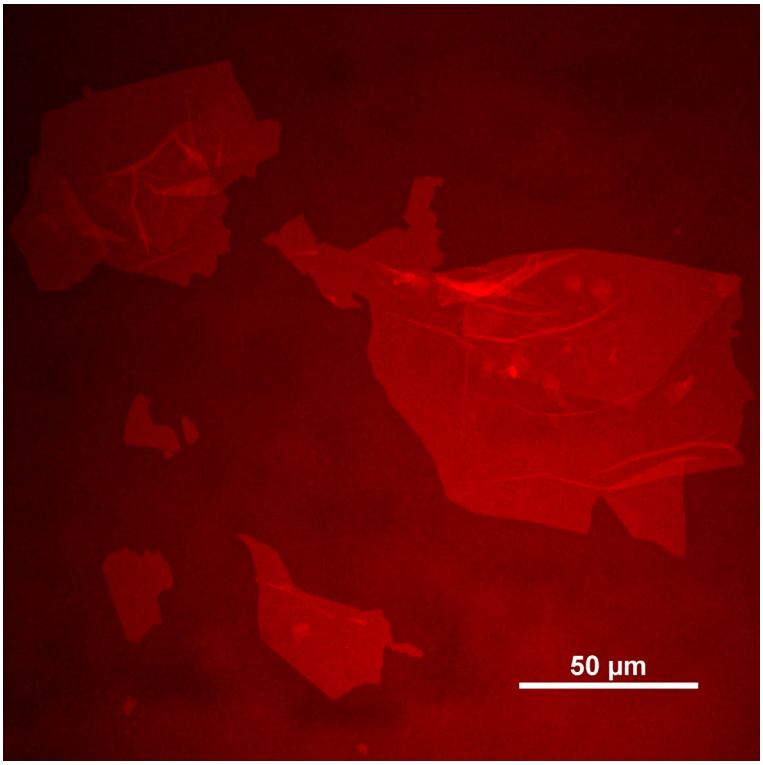

Figure 6-1. CLSM Image of GO flakes that are sandwiched between two glass substrates

Figure 6-1 shows a CLSM image of GO flakes, sandwiched between a glass slide and cover slip. The GO flakes are greatly fluorescent regardless of their size and it easy to find if the flakes are folded or crumbled. Hence CLSM is a superb nondestructive characterization technique for rapid and individual analysis of GO flakes [136]. CLSM amazingly allows determining the GO flakes assembly in their original GO dispersion in real-time without needing freeze-drying or adding multi-layered fluorescent GO particles [29], [137]. This is crucial since it has been reported that the freeze-dried GO assemblies do not preserve the primary GO alignment inside the aqueous dispersion before drying, and the freezing of water reconstructs the GO assembly. Elimination of the water in the middle of the GO particles, via either sublimation or evaporation, significantly modifies the interparticle interactions and the GO alignment structure [28], [29]. This is known that adding additive, even GO flakes with different sizes, disturb the original self-assembly of GO flakes [20], [138].

6.1 Confocal Laser Scanning Microscopy

When a fluorescent sample is imaged by means of a normal widefield optical microscope, the secondary fluorescence light rays emitted by the sample, which emerge away from the region of interest, often disturbs the resolution of those elements that are in focus. The objective in normal widefield fluorescence microscope focus a broad cone of light ray over a large space of the samples being illuminated equally and simultaneously, as displayed in Figure 6-2. By the widefield microscope the whole volume of the sample over a large area is illumined. A main part of the emitted fluorescence light ray is guided back towards the microscope, and the objective collect and project it into the detector or eyepieces. The outcome is a large amount of signal because of the background illumination and auto-fluorescence come from points above and below the focal plane that severely lowers image contrast and resolution.

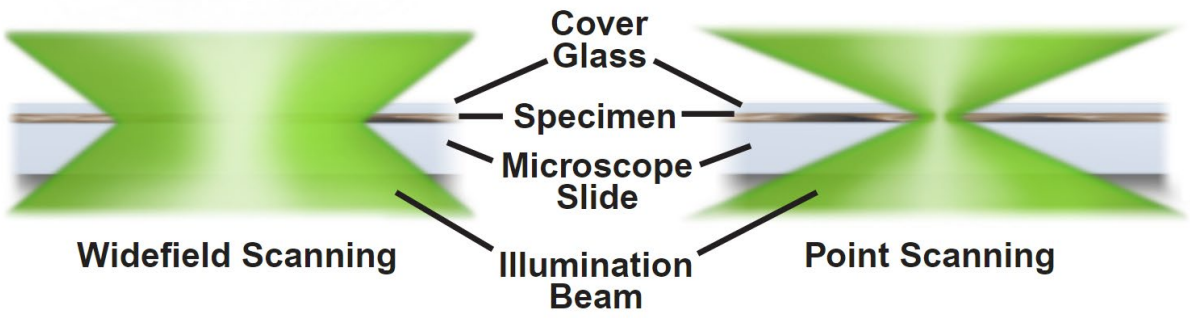

Figure 6-2. A schematic showing normal widefield versus confocal point scanning of samples [139]

In the confocal microscope, the sample is scanned using a delicately focused spot of light, being placed in the focal plane. The fundamental concept in the confocal method is the applying of spatial filtering techniques to remove out-of-focus light rays in samples that have a thickness larger than the immediate plane of focus. Figure 6-3 demonstrates the main light pathways in a basic confocal microscope configuration. Coherent beam produced by the excitation source (laser) go through a pinhole aperture being placed in a confocal plane with a scanning spot on the sample and a second pinhole aperture placed before the detector. As dichromatic mirror reflects the beam light and the beam scans the sample in a specified focal plane, secondary fluorescent emitted light from specified spots on the sample, come back via the dichromatic mirror. Then they are focused on the detector pinhole aperture as a confocal point.

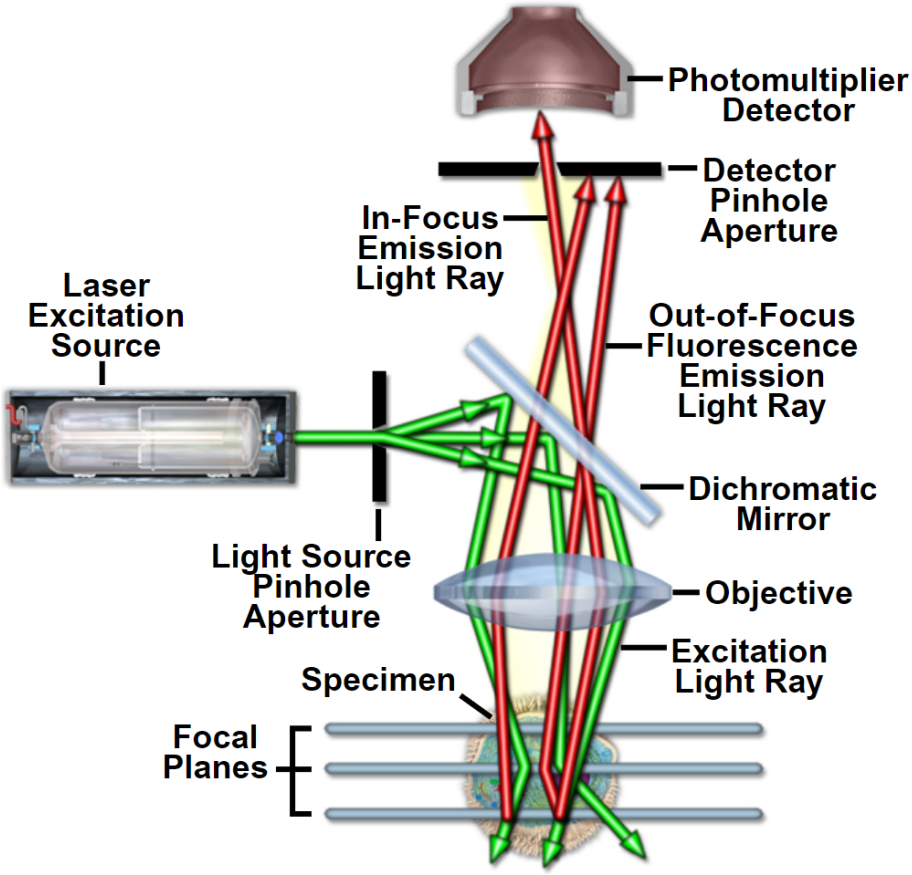

Figure 6-3. Principal Light Pathways in Confocal Microscopy [139]

The main fluorescence emission, which happens at places above and below the objective focal plane are out-of-focus light rays in Figure 6-3 i.e., they are not confocal with the pinhole. Hence, just a tiny percentage of the out-of-focus fluorescence emission are pass through the pinhole aperture and most of them are not detected by the photomultiplier and they do not have an impact on the resulting image. When the objective is refocused in a confocal microscope, the pinhole apertures of the light source and detector becomes confocal with a new place on sample, since the excitation and emission places on a sample shift.

In laser scanning confocal microscopy, for a large sample, the image is produced by probing the focused beam within a specific area. The beam is regulated by two high-velocity oscillating mirrors guided by galvanometer motors. The location of the beam is changed by one of the

mirrors from left to right along the x direction, and the other motor moves the beam in the y lateral axis. By ending each single scan along the x direction, the beam is quickly moved back to the initial point and moved along the y direction to start a new scan in a procedure called flyback. The scanning information is not recorded in the course of the flyback process.

By each scan line along the area in the focal plane, the objective collects the fluorescence emission and send it back the detector. The scanning mirrors moves very slowly comparing to the speed of light; hence the secondary emission sees a light path being is similar to the initial excitation beam. The focused fluorescence emission to the detector is converted into an analog electrical signal by the photomultiplier, corresponding to intensity. An analog-to-digital (A/D) converter convert the analog signal into pixels. The CLSM image of a sample is made by the photomultiplier and accompanying electronics, using the emission photon signals, hence it does not exists as a real image to be seen by the microscope eyepieces [139]–[141].

6.2 Visualization of GO flakes using CLSM

For my CLSM measurements, I had the opportunity to employ a NIKON A1R+ laser scanning fluorescence confocal system with a 60x high numerical aperture water immersion objective. The confocal system was an inverted microscope, and samples were illuminated by the source beam from bottom surface. The system was operated in ambient air and for clean samples does not need any sample preparation. The system allowed me to use 300 μm cells, with thin glass substrates having 160 μm thickness, to scan the whole space inside the cells. I normally used 500 nm steps in z direction, to scan the gap distance between two glass substrates. For processing the captured CLSM images, I used NIS-Elements Advanced Research software, which is a powerful software for advanced analysis of CLSM images.

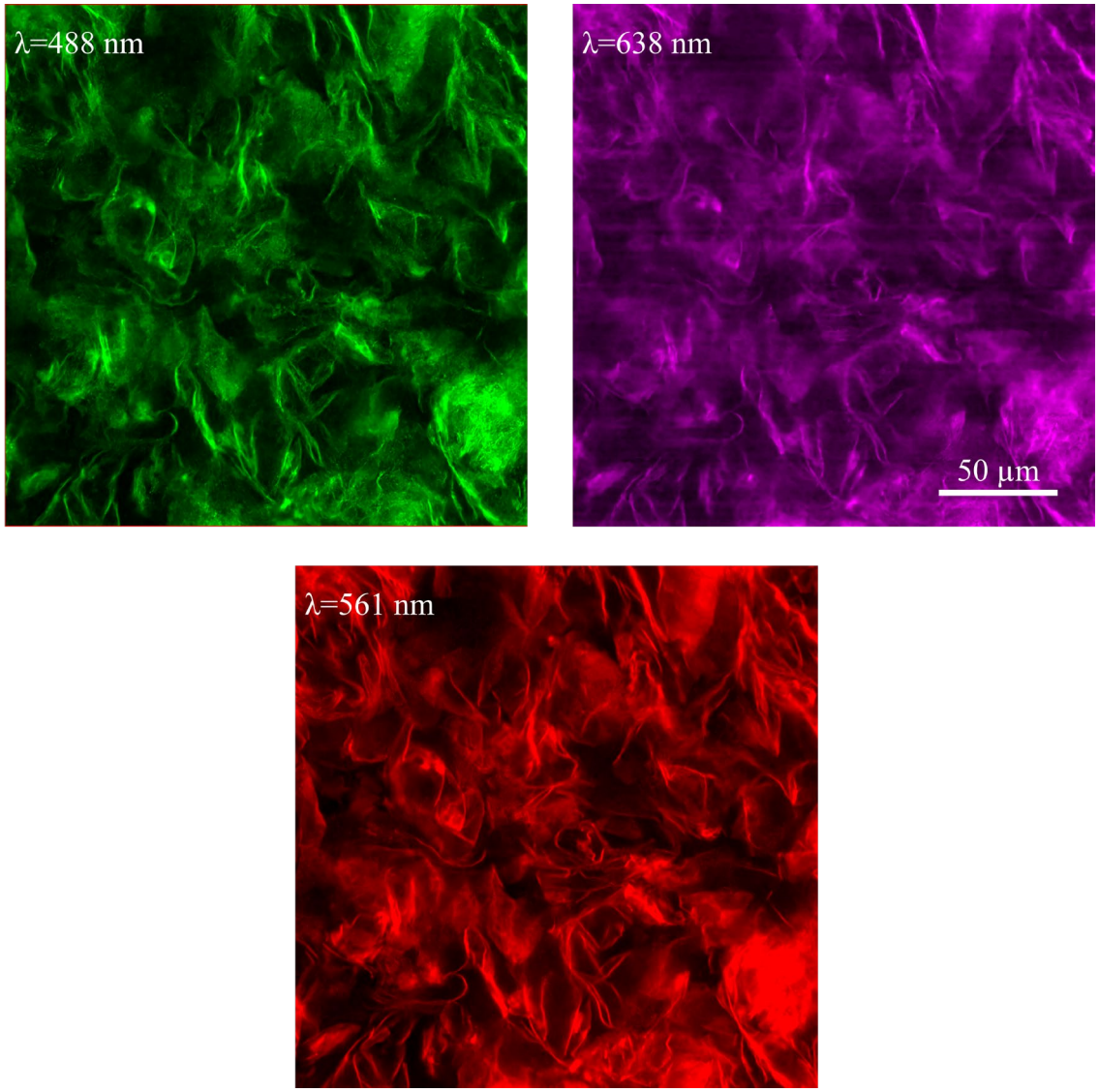

Figure 6-4. CLSM images of GO flakes using different exaction wavelengths, in 300 µm cell filled with 1 mg/mL GO suspension

For GO flakes, functional groups, lateral size, localized domains, and strain in flakes can change the electronic energy structures and result in shifts in the fluorescence peak position, band, and shape [142]. The fluorescence peak position is redshifted to longer wavelengths once the excitation wavelength is raised from λ = 325 to 650 nm [143]. Hence, for excitation source, initially I used lasers with wavelength of 488, 561, 638 nm. Figure 6-4 shows captured images of same GO flakes using different excitation wavelengths, in a 300 µm filled with 1 mg/mL GO suspension. I found that CLSM images by 561 nm laser have much better resolution, in

comparison with other wavelengths, since using 561 nm as the excitation wavelength results in a stronger emitted fluorescence light from GO flakes. Therefore, for rest of my CLSM measurements I used a 561nm laser as the excitation source and the emission was collected in the spectral region of 570 to 620 nm.

6.3 Effect of GO suspensions concentration on flakes assembly

To study GO flakes assembly in their aqueous suspensions, I used suspension with different concentrations. In very diluted suspensions, for example 0.02 mg/mL, GO flakes do not have an order and they are randomly oriented in different directions since they do not feel each other at a long distance. Over time GO flakes sediment the sedimented flakes are not flat but they have an in-plane alignment to bottom surface and they are curved, Figure 6-5.

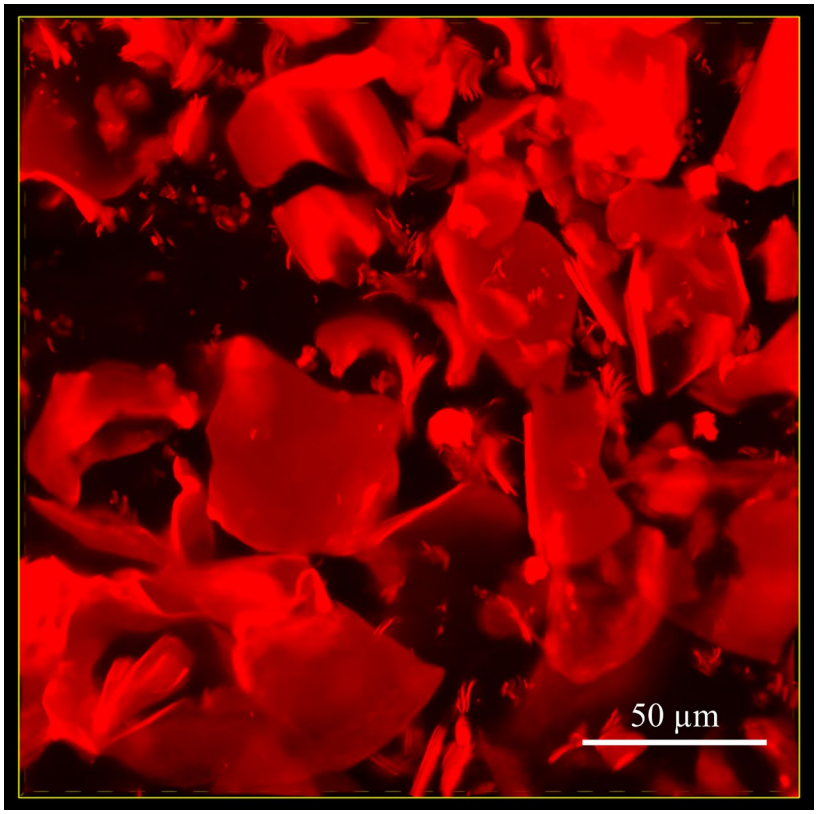

Figure 6-5. CLSM images of GO flakes in 0.02 mg/mL GO suspension

Figure 6-6 shows a 3D CLSM image of sedimented GO flakes from a low suspension concentration, 0.2 mg/mL, on bottom glass substrate of a 300 µm cell, after one day. For low concentrations in biphasic part of GO flakes phase diagram, I observed that the sedimentation of GO flakes, i.e. nematic phase happens faster in confined space of cells comparing to vials. The sedimented GO flakes are curved, not completely flat, but they have a level of planer alignment to the bottom surface because of their disk shape. This assembly of GO flakes in the sedimented nematic phase is the reason why the overtime separated bottom phases in vials, during my phase separation studies (chapter 2), are more birefringence than their fresh made suspensions. Because well dispersed GO flakes in a low concentration suspension avoid any interaction with each other, and they do not have any order.

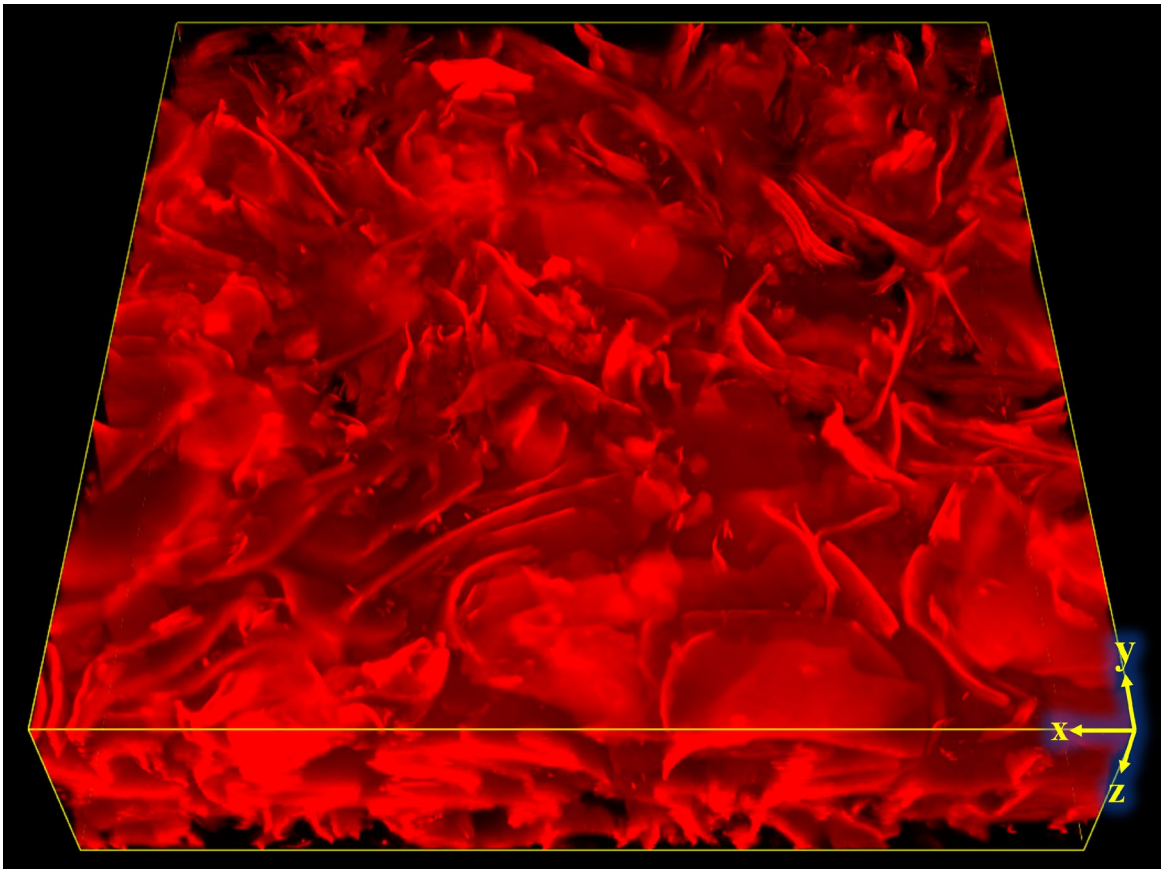

Figure 6-6. 3D CLSM image of sedimented GO flakes from 0.2 mg/mL suspension, after one day. The image has 211.65 µm size in x and y dimensions.

By increasing the concentration, the sedimentation of GO flakes gets slower, and I could perform CLSM measurements at the center of a 300 cell i.e., at a space with equal distance from two glass substrates and two side electrode walls, where GO flakes feel less the effect of the surfaces. Figure 6-7 shows GO flakes in 0.5 mg/mL biphasic suspension after one day and they are not sedimented. This agrees with my phase separation studies indicating that 0.5 mg/mL is the equilibrium concentration for having LC phase at first 20 days. In the image, although GO flakes do not have a noticeable order, their alignment is not just planer but to some extent vertical too.

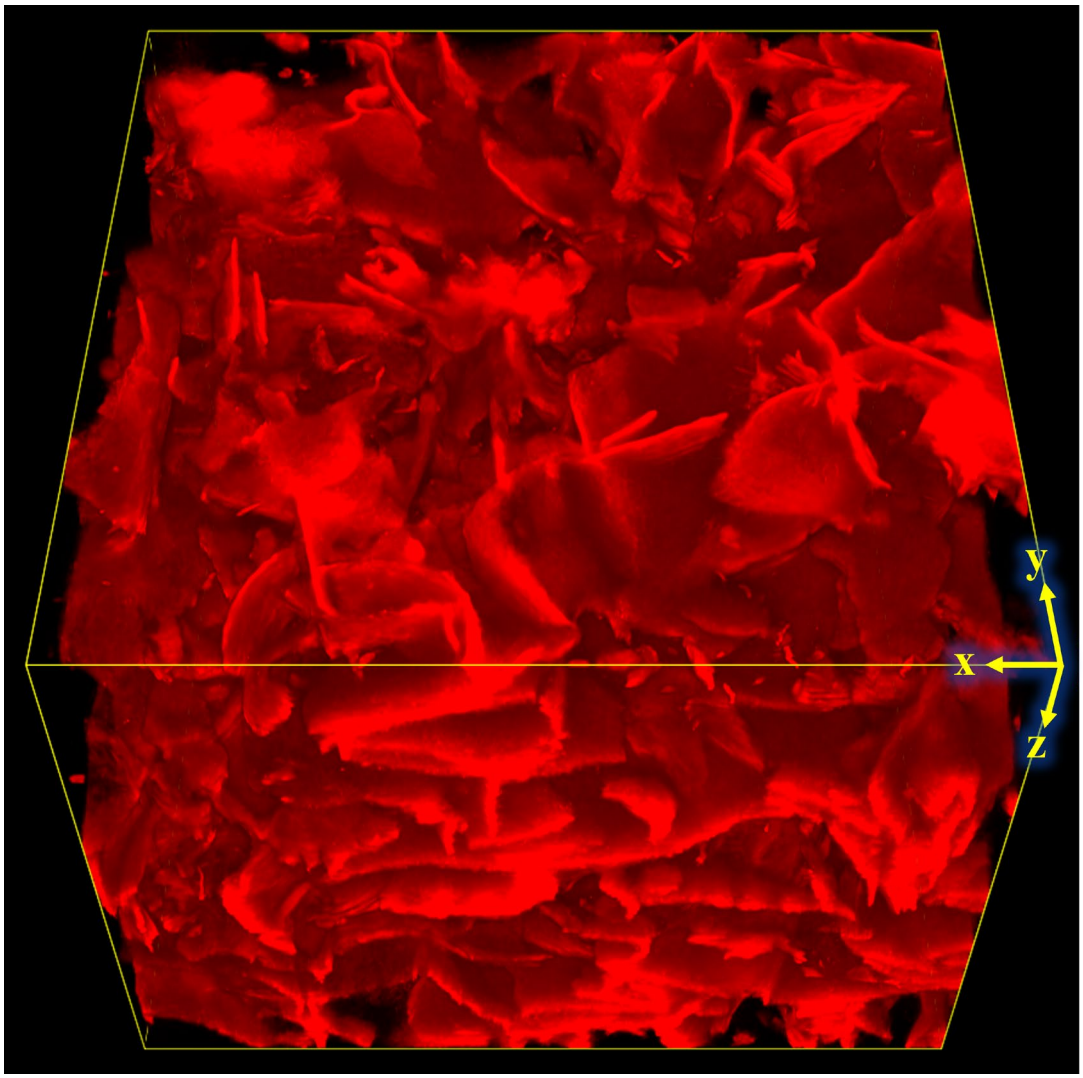

Figure 6-7. A 3D CLSM image of GO flakes in 0.5 mg/mL suspension, at the center of a 300 µm cell. The image has 211.65 µm size in x and y dimensions.

In the 0.7 mg/mL suspension being the critical concentration for having pure nematic phase, GO flakes come enough close to each other to form an order as a result of their large excluded volume, Figure 6-8. However, not all GO flakes have a vertical alignment in whole cell, but small areas with different orientations. This is the reason that 0.7 mg/mL suspension looks dark between crossed polarizers.

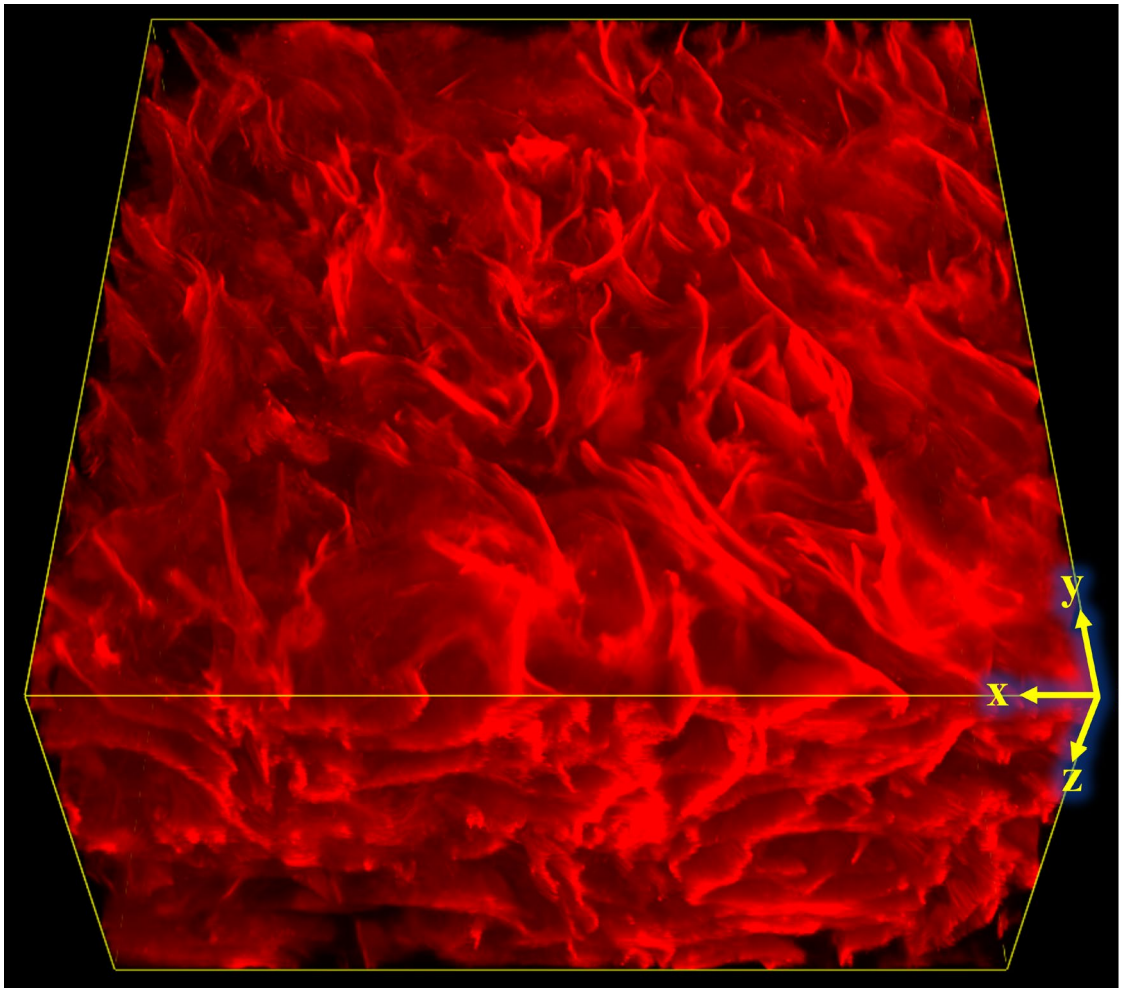

Figure 6-8. A 3D CLSM image of GO flakes in the critical concentration for having pure nematic phase, 0.7 mg/mL suspension, at the center of a 300 µm cell. The image has 211.65 µm size in x and y dimensions.

For 1 mg/mL suspension, Figure 6-9, vertical alignment of GO flakes is evident. Hence higher transmitted light intensity was measured for 1 mg/mL suspension in comparison with 0.5 and

0.7 mg/mL suspension. However, GO flakes with same orientation still do not form a large monodomain.

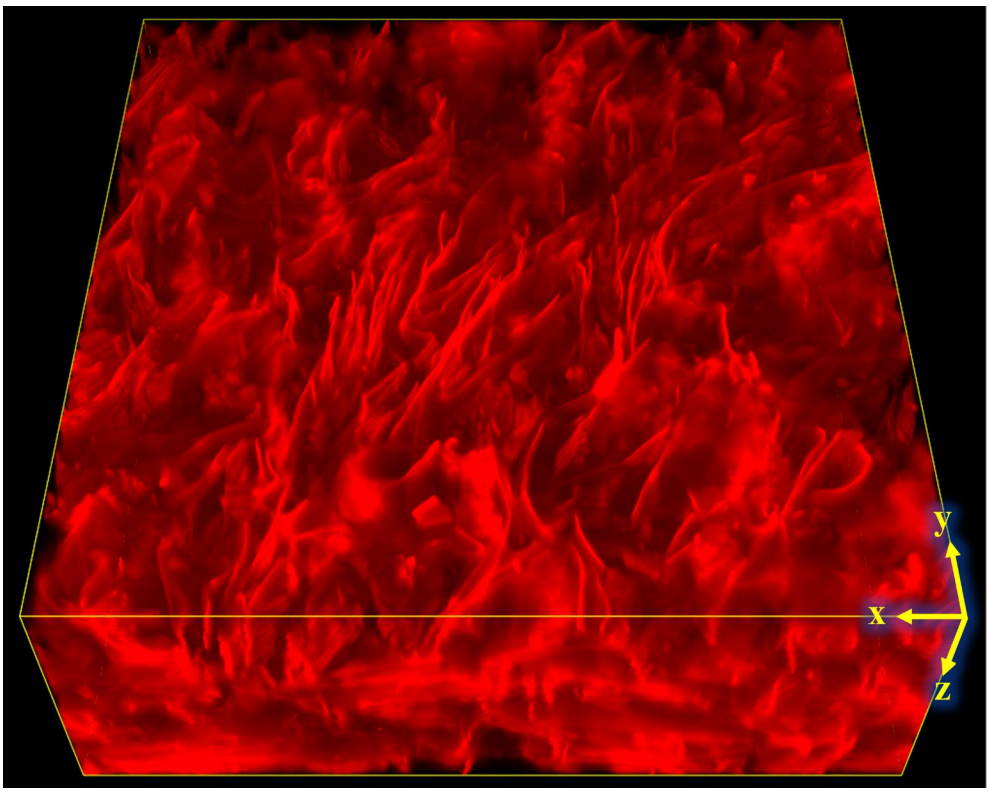

Figure 6-9. 3D CLSM image of GO flakes in 1 mg/mL suspension, at the center of a 300 µm cell. The image has 211.65 µm size in x and y dimensions

Only in 2 mg/mL suspension, Figure 6-10, GO flakes form large domains in scale of 100×100 μm^2 with a preferred orientation direction. In the image, it is visible that GO flakes have an average orientation toward the "y" direction i.e., perpendicular to electrode direction ("x" direction), in agreement with the POM and SAXS measurements. In addition, the vertical alignment of GO flakes is more pronounced resulting in higher transmitted light between crossed polarizers. Nevertheless, as the POM images revealed, even the 2 mg/mL suspension is dark in 300 µm cell between crossed polarizers in comparison with 3 mm cell. It is due to the large particle size of GO flakes. Confined large GO flakes, in a 300 µm cell that one of its

dimensions is just few times larger than the lateral size of flakes, cannot have an extended orientational order in a large area and their assembly is strongly depended on the cell dimension. On the other hand, for calculating the GO flakes average size particle using SEM images, I considered all size particles. However in Figure 6-7 to Figure 6-10, it is clear that the GO flakes assembly is strongly under influence of larger flakes (>50 µm) that generate excluded volume for smaller flakes, and they rule the behaviors of GO flakes [138]. Hence, the 300 µm gap distance in the cell is small for large GO flakes to freely have an extended orientational order, and instead they form small domains with different orientations. This is what also my transmitted light intensity measurements between crossed polarizers revealed when I rotated the cell. I found that for 2 mg/mL suspension, the ratio between maximum and minimum transmitted light intensity, at different angle, is low.

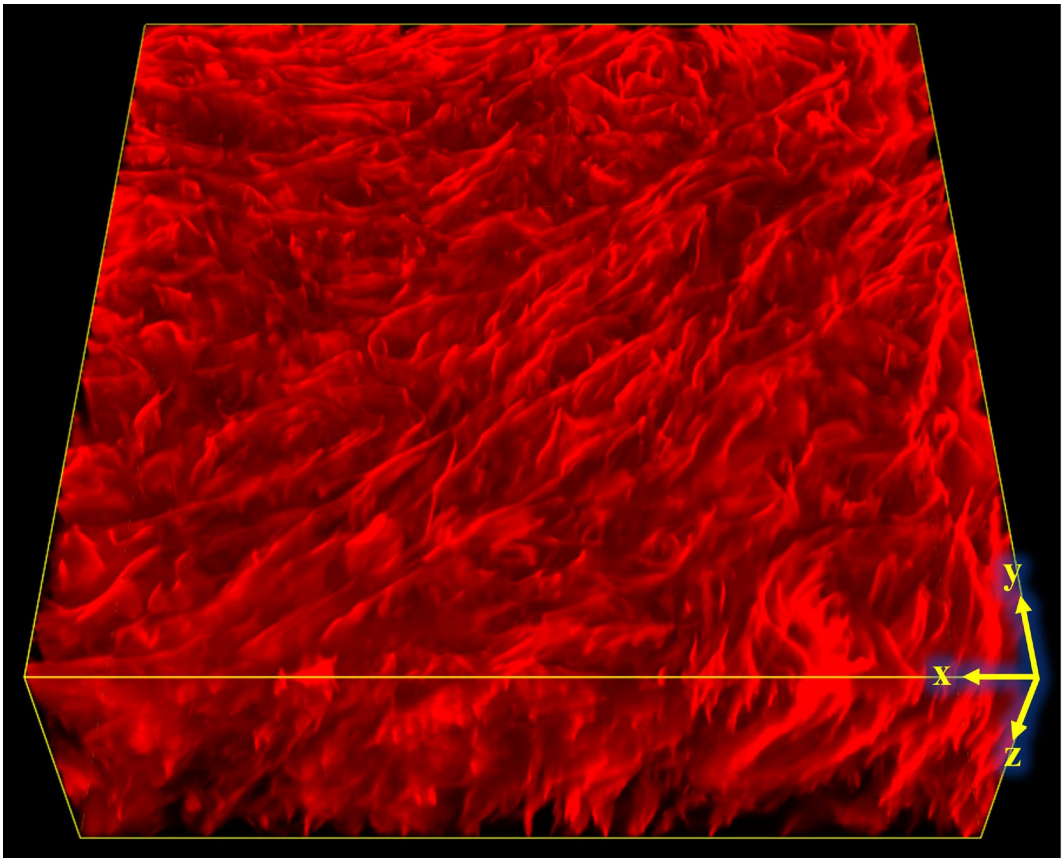

Figure 6-10. 3D CLSM image of GO flakes in 2 mg/mL suspension, at the center of a 300 µm cell. The image has 211.65 µm size in x and y dimensions.

6.4 Resolving GO flakes assembly in bulk

Using POM and synchrotron SAXS, I could successfully determine the orientational order of GO flakes in the plane of my cell, x-y plane. However, what my POM and SAXS measurements revealed were the average of GO flakes orientations in z direction, depending on their distance from side electrodes. My CLSM measurements remarkably revealed that GO flakes actually have also different alignment depending on their distance from top and bottom glass substrates.

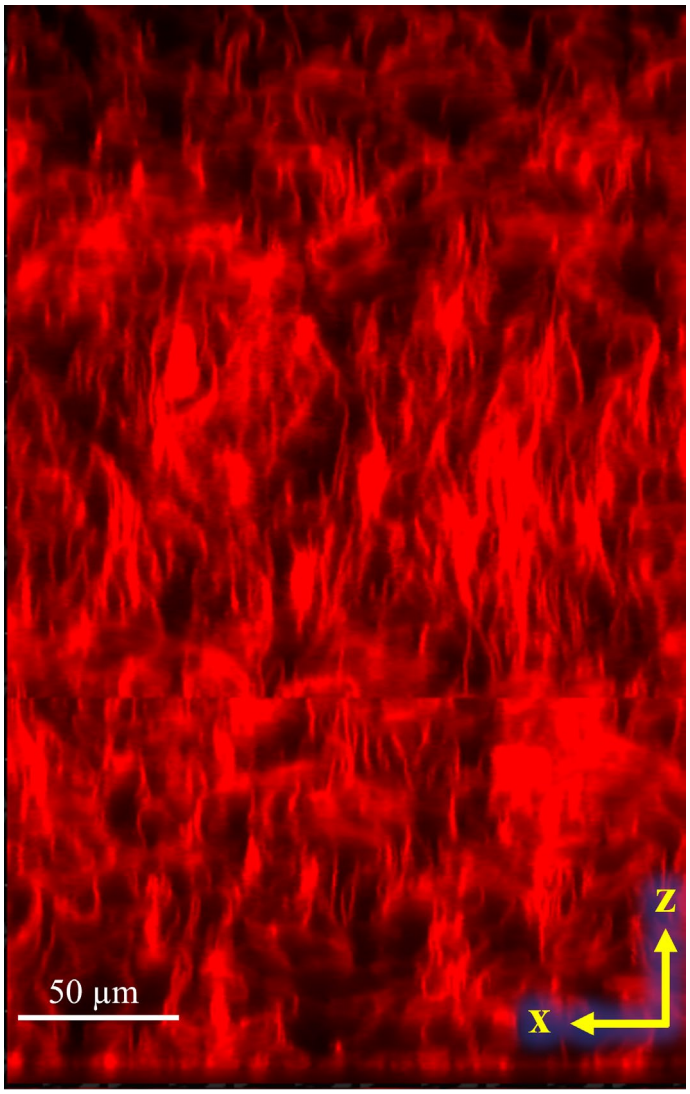

Figure 6-11. CLSM images of GO flakes self-assembly in 2 mg/mL suspension, at an equal distance between electrodes in a 300 µm cell: showing the whole cell gap distance between two glass substrates.

Figure 6-11 shows a view of GO flakes alignments in bulk, z direction. The 2D image was not obtained by scanning the x-z plane, it is composed of CLSM scans in x-y plane and the narrow dark areas at the top and bottom indicate the glass substrates. In the image the different orientation of GO flakes, at the center of cell and near to the glass substrates, are obvious. Close to the glass substrates, as a result of induced shear field at the surfaces during filling the cell, GO flakes have a planer alignment [113], [120]. GO flakes alignment at 2 μm distance from top glass surface are displayed in Figure 6-12a. In the image, GO flakes are not completely flat but curved.

At a slightly longer distance from the glass substrates, I observed a decreasing of the GO flakes planer alignment already at 5 μm distance, Figure 6-12b. This indicates that the shear force act only in a short distance from the surfaces to align GO flakes planer to them. At longer distances from top and bottom surfaces, when GO flakes feel less the surface field effect and have more freedom, they rotate to have a vertical alignment. Figure 6-12c shows GO flakes order at 30 μm distance from bottom glass substrate and the emerge of GO flakes vertical alignment is noticeable.

The preferred vertical alignment of GO flakes at the center of cell is the result of their flow-induced alignment during filling the cell, having a shape of laminar follow as the SAXS measurements uncovered. Thus, the vertical alignment of GO flakes dominants in the bulk, Figure 6-12d, while the planer alignment appears close to the surface due to the surface field effect [137]. The distance that the rotation of GO flakes orientation take place, depends on the concentration and by increasing the concentration, I observed shorter transition distances.

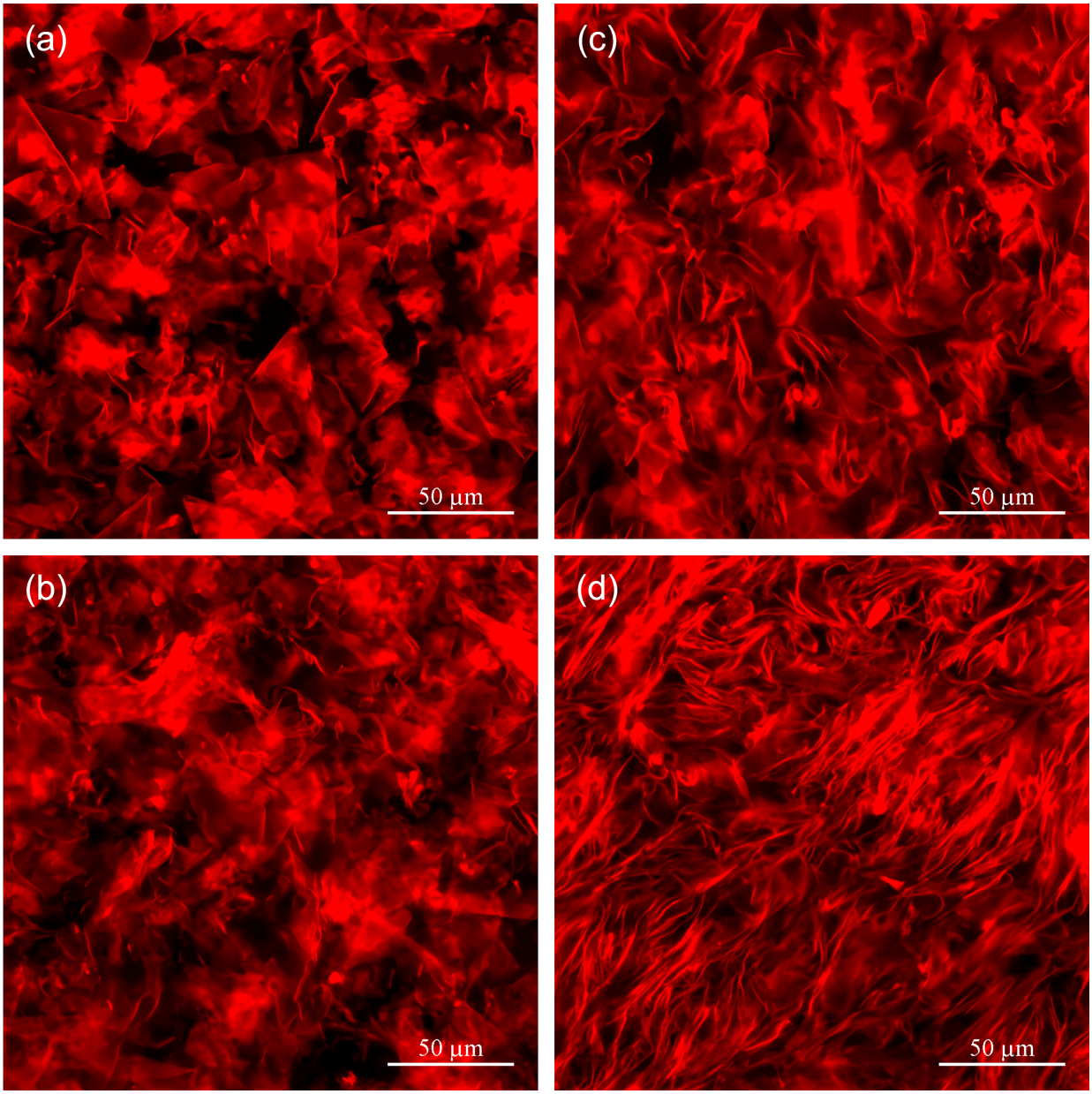

Figure 6-12. CLSM images of GO flakes in 2 mg/mL suspension, at an equal distance between electrodes in a 300 µm cell, in x-y plane at (a) 2 µm distance from top glass surface, (b) 5 µm distance from bottom glass surface, (c) 30 µm distance from bottom glass surface, (d) an equal distance between top and bottom glass substrates.

6.5 Direct visualization of GO flakes induced assembly

Figure 6-13 shows a close look at the side of cell near to an electrode. The top dark part indicates the presence of the electrode as it is not fluorescent. Just beside the electrode, GO

flakes have an obvious orientation parallel to electrode direction, in an agreement with the SAXS measurements. They look flatter and they have a higher density i.e. lower inter-flake distancing, which present response of the flakes to the higher shear force applied to the suspension at side of the cell [113]. Consequently, the GO flakes planer alignments are stable and the side of cells appears more birefringence between crossed polarizers.

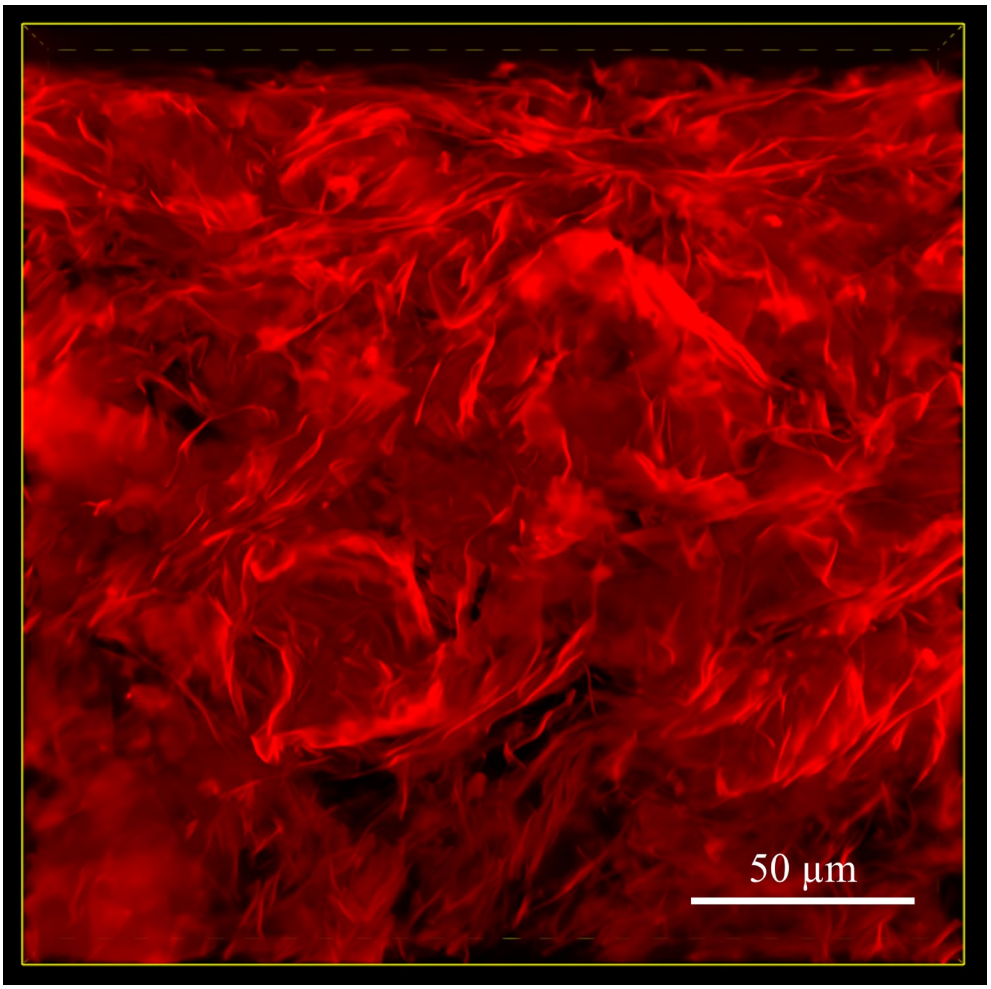

Figure 6-13. CLSM image of GO flakes in 2 mg/mL suspension, at the side of a 300 µm cell.

Contrary to the stable planar alignment of GO flakes at close distance to the cell surfaces, their vertical alignment in bulk is unstable and they easily change their orientation at the center of cell. Hence, under a low electric field as the external stimulus, GO flakes show an immediate

response and their field-induced alignment overcomes their initial order. Figure 6-14 shows GO flakes assembly in 2 mg/mL suspension after their electro-optical switching, under 7.5 volt/mm electric field.

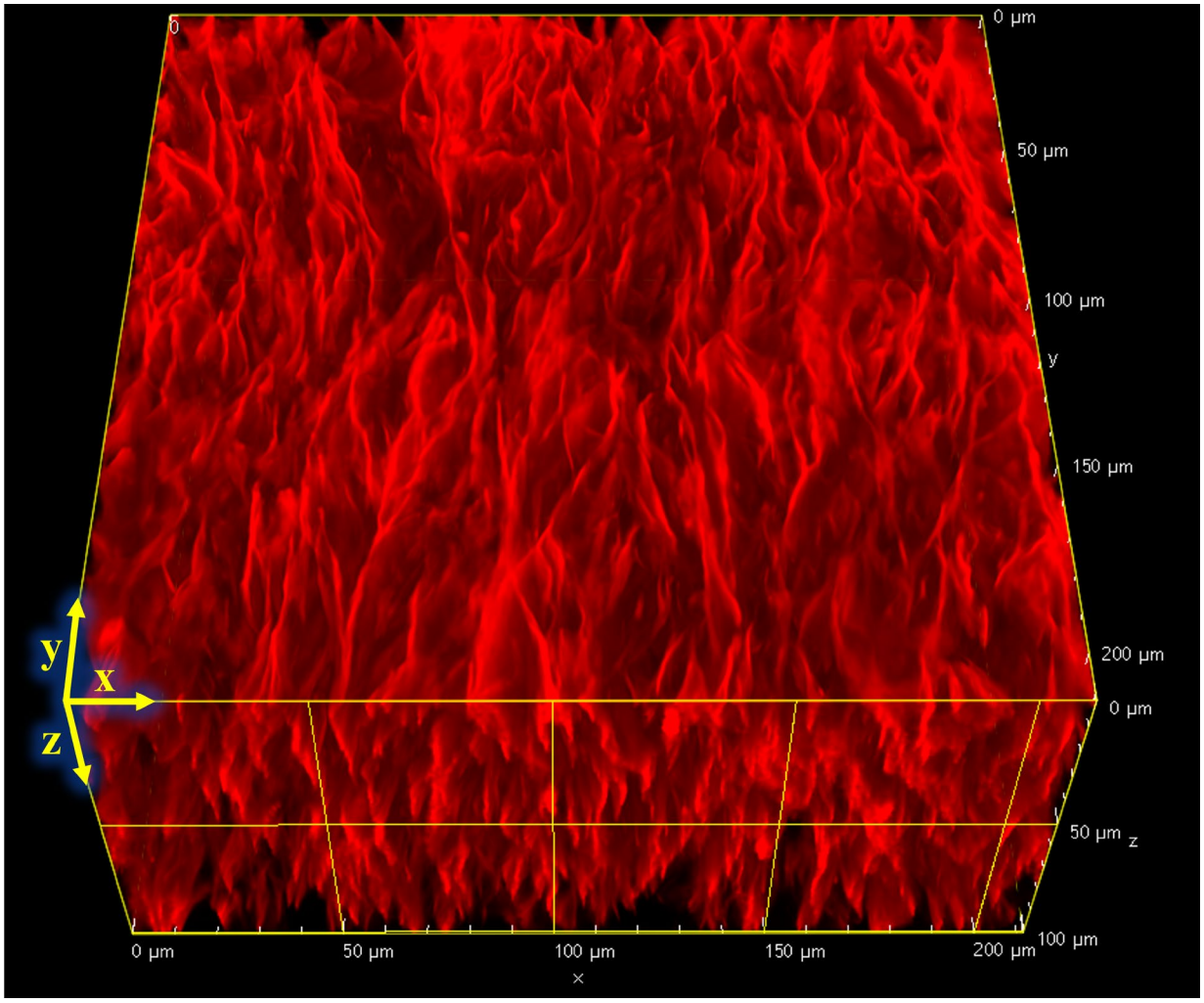

Figure 6-14. A 3D CLSM image of GO flakes under 7.5 volt/mm electric field in 2 mg/mL suspension, at the center of a 300 µm cell. The image has 211.65 µm size in x and y dimensions.

In agreement with the POM and SAXS measurements, in Figure 6-14, GO flakes have a great orientational order parallel to the electric field in y direction, which is extended through a large area in the 300 µm cell in all directions. During electro-optical switching, I observed that at the

beginning GO flakes flow in the cells in a direction opposite to direction that I filled the cells. This flow direction flattens the GO flakes assembly in the cells, having a shape of laminar flow (the SAXS measurements revealed), so GO flakes can get parallel to electric field direction. By switching off the electric field, GO flakes flow in opposite directions to reduce their free energy by gaining back their initial assembly.

Conclusion

The large GO flakes aqueous suspension is like no other colloid discotic lyotropic liquid crystal system, because of GO flakes very large aspect ratio and their superflexibility. I could show that large GO suspensions form the nematic phase at very low concentration, and without performing a size selection of large GO flakes. During the phase separation in the biphasic region of GO dispersion, I found an equilibrium concentration for GO LC phases, which depends on the time of the phase separation of the nematic phases, but not on the original concentration of GO suspension. From the observed threshold volume fraction value for having pure nematic LC phase, I calculated the thickness of dispersed GO flakes in water according to the developed Onsager's theory for solid dislike colloids, and I obtained a higher value than what was measured by AFM. My measurements demonstrated that although Onsager's theory can explain the general behaviors of solid dislike colloids particles up to some level, the theory is not fully compatible with large GO suspensions, since the theory does not consider the superflexibility and polydispersity of GO flakes.

By performing high spatial resolution CLSM, I could precisely determine the self-assembly of large GO flakes in aqueous suspension. The direct visualization of GO flakes using CLSM and my synchrotron SAXS measurements allowed me to clearly understand the behaviors of GO flakes in confined spaces like in the cells. I learned that GO flakes assembly is much more complicated than what has been understood and considered to explain the GO flake behaviors in their suspensions, including their electro-optical switching.

My CLSM measurements revealed that dispersed GO flakes are curved, and they cannot be considered as solid disk particles for their properties study. However, the large excluded

volume of large GO flakes can align super-flexible GO flakes at very low concentrations to form LC phases. In addition, even a low force like capillary flow can align super-flexible GO flakes, and when GO flakes smoothly flow on a surface, the shear force makes GO flakes have an in-plane alignment and a lower inter-flake distancing, but not completely flattened.

The high sensitivity of large GO flakes to the electric field and forming LC phase at very low concentration make GO flakes exceptionally responsive to the electric field. In contrast to previous reports, I could perform electro-optical switching of pure LC phase of large GO flakes, with a high birefringence. All my CLSM, SAXS and POM measurements confirm that large GO flakes' great electric field-induced alignment can be obtained in their LC phases, using a low electric field. These results could advance the understanding of GO assemblies under shear stress and electric field to prepare them for real-world applications.

References

[1] A. K. Geim and K. S. Novoselov, “The rise of graphene,” *Nat. Mater.*, vol. 6, no. 3, pp. 183–191, Mar. 2007, doi: 10.1038/nmat1849.

[2] A. K. Geim, “Graphene: Status and Prospects,” *Science*, vol. 324, no. 5934, pp. 1530–1534, Jun. 2009, doi: 10.1126/science.1158877.

[3] A. H. Castro Neto, F. Guinea, N. M. R. Peres, K. S. Novoselov, and A. K. Geim, “The electronic properties of graphene,” *Rev. Mod. Phys.*, vol. 81, no. 1, pp. 109–162, Jan. 2009, doi: 10.1103/RevModPhys.81.109.

[4] S. Stankovich *et al.*, “Synthesis of graphene-based nanosheets via chemical reduction of exfoliated graphite oxide,” *Carbon*, vol. 45, no. 7, pp. 1558–1565, Jun. 2007, doi: 10.1016/j.carbon.2007.02.034.

[5] A. M. Dimiev and J. M. Tour, “Mechanism of Graphene Oxide Formation,” *ACS Nano*, vol. 8, no. 3, pp. 3060–3068, Mar. 2014, doi: 10.1021/nn500606a.

[6] K. Parvez, S. Yang, X. Feng, and K. Müllen, “Exfoliation of graphene via wet chemical routes,” *Synth. Met.*, vol. 210, pp. 123–132, Dec. 2015, doi: 10.1016/j.synthmet.2015.07.014.

[7] R. Narayan, J. E. Kim, J. Y. Kim, K. E. Lee, and S. O. Kim, “Graphene Oxide Liquid Crystals: Discovery, Evolution and Applications,” *Adv. Mater.*, vol. 28, no. 16, pp. 3045–3068, 2016, doi: https://doi.org/10.1002/adma.201505122.

[8] Y. Liu, Z. Xu, W. Gao, Z. Cheng, and C. Gao, “Graphene and Other 2D Colloids: Liquid Crystals and Macroscopic Fibers,” *Adv. Mater.*, vol. 29, no. 14, p. 1606794, 2017, doi: https://doi.org/10.1002/adma.201606794.

[9] S. P. Sasikala *et al.*, “Graphene oxide liquid crystals: a frontier 2D soft material for graphene-based functional materials,” *Chem. Soc. Rev.*, vol. 47, no. 16, pp. 6013–6045, Aug. 2018, doi: 10.1039/C8CS00299A.

[10] L. Onsager, “The Effects of Shape on the Interaction of Colloidal Particles,” *Ann. N. Y. Acad. Sci.*, vol. 51, no. 4, pp. 627–659, 1949, doi: 10.1111/j.1749-6632.1949.tb27296.x.

[11] M. A. Bates and D. Frenkel, “Nematic–isotropic transition in polydisperse systems of infinitely thin hard platelets,” *J. Chem. Phys.*, vol. 110, no. 13, pp. 6553–6559, Mar. 1999, doi: 10.1063/1.478558.

[12] J. E. Kim *et al.*, “Graphene Oxide Liquid Crystals,” *Angew. Chem.*, vol. 123, no. 13, pp. 3099–3103, 2011, doi: https://doi.org/10.1002/ange.201004692.

[13] Z. Xu and C. Gao, “Aqueous Liquid Crystals of Graphene Oxide,” *ACS Nano*, vol. 5, no. 4, pp. 2908–2915, Apr. 2011, doi: 10.1021/nn200069w.

[14] B. Dan *et al.*, “Liquid crystals of aqueous, giant graphene oxide flakes,” *Soft Matter*, vol. 7, no. 23, pp. 11154–11159, Nov. 2011, doi: 10.1039/C1SM06418E.

[15] B. Konkena and S. Vasudevan, “Glass, Gel, and Liquid Crystals: Arrested States of Graphene Oxide Aqueous Dispersions,” *J. Phys. Chem. C*, vol. 118, no. 37, pp. 21706–21713, Sep. 2014, doi: 10.1021/jp507266t.

[16] K. E. Lee *et al.*, “Liquid crystal size selection of large-size graphene oxide for size-dependent N-doping and oxygen reduction catalysis,” *ACS Nano*, vol. 8, no. 9, pp. 9073–9080, Sep. 2014, doi: 10.1021/nn5024544.

[17] M. A. Pirlar *et al.*, “Light scattering through the graphene oxide liquid crystal in a micro-channel,” *Opt. Express*, vol. 27, no. 17, pp. 23864–23874, Aug. 2019, doi: 10.1364/OE.27.023864.

[18] T. M. McCoy, G. Turpin, B. M. Teo, and R. F. Tabor, “Graphene oxide: a surfactant or particle?,” *Curr. Opin. Colloid Interface Sci.*, vol. 39, pp. 98–109, Feb. 2019, doi: 10.1016/j.cocis.2019.01.010.

[19] T.-Z. Shen, S.-H. Hong, and J.-K. Song, “Electro-optical switching of graphene oxide liquid crystals with an extremely large Kerr coefficient,” *Nat. Mater.*, vol. 13, no. 4, Art. no. 4, Apr. 2014, doi: 10.1038/nmat3888.

[20] R. T. M. Ahmad, T.-Z. Shen, A. R. Masud, T. K. Ekanayaka, B. Lee, and J.-K. Song, “Guided Electro-Optical Switching of Small Graphene Oxide Particles by Larger Ones in Aqueous Dispersion,” *Langmuir*, vol. 32, no. 50, pp. 13458–13463, Dec. 2016, doi: 10.1021/acs.langmuir.6b03460.

[21] S.-H. Hong, T.-Z. Shen, and J.-K. Song, “Manipulation of structural color reflection in graphene oxide dispersions using electric fields,” *Opt. Express*, vol. 23, no. 15, pp. 18969–18974, Jul. 2015, doi: 10.1364/OE.23.018969.

[22] R. T. M. Ahmad, S.-H. Hong, T.-Z. Shen, and J.-K. Song, “Optimization of particle size for high birefringence and fast switching time in electro-optical switching of graphene oxide dispersions,” *Opt. Express*, vol. 23, no. 4, pp. 4435–4440, Feb. 2015, doi: 10.1364/OE.23.004435.

[23] S. Shahini, S. Campidelli, and G. Scalia, “Large Graphene Oxide Flakes: From Isotopic to Nematic Liquid Crystal Phase Transition,” *Phys. Status Solidi B*, vol. 256, no. 12, p. 1900411, 2019, doi: https://doi.org/10.1002/pssb.201900411.

[24] S.-H. Hong, T.-Z. Shen, and J.-K. Song, “Electro-optical Characteristics of Aqueous Graphene Oxide Dispersion Depending on Ion Concentration,” *J. Phys. Chem. C*, vol. 118, no. 45, pp. 26304–26312, Nov. 2014, doi: 10.1021/jp504892s.

[25] Y. Jiang, Y. Wang, Z. Xu, and C. Gao, “Conformation Engineering of Two-Dimensional Macromolecules: A Case Study with Graphene Oxide,” *Acc. Mater. Res.*, vol. 1, no. 3, pp. 175–187, Dec. 2020, doi: 10.1021/accountsmr.0c00027.

[26] Z. Yuan, X. Xiao, J. Li, Z. Zhao, D. Yu, and Q. Li, “Self-Assembled Graphene-Based Architectures and Their Applications,” *Adv. Sci.*, vol. 5, no. 2, p. 1700626, 2018, doi: https://doi.org/10.1002/advs.201700626.

[27] B. Senyuk *et al.*, “Nonlinear Photoluminescence Imaging of Isotropic and Liquid Crystalline Dispersions of Graphene Oxide,” *ACS Nano*, vol. 6, no. 9, pp. 8060–8066, Sep. 2012, doi: 10.1021/nn302644r.

[28] H. Ham *et al.*, “Freeze-drying-induced changes in the properties of graphene oxides,” *Nanotechnology*, vol. 25, no. 23, p. 235601, May 2014, doi: 10.1088/0957-4484/25/23/235601.

[29] T.-Z. Shen, S.-H. Hong, B. Lee, and J.-K. Song, “Bottom-up and top-down manipulations for multi-order photonic crystallinity in a graphene-oxide colloid,” *NPG Asia Mater.*, vol. 8, no. 8, Art. no. 8, Aug. 2016, doi: 10.1038/am.2016.110.

[30] Y. Liu, Z. Xu, W. Gao, Z. Cheng, and C. Gao, “Graphene and Other 2D Colloids: Liquid Crystals and Macroscopic Fibers,” *Adv. Mater.*, vol. 29, no. 14, p. 1606794, 2017, doi: 10.1002/adma.201606794.

[31] D. R. Dreyer, S. Park, C. W. Bielawski, and R. S. Ruoff, “The chemistry of graphene oxide,” *Chem. Soc. Rev.*, vol. 39, no. 1, pp. 228–240, Dec. 2009, doi: 10.1039/B917103G.

[32] S. Eigler and A. Hirsch, “Chemistry with Graphene and Graphene Oxide—Challenges for Synthetic Chemists,” *Angew. Chem. Int. Ed.*, vol. 53, no. 30, pp. 7720–7738, 2014, doi: 10.1002/anie.201402780.

[33] B. C. Brodie, “XIII. On the atomic weight of graphite,” *Philos. Trans. R. Soc. Lond.*, vol. 149, pp. 249–259, Jan. 1859, doi: 10.1098/rstl.1859.0013.

[34] S. Stankovich *et al.*, “Graphene-based composite materials,” *Nature*, vol. 442, no. 7100, pp. 282–286, Jul. 2006, doi: 10.1038/nature04969.

[35] D. A. Dikin *et al.*, “Preparation and characterization of graphene oxide paper,” *Nature*, vol. 448, no. 7152, pp. 457–460, Jul. 2007, doi: 10.1038/nature06016.

[36] S. Stankovich *et al.*, “Synthesis of graphene-based nanosheets via chemical reduction of exfoliated graphite oxide,” *Carbon*, vol. 45, no. 7, pp. 1558–1565, Jun. 2007, doi: 10.1016/j.carbon.2007.02.034.

[37] C. K. Chua and M. Pumera, “Chemical reduction of graphene oxide: a synthetic chemistry viewpoint,” *Chem. Soc. Rev.*, vol. 43, no. 1, pp. 291–312, Dec. 2013, doi: 10.1039/C3CS60303B.

[38] Z. Wang *et al.*, “Aqueous phase preparation of graphene with low defect density and adjustable layers,” *Chem. Commun.*, vol. 49, no. 92, pp. 10835–10837, Oct. 2013, doi: 10.1039/C3CC46809G.

[39] X.-Y. Wang, A. Narita, and K. Müllen, “Precision synthesis versus bulk-scale fabrication of graphenes,” *Nat. Rev. Chem.*, vol. 2, no. 1, pp. 1–10, Dec. 2017, doi: 10.1038/s41570-017-0100.

[40] A. T. Smith, A. M. LaChance, S. Zeng, B. Liu, and L. Sun, “Synthesis, properties, and applications of graphene oxide/reduced graphene oxide and their nanocomposites,” *Nano Mater. Sci.*, vol. 1, no. 1, pp. 31–47, Mar. 2019, doi: 10.1016/j.nanoms.2019.02.004.

[41] A. T. Dideikin and A. Y. Vul’, “Graphene Oxide and Derivatives: The Place in Graphene Family,” *Front. Phys.*, vol. 6, p. 149, 2019, doi: 10.3389/fphy.2018.00149.

[42] W. S. Hummers and R. E. Offeman, “Preparation of Graphitic Oxide,” *J. Am. Chem. Soc.*, vol. 80, no. 6, pp. 1339–1339, Mar. 1958, doi: 10.1021/ja01539a017.

[43] N. I. Kovtyukhova *et al.*, “Layer-by-Layer Assembly of Ultrathin Composite Films from Micron-Sized Graphite Oxide Sheets and Polycations,” *Chem. Mater.*, vol. 11, no. 3, pp. 771–778, Mar. 1999, doi: 10.1021/cm981085u.

[44] D. C. Marcano *et al.*, “Improved Synthesis of Graphene Oxide,” *ACS Nano*, vol. 4, no. 8, pp. 4806–4814, Aug. 2010, doi: 10.1021/nn1006368.

[45] J. Zhao, S. Pei, W. Ren, L. Gao, and H.-M. Cheng, “Efficient Preparation of Large-Area Graphene Oxide Sheets for Transparent Conductive Films,” *ACS Nano*, vol. 4, no. 9, pp. 5245–5252, Sep. 2010, doi: 10.1021/nn1015506.

[46] T. Soltani and B.-K. Lee, “Low intensity-ultrasonic irradiation for highly efficient, eco-friendly and fast synthesis of graphene oxide,” *Ultrason. Sonochem.*, vol. 38, pp. 693–703, Sep. 2017, doi: 10.1016/j.ultsonch.2016.08.010.

[47] A. M. Dimiev and J. M. Tour, “Mechanism of Graphene Oxide Formation,” *ACS Nano*, vol. 8, no. 3, pp. 3060–3068, Mar. 2014, doi: 10.1021/nn500606a.

[48] E. M. Deemer *et al.*, “Consequence of oxidation method on graphene oxide produced with different size graphite precursors,” *Mater. Sci. Eng. B*, vol. 224, pp. 150–157, Oct. 2017, doi: 10.1016/j.mseb.2017.07.018.

[49] L. Zhang, J. Liang, Y. Huang, Y. Ma, Y. Wang, and Y. Chen, “Size-controlled synthesis of graphene oxide sheets on a large scale using chemical exfoliation,” *Carbon*, vol. 47, no. 14, pp. 3365–3368, Nov. 2009, doi: 10.1016/j.carbon.2009.07.045.

[50] H. He, J. Klinowski, M. Forster, and A. Lerf, “A new structural model for graphite oxide,” *Chem. Phys. Lett.*, vol. 287, no. 1, pp. 53–56, Apr. 1998, doi: 10.1016/S0009-2614(98)00144-4.

[51] A. Lerf, H. He, M. Forster, and J. Klinowski, “Structure of Graphite Oxide Revisited,” *J. Phys. Chem. B*, vol. 102, no. 23, pp. 4477–4482, Jun. 1998, doi: 10.1021/jp9731821.

[52] K. Erickson, R. Erni, Z. Lee, N. Alem, W. Gannett, and A. Zettl, “Determination of the Local Chemical Structure of Graphene Oxide and Reduced Graphene Oxide,” *Adv. Mater.*, vol. 22, no. 40, pp. 4467–4472, 2010, doi: 10.1002/adma.201000732.

[53] T. M. McCoy, G. Turpin, B. M. Teo, and R. F. Tabor, “Graphene oxide: a surfactant or particle?,” *Curr. Opin. Colloid Interface Sci.*, vol. 39, pp. 98–109, Feb. 2019, doi: 10.1016/j.cocis.2019.01.010.

[54] J. Kim, L. J. Cote, and J. Huang, “Two dimensional soft material: new faces of graphene oxide,” *Acc. Chem. Res.*, vol. 45, no. 8, pp. 1356–1364, Aug. 2012, doi: 10.1021/ar300047s.

[55] J. Kim, L. J. Cote, F. Kim, W. Yuan, K. R. Shull, and J. Huang, “Graphene Oxide Sheets at Interfaces,” *J. Am. Chem. Soc.*, vol. 132, no. 23, pp. 8180–8186, Jun. 2010, doi: 10.1021/ja102777p.

[56] F. Kim, L. J. Cote, and J. Huang, “Graphene Oxide: Surface Activity and Two-Dimensional Assembly,” *Adv. Mater.*, vol. 22, no. 17, pp. 1954–1958, 2010, doi: 10.1002/adma.200903932.

[57] J. I. Paredes, S. Villar-Rodil, A. Martínez-Alonso, and J. M. D. Tascón, “Graphene Oxide Dispersions in Organic Solvents,” *Langmuir*, vol. 24, no. 19, pp. 10560–10564, Oct. 2008, doi: 10.1021/la801744a.

[58] R. Jalili *et al.*, “Organic Solvent-Based Graphene Oxide Liquid Crystals: A Facile Route toward the Next Generation of Self-Assembled Layer-by-Layer Multifunctional 3D Architectures,” *ACS Nano*, vol. 7, no. 5, pp. 3981–3990, May 2013, doi: 10.1021/nn305906z.

[59] M. M. Gudarzi, M. H. M. Moghadam, and F. Sharif, “Spontaneous exfoliation of graphite oxide in polar aprotic solvents as the route to produce graphene oxide – organic solvents liquid crystals,” *Carbon*, vol. 64, pp. 403–415, Nov. 2013, doi: 10.1016/j.carbon.2013.07.093.

[60] C.-J. Shih, S. Lin, R. Sharma, M. S. Strano, and D. Blankschtein, “Understanding the pH-Dependent Behavior of Graphene Oxide Aqueous Solutions: A Comparative Experimental and Molecular Dynamics Simulation Study,” *Langmuir*, vol. 28, no. 1, pp. 235–241, Jan. 2012, doi: 10.1021/la203607w.

[61] M. M. Gudarzi, “Colloidal Stability of Graphene Oxide: Aggregation in Two Dimensions,” *Langmuir*, vol. 32, no. 20, pp. 5058–5068, May 2016, doi: 10.1021/acs.langmuir.6b01012.

[62] X. Fan *et al.*, “Deoxygenation of Exfoliated Graphite Oxide under Alkaline Conditions: A Green Route to Graphene Preparation,” *Adv. Mater.*, vol. 20, no. 23, pp. 4490–4493, 2008, doi: 10.1002/adma.200801306.

[63] F. Reinitzer, “Beiträge zur Kenntniss des Cholesterins,” *Monatshefte Für Chem. Verwandte Teile Anderer Wiss.*, vol. 9, no. 1, pp. 421–441, Dec. 1888, doi: 10.1007/BF01516710.

[64] S. Ermakov, A. Beletskii, O. Eismont, and Vi. Nikolaev, *Liquid crystals in biotribology: synovial joint treatment*. Springer, 2016.

[65] G. Brown, *Liquid Crystals and Biological Structures*. Elsevier, 2012.

[66] M. Hird, “Fluorinated liquid crystals – properties and applications,” *Chem. Soc. Rev.*, vol. 36, no. 12, pp. 2070–2095, Nov. 2007, doi: 10.1039/B610738A.

[67] S. Chandrasekhar, “Discotic liquid crystals. A brief review,” *Liq. Cryst.*, vol. 14, no. 1, pp. 3–14, Jan. 1993, doi: 10.1080/02678299308027301.

[68] N. A. Platé, *Liquid-Crystal Polymers*. Springer Science & Business Media, 1993.

[69] H. K. Bisoyi and S. Kumar, “Liquid-crystal nanoscience: an emerging avenue of soft self-assembly,” *Chem. Soc. Rev.*, vol. 40, no. 1, pp. 306–319, Dec. 2010, doi: 10.1039/B901793N.

[70] Y. Jiang, Y. Wang, Z. Xu, and C. Gao, “Conformation Engineering of Two-Dimensional Macromolecules: A Case Study with Graphene Oxide,” *Acc. Mater. Res.*, vol. 1, no. 3, pp. 175–187, Dec. 2020, doi: 10.1021/accountsmr.0c00027.

[71] L. Onsager, “The Effects of Shape on the Interaction of Colloidal Particles,” *Ann. N. Y. Acad. Sci.*, vol. 51, no. 4, pp. 627–659, 1949, doi: 10.1111/j.1749-6632.1949.tb27296.x.

[72] R. Jalili *et al.*, “Formation and processability of liquid crystalline dispersions of graphene oxide,” *Mater. Horiz.*, vol. 1, no. 1, pp. 87–91, Nov. 2013, doi: 10.1039/C3MH00050H.

[73] A. Shundo *et al.*, “Hierarchical spatial heterogeneity in liquid crystals composed of graphene oxides,” *Phys. Chem. Chem. Phys.*, vol. 18, no. 32, pp. 22399–22406, Aug. 2016, doi: 10.1039/C6CP03614G.

[74] F. Guo, F. Kim, T. H. Han, V. B. Shenoy, J. Huang, and R. H. Hurt, “Hydration-Responsive Folding and Unfolding in Graphene Oxide Liquid Crystal Phases,” *ACS Nano*, vol. 5, no. 10, pp. 8019–8025, Oct. 2011, doi: 10.1021/nn2025644.

[75] S. H. Aboutalebi, M. M. Gudarzi, Q. B. Zheng, and J.-K. Kim, “Spontaneous Formation of Liquid Crystals in Ultralarge Graphene Oxide Dispersions,” *Adv. Funct. Mater.*, vol. 21, no. 15, pp. 2978–2988, 2011, doi: 10.1002/adfm.201100448.

[76] Z. Xu and C. Gao, “Graphene chiral liquid crystals and macroscopic assembled fibres,” *Nat. Commun.*, vol. 2, no. 1, p. 571, Dec. 2011, doi: 10.1038/ncomms1583.

[77] David J.R. Cristaldi, Salvatore Pennisi, and Francesco Pulvirenti, *Liquid Crystal Display Drivers - Techniques and Circuits*. Springer, Dordrecht, 2009.

[78] S. Singh and D. Dunmur, *Liquid crystals: fundamentals*. Singapore; New Jersey: World Scientific, 2002. [Online]. Available: http://public.ebookcentral.proquest.com/choice/publicfullrecord.aspx?p=1681302

[79] I. Dierking, *Textures of Liquid Crystals*, 1st ed. Wiley-VCH Verlag GmbH & Co. KGaA, 2003. doi: 10.1002/3527602054.

[80] Douglas B. Murphy, Kenneth R. Spring, Thomas J. Fellers, and Michael W. Davidson, “Principles of Birefringence,” *Nikon’s MicroscopyU*. https://www.microscopyu.com/techniques/polarized-light/principles-of-birefringence

[81] I. Langmuir, “The Role of Attractive and Repulsive Forces in the Formation of Tactoids, Thixotropic Gels, Protein Crystals and Coacervates,” *J. Chem. Phys.*, vol. 6, no. 12, pp. 873–896, Dec. 1938, doi: 10.1063/1.1750183.

[82] B. Konkena and S. Vasudevan, “Glass, Gel, and Liquid Crystals: Arrested States of Graphene Oxide Aqueous Dispersions,” *J. Phys. Chem. C*, vol. 118, no. 37, pp. 21706–21713, Sep. 2014, doi: 10.1021/jp507266t.

[83] Z. Xu and C. Gao, “Aqueous Liquid Crystals of Graphene Oxide,” *ACS Nano*, vol. 5, no. 4, pp. 2908–2915, Apr. 2011, doi: 10.1021/nn200069w.

[84] P. Poulin *et al.*, “Superflexibility of graphene oxide,” *Proc. Natl. Acad. Sci.*, vol. 113, no. 40, pp. 11088–11093, Oct. 2016, doi: 10.1073/pnas.1605121113.

[85] F. Camerel, J. C. P. Gabriel, P. Batail, P. Panine, and P. Davidson, “Combined SAXS−Rheological Studies of Liquid-Crystalline Colloidal Dispersions of Mineral Particles,” *Langmuir*, vol. 19, no. 24, pp. 10028–10035, Nov. 2003, doi: 10.1021/la034626p.

[86] A. M. Philippe *et al.*, “Rheo-SAXS investigation of shear-thinning behaviour of very anisometric repulsive disc-like clay suspensions,” *J. Phys.: Condens. Matter*, vol. 23, no. 19, p. 194112, Apr. 2011, doi: 10.1088/0953-8984/23/19/194112.

[87] M. J. Shah, D. C. Thompson, and C. M. Hart, “Reversal of Electro-Optical Birefringence in Bentonite Suspensions,” 1963, doi: 10.1021/J100800A002.

[88] I. Dozov *et al.*, "Electric-field-induced perfect anti-nematic order in isotropic aqueous suspensions of a natural beidellite clay," *J. Phys. Chem. B*, vol. 115, no. 24, pp. 7751–7765, Jun. 2011, doi: 10.1021/jp201201x.

[89] E. Paineau *et al.*, "Liquid-Crystalline Nematic Phase in Aqueous Suspensions of a Disk-Shaped Natural Beidellite Clay," *J. Phys. Chem. B*, vol. 113, no. 48, pp. 15858–15869, Dec. 2009, doi: 10.1021/jp908326y.

[90] S.-H. Hong, T.-Z. Shen, and J.-K. Song, "Electro-optical Characteristics of Aqueous Graphene Oxide Dispersion Depending on Ion Concentration," *J. Phys. Chem. C*, vol. 118, no. 45, pp. 26304–26312, Nov. 2014, doi: 10.1021/jp504892s.

[91] J. E. Kim *et al.*, "Graphene Oxide Liquid Crystals," *Angew. Chem. Int. Ed.*, vol. 50, no. 13, pp. 3043–3047, 2011, doi: 10.1002/anie.201004692.

[92] B. Li, S. Li, J. Liu, B. Wang, and S. Yang, "Vertically Aligned Sulfur–Graphene Nanowalls on Substrates for Ultrafast Lithium–Sulfur Batteries," *Nano Lett.*, vol. 15, no. 5, pp. 3073–3079, May 2015, doi: 10.1021/acs.nanolett.5b00064.

[93] Z.-S. Wu *et al.*, "Field Emission of Single-Layer Graphene Films Prepared by Electrophoretic Deposition," *Adv. Mater.*, vol. 21, no. 17, pp. 1756–1760, 2009, doi: 10.1002/adma.200802560.

[94] S. J. An *et al.*, "Thin Film Fabrication and Simultaneous Anodic Reduction of Deposited Graphene Oxide Platelets by Electrophoretic Deposition," *J. Phys. Chem. Lett.*, vol. 1, no. 8, pp. 1259–1263, Apr. 2010, doi: 10.1021/jz100080c.

[95] M. Diba, D. W. H. Fam, A. R. Boccaccini, and M. S. P. Shaffer, "Electrophoretic deposition of graphene-related materials: A review of the fundamentals," *Prog. Mater. Sci.*, vol. 82, pp. 83–117, Sep. 2016, doi: 10.1016/j.pmatsci.2016.03.002.

[96] T.-Z. Shen, S.-H. Hong, and J.-K. Song, "Electro-optical switching of graphene oxide liquid crystals with an extremely large Kerr coefficient," *Nat. Mater.*, vol. 13, no. 4, pp. 394–399, Apr. 2014, doi: 10.1038/nmat3888.

[97] J. Y. Kim and S. O. Kim, "Electric fields line up graphene oxide," *Nat. Mater.*, vol. 13, no. 4, pp. 325–326, Apr. 2014, doi: 10.1038/nmat3929.

[98] M. Kumar, A. Gowda, and S. Kumar, "Discotic Liquid Crystals with Graphene: Supramolecular Self-assembly to Applications," *Part. Part. Syst. Charact.*, vol. 34, no. 9, p. 1700003, 2017, doi: 10.1002/ppsc.201700003.

[99] J. Zhao, S. Pei, W. Ren, L. Gao, and H.-M. Cheng, "Efficient Preparation of Large-Area Graphene Oxide Sheets for Transparent Conductive Films," *ACS Nano*, vol. 4, no. 9, pp. 5245–5252, Sep. 2010, doi: 10.1021/nn1015506.

[100] J. Azevedo *et al.*, "Versatile Wafer-Scale Technique for the Formation of Ultrasmooth and Thickness-Controlled Graphene Oxide Films Based on Very Large Flakes," *ACS Appl. Mater. Interfaces*, vol. 7, no. 38, pp. 21270–21277, Sep. 2015, doi: 10.1021/acsami.5b05540.

[101] C. J. Chen, *Introduction to Scanning Tunneling Microscopy*, Second. Oxford University Press, 2007. [Online]. Available: DOI:10.1093/acprof:oso/9780199211500.001.0001

[102] P. Eaton and P. West, *Atomic force microscopy*, First. Oxford University Press, 2018. [Online]. Available: DOI:10.1093/acprof:oso/9780199570454.001.0001

[103] H. Yang, H. Li, J. Zhai, L. Sun, and H. Yu, "Simple Synthesis of Graphene Oxide Using Ultrasonic Cleaner from Expanded Graphite," *Ind. Eng. Chem. Res.*, vol. 53, no. 46, pp. 17878–17883, Nov. 2014, doi: 10.1021/ie503586v.

[104] D. C. Marcano *et al.*, "Improved Synthesis of Graphene Oxide," *ACS Nano*, vol. 4, no. 8, pp. 4806–4814, Aug. 2010, doi: 10.1021/nn1006368.

[105] S. Pei, Q. Wei, K. Huang, H.-M. Cheng, and W. Ren, "Green synthesis of graphene oxide by seconds timescale water electrolytic oxidation," *Nat. Commun.*, vol. 9, no. 1, p. 145, Jan. 2018, doi: 10.1038/s41467-017-02479-z.

[106] J. Zhang, H. Yang, G. Shen, P. Cheng, J. Zhang, and S. Guo, "Reduction of graphene oxide viaL-ascorbic acid," *Chem. Commun.*, vol. 46, no. 7, pp. 1112–1114, Feb. 2010, doi: 10.1039/B917705A.

[107] E. Stolyarova *et al.*, "High-resolution scanning tunneling microscopy imaging of mesoscopic graphene sheets on an insulating surface," *Proc. Natl. Acad. Sci.*, vol. 104, no. 22, pp. 9209–9212, May 2007, doi: 10.1073/pnas.0703337104.

[108] Y. Zhu *et al.*, "Graphene and Graphene Oxide: Synthesis, Properties, and Applications," *Adv. Mater.*, vol. 22, no. 35, pp. 3906–3924, 2010, doi: 10.1002/adma.201001068.

[109] P. P. Brisebois and M. Siaj, "Harvesting graphene oxide – years 1859 to 2019: a review of its structure, synthesis, properties and exfoliation," *J. Mater. Chem. C*, vol. 8, no. 5, pp. 1517–1547, Feb. 2020, doi: 10.1039/C9TC03251G.

[110] Y. Jin, Z. Xu, Y. Guo, and X. Yang, "Molecular-Level Recognition of Interaction Mechanism between Graphene Oxides in Solvent Media," *J. Phys. Chem. C*, vol. 122, no. 7, pp. 4063–4072, Feb. 2018, doi: 10.1021/acs.jpcc.7b12017.

[111] P. Bansal, A. S. Panwar, and D. Bahadur, "Molecular-Level Insights into the Stability of Aqueous Graphene Oxide Dispersions," *J. Phys. Chem. C*, vol. 121, no. 18, pp. 9847–9859, May 2017, doi: 10.1021/acs.jpcc.7b00464.

[112] J. Shang, L. Ma, J. Li, W. Ai, T. Yu, and G. G. Gurzadyan, "The Origin of Fluorescence from Graphene Oxide," *Sci. Rep.*, vol. 2, no. 1, p. 792, Nov. 2012, doi: 10.1038/srep00792.

[113] P. Poulin *et al.*, "Superflexibility of graphene oxide," *Proc. Natl. Acad. Sci.*, vol. 113, no. 40, pp. 11088–11093, Oct. 2016, doi: 10.1073/pnas.1605121113.

[114] F. Lin, X. Tong, Y. Wang, J. Bao, and Z. M. Wang, "Graphene oxide liquid crystals: synthesis, phase transition, rheological property, and applications in optoelectronics and display," *Nanoscale Res. Lett.*, vol. 10, no. 1, p. 435, Nov. 2015, doi: 10.1186/s11671-015-1139-1.

[115] M. Kim *et al.*, "Graphene: a new liquid crystal for high performance electro-optic applications," in *Liquid Crystals XXII*, Sep. 2018, vol. 10735, p. 107350N. doi: 10.1117/12.2501822.

[116] R. T. M. Ahmad, S.-H. Hong, T.-Z. Shen, A. R. Masud, and J.-K. Song, "Effect of solvents on the electro-optical switching of graphene oxide dispersions," *Appl. Phys. Lett.*, vol. 108, no. 25, p. 251903, Jun. 2016, doi: 10.1063/1.4954763.

[117] M. J. Kim, J. H. Park, J. Yamamoto, Y. S. Kim, and G. Scalia, "Electro-optic switching with liquid crystal graphene," *Phys. Status Solidi RRL – Rapid Res. Lett.*, vol. 10, no. 5, pp. 397–403, 2016, doi: 10.1002/pssr.201600038.

[118] "Polarized Light Microscopy - The First Order (Full Wave) Retardation Plate," *Olympus Life Science Solutions*. https://www.olympus-lifescience.com/en/microscope-resource/primer/techniques/polarized/firstorderplate/

[119] I. Dierking, in *Textures of Liquid Crystals*, Weinheim: WILEY-VCH Verlag GmbH & Co. KGaA, 2003, pp. 35–38. doi: 10.1002/3527602054.fmatter.

[120] L. He *et al.*, "Graphene oxide liquid crystals for reflective displays without polarizing optics," *Nanoscale*, vol. 7, no. 5, pp. 1616–1622, Jan. 2015, doi: 10.1039/C4NR06008C.

[121] A. M. Fernández-Sotillo and P. Ferreira-Aparicio, "Continuous Graphene-like Layers Formed on Copper Substrates by Graphene Oxide Self-Assembly and Reduction," *ACS Appl. Energy Mater.*, vol. 3, no. 10, pp. 10023–10036, Oct. 2020, doi: 10.1021/acsaem.0c01722.

[122] E. K. Richman and J. E. Hutchison, "The Nanomaterial Characterization Bottleneck," *ACS Nano*, vol. 3, no. 9, pp. 2441–2446, Sep. 2009, doi: 10.1021/nn901112p.

[123] D. W. Bruce, D. O'Hare, and R. I. Walton, Eds., *Structure from diffraction methods*. Chichester: Wiley-Blackwell, 2014.

[124] "What is a synchrotron?" https://www.esrf.fr/about/synchrotron-science/synchrotron

[125] T. Narayanan, H. Wacklin, O. Konovalov, and R. Lund, “Recent applications of synchrotron radiation and neutrons in the study of soft matter,” *Crystallogr. Rev.*, vol. 23, no. 3, pp. 160–226, Jul. 2017, doi: 10.1080/0889311X.2016.1277212.

[126] J. Ilavsky *et al.*, “Development of combined microstructure and structure characterization facility for in situ and operando studies at the Advanced Photon Source,” *J. Appl. Crystallogr.*, vol. 51, no. 3, Art. no. 3, Jun. 2018, doi: 10.1107/S160057671800643X.

[127] T. Narayanan and O. Konovalov, “Synchrotron Scattering Methods for Nanomaterials and Soft Matter Research,” *Materials*, vol. 13, no. 3, p. 752, Feb. 2020, doi: 10.3390/ma13030752.

[128] P. M. V. Raja and A. R. Barron, *Physical Methods in Chemistry and Nano Science*. Rice University, 2021. [Online]. Available: https://chem.libretexts.org/@go/page/55906

[129] L. J. Michot *et al.*, “Liquid–crystalline aqueous clay suspensions,” *Proc. Natl. Acad. Sci.*, vol. 103, no. 44, pp. 16101–16104, Oct. 2006, doi: 10.1073/pnas.0605201103.

[130] Z. Xu and C. Gao, “Graphene chiral liquid crystals and macroscopic assembled fibres,” *Nat. Commun.*, vol. 2, no. 1, Art. no. 1, Dec. 2011, doi: 10.1038/ncomms1583.

[131] Norbert Stribeck, *X-Ray Scattering of Soft Matter*. Berlin, Heidelberg: Springer Berlin Heidelberg, 2007. doi: 10.1007/978-3-540-69856-2.

[132] T. M. McCoy, L. de Campo, A. V. Sokolova, I. Grillo, E. I. Izgorodina, and R. F. Tabor, “Bulk properties of aqueous graphene oxide and reduced graphene oxide with surfactants and polymers: adsorption and stability,” *Phys. Chem. Chem. Phys.*, vol. 20, no. 24, pp. 16801–16816, Jun. 2018, doi: 10.1039/C8CP02738B.

[133] L. A. Feigin and D. I. Svergun, *Structure Analysis by Small-Angle X-Ray and Neutron Scattering*. Boston, MA: Springer US, 1987. doi: 10.1007/978-1-4757-6624-0.

[134] D. I. Svergun and M. H. J. Koch, “Small-angle scattering studies of biological macromolecules in solution,” *Rep. Prog. Phys.*, vol. 66, no. 10, pp. 1735–1782, Oct. 2003, doi: 10.1088/0034-4885/66/10/R05.

[135] X. Yang, C. Guo, L. Ji, Y. Li, and Y. Tu, “Liquid Crystalline and Shear-Induced Properties of an Aqueous Solution of Graphene Oxide Sheets,” *Langmuir*, vol. 29, no. 25, pp. 8103–8107, Jun. 2013, doi: 10.1021/la401038c.

[136] V. Panchal *et al.*, “Confocal laser scanning microscopy for rapid optical characterization of graphene,” *Commun. Phys.*, vol. 1, no. 1, Art. no. 1, Nov. 2018, doi: 10.1038/s42005-018-0084-6.

[137] S.-H. Hong, T.-Z. Shen, and J.-K. Song, “Shear-induced assembly of graphene oxide particles into stripes near surface,” *Liq. Cryst.*, vol. 45, no. 9, pp. 1303–1311, Jul. 2018, doi: 10.1080/02678292.2018.1435829.

[138] R. Jalili *et al.*, “Formation and processability of liquid crystalline dispersions of graphene oxide,” *Mater. Horiz.*, vol. 1, no. 1, pp. 87–91, Nov. 2013, doi: 10.1039/C3MH00050H.

[139] “Introductory Confocal Concepts,” *Nikon’s MicroscopyU, The Source for Microscopy Education*. https://www.microscopyu.com/techniques/confocal/introductory-confocal-concepts

[140] “Introduction to Confocal Microscopy,” *Olympus Life Science Solutions*. https://www.olympus-lifescience.com/en/microscope-resource/primer/techniques/confocal/confocalintro/

[141] N. S. Claxton, T. J. Fellers, and M. W. Davidson, “Microscopy, Confocal,” in *Encyclopedia of Medical Devices and Instrumentation*, American Cancer Society, 2006. doi: 10.1002/0471732877.emd291.

[142] P. Zheng and N. Wu, “Fluorescence and Sensing Applications of Graphene Oxide and Graphene Quantum Dots: A Review,” *Chem. – Asian J.*, vol. 12, no. 18, pp. 2343–2353, 2017, doi: 10.1002/asia.201700814.

[143] M. Li, S. K. Cushing, X. Zhou, S. Guo, and N. Wu, “Fingerprinting photoluminescence of functional groups in graphene oxide,” *J. Mater. Chem.*, vol. 22, no. 44, pp. 23374–23379, Oct. 2012, doi: 10.1039/C2JM35417A.

Acknowledgement

I would like to thank the jury member of my PhD defense, especially Miro for his help and support, Jan for his benevolence, Emmanuelle for her support and valuable discussion.

I would like to express my gratitude to all those who helped and supported me during my PhD journey; especially Inma, Rao, Philipp, Evandro, Eduardo, Thomas, Manos, Rijeesh, Anjali, Camila, Yong, Zory, Olga, Ralf, Alex, Suzanne, Stéphanie and Anja.

I would like to express my grateful thanks to Astrid, Monique, and Adamantia for their kindness, help and support.

I acknowledge the support of the University of Luxembourg, ALBA Synchrotron, and ESRF - The European Synchrotron.

This work was financially supported by the Luxembourg National Research Fund (FNR), CORE project Nanosoft, C16/MS/11366029. Some of the travel expenses covered during this work were funded by the Doctoral Program in Physics and Materials Science (DPPM) of the University of Luxembourg.

List of Publications and Presentations

Peer-Reviewed Publications

1. Sharif Shahini, Stephane Campidelli, Giusy Scalia, "Large graphene oxide flakes: self-assembly and electro-optical switching in liquid crystal phase". (*Ready to be submitted*)
2. Sharif Shahini, Stephane Campidelli, Giusy Scalia, "Large Graphene Oxide flakes: isotopic to nematic liquid crystal phase transition", *Physica Status Solidi B*, Vol 256, 12, 1900411, 2019, doi.org/10.1002/pssb.201900411.
3. MinJae Kim, Ji Hyun Park, Sharif Shahini, Jun Yamamoto, Stephane Campidelli, Youn Sang Kim, Giusy Scalia, "Graphene: a new liquid crystal for high performance electro-optic applications", *Proceeding of SPIE Organic Photonics + Electronics*, Volume 10735, Liquid Crystals XXII, 107350N, 2018, doi.org/10.1117/12.2501822.

Contributed Oral Presentations

1. Sharif Shahini, Giusy Scalia, "Assembly of liquid crystal graphene oxide flakes", Presented at MASSENA Young Scientist Conference 2021, Sport Hotel Leweck, June 2021, Lipperscheid, Grand Duchy of Luxembourg.
2. Sharif Shahini, Stephane Campidelli, Giusy Scalia, "Orientation and reorientation of graphene oxide liquid crystal flakes", Presented at Optics of Liquid Crystals 2019 (OLC2019), Hotel Château Laurier, September 2019, Québec city, Canada.

Poster Presentations

1. Sharif Shahini, Stephane Campidelli, Giusy Scalia, "Graphene oxide flake behavior under electric field in liquid crystal phase", Presented at International Winterschool on

Electronic Properties of Novel Materials 2019 (IWEPNM2019), Hotel Sonnalp, March 2019, Kirchberg in Tirol, Austria.

2. Sharif Shahini, Stephane Campidelli, Giusy Scalia, "Electro-optic switching of graphene oxide liquid crystal", Presented at Graphene Study 2019, Obergurgl University Center, February 2019, Obergurgl, Austria.
3. Sharif Shahini, Stephane Campidelli, Giusy Scalia, "Low electric field switching in the liquid crystal phase of graphene oxide LC", Presented at the 27th International Liquid Crystal Conference (ILCC2018), Kyoto International Conference Center, July 2018, Kyoto, Japan.
4. Sharif Shahini, Stephane Campidelli, Giusy Scalia, "Graphene oxide switching in liquid crystal phase", Presented at the German Liquid Crystal Conference 2018, University of Luxembourg, March 2018, Luxembourg, Grand Duchy of Luxembourg.